This electronic thesis or dissertation has been downloaded from the King's Research Portal at https://kclpure.kcl.ac.uk/portal/



Molecular Dynamics Simulation Study of Non-Ionic Surfactant-Based Nanoparticles

Ishkhanyan, Hrach

Awarding institution:
King's College London

The copyright of this thesis rests with the author and no quotation from it or information derived from it may be published without proper acknowledgement.

END USER LICENCE AGREEMENT



Unless another licence is stated on the immediately following page this work is licensed

under a Creative Commons Attribution-NonCommercial-NoDerivatives 4.0 International

licence. https://creativecommons.org/licenses/by-nc-nd/4.0/

You are free to copy, distribute and transmit the work

Under the following conditions:

- Attribution: You must attribute the work in the manner specified by the author (but not in any way that suggests that they endorse you or your use of the work).
- Non Commercial: You may not use this work for commercial purposes.
- No Derivative Works - You may not alter, transform, or build upon this work.

Any of these conditions can be waived if you receive permission from the author. Your fair dealings and other rights are in no way affected by the above.

Take down policy

If you believe that this document breaches copyright please contact librarypure@kcl.ac.uk providing details, and we will remove access to the work immediately and investigate your claim.

Download date: 08. Oct. 2023

Molecular Dynamics Simulation Study of Non-Ionic Surfactant-Based Nanoparticles

Hrachya Ishkhanyan

A thesis submitted in partial fulfillment
of the requirements for the degree of
Doctor of Philosophy in Physics
of
King's College London.

Department of Physics
King's College London

September 1, 2023

Abstract

In this thesis, surfactant-based self-assembled nanoparticles were investigated using molecular dynamics simulations. First, the structural properties and the encapsulation of two non-steroidal anti-inflammatory drugs (NSAIDs) - ibuprofen and indomethacin - within Triton X-100 (TX-100) micelles were investigated. The pure TX-100 micelle was found to be semi-spherical in shape, whereas the micelles in the presence of the drugs become aspherical. This effect was more significant with indomethacin, where continuous elongation of the micelle resulted in splitting it into two, which was caused by the destabilization of the micelle due to clustering of indomethacin inside of it. The results have shown that more indomethacin than ibuprofen has been solubilized. Another surfactant from the Triton X family, Triton X-114 (TX-114), which has a shorter hydrophilic PEG headgroup than TX-100, was used as a building block for the nanoparticle. The TX-114 micelle have solubilized more ibuprofen than TX-100 micelle. Furthermore, similar to the TX-100 micelle, indomethacin clusterization inside of TX-114 micelle caused a splitting of the initial micelle into two. Lastly, we investigate the effect of cross-linking between surfactants on the structural properties of micelles. In doing so, micelles containing different amounts of TX-100 and the polymer version of TX-100, Tyloxapol, consisting of 3 (trimer) and 7 (heptamer) monomers, were investigated. Structural differences and properties were investigated using various tools and in-house written Python scripts. Pure trimer and heptamer micelles stabilized quickly and have been found to be oblate in shape. Furthermore, it was found that all micelles formed by the heptamer, were stable with very small

fluctuations in their RMSD. The systems containing 75% and 25% Tyloxapol trimer, were the least stable with a significant amount of water inside of the hydrophobic core. During this project, I created a Python code (still in development), that allows one to determine the location interface of nanoparticles whose shape is not spherical in nature. This code then allows one to accurately describe the structural properties of the micelle and its surroundings.

Acknowledgements

Firstly, I would like to thank my supervisor, Chris Lorenz, for all the support and encouragement he has provided throughout these years. With his invaluable guidance I have been able to repel every doubt I have had and overcome the challenges before me. Four years ago, not only have I found a supervisor everyone would love to have, but I have also found a dear friend.

I would also like to thank my second supervisor, Natasha Rhys, whose support was irreplaceable. I want to thank Mat Bieniek and Paul Smith for having me during their coding sessions, and for the intense pool matches we have had. Furthermore, I would like to thank Rob Ziolek, who has always found time to help me, and Jirawat Assawakhajornsak who has been a good friend and a worthy opponent at table tennis. Huge thanks to Alejandro Santana-Bonilla whose help and insight have played a huge role in my recent work. And of course, thanks to the rest of past and present members of Lorenz Lab, namely to Demi Pink, Mohamed Ali Al-Badri, Sze May Yee, Adam Suhaj, Raquel Lopez-Rios De Castro, Miruna Serian, Joanna Xie, Javier Garcia-Ruiz, Alice Pettitt, Zhiwen Zhong, Melissa Jade Mitchell, a fun, smart and supportive group of people.

A huge thank you to Mr Vartan Ouzounian, the Honourary Secretary of Tekeyan Trust London, who kindly agreed to fund my research. I could not have reached this far without his support.

Thanks to my dear friends, Shushan, Alik, Petros, Erik, Karen and Lusine for always being there for me. Although being physically separated, you have

never abandoned me and I have never felt this close to you all. To dear Arus, whom I can always turn to to complain about life. To my dear Alla, who gave me hope in hopeless times and has made perhaps the most difficult stage of my PhD less stressful.

Lastly, I thank my dearest family, my father, Avetik, my mother, Nune, my brother, Rafael and my harsik, Ani, who encouraged me, unreservedly supported me and believed in me when I did not. And a special thank you to my late grandmother, Frina, the kindest and the most loving and caring woman I have ever known, who could always make us smile in the most difficult times, even after her passing. Rest in peace, tatik.

The last card in the hands of people whose future is at stake is education.

Garegin Nzhdeh

Love and joy pass through
As do beauty, treasure and throne,
Death is for us, and we are for death,
It's deed alone that lives on.

Man's deeds are immortal, know it well,
Through centuries they will transcend;
Blessed is he, who by his deeds
Lives on forever till the end.

The Capture of Tmkaberd
Hovhannes Tumanyan

When people will stop being evil, when peace and brotherly love will reign over the world, I will be ready to be the kindest and kiss my enemies.

Madman
Raffi

Contents

1 Introduction **14**

1.1 Motivation 14

1.2 Surfactants 15

1.2.1 Overview 15

1.2.2 Surfactants in solution 16

1.2.3 Surfactant applications 17

1.2.4 Toxicity of surfactants 21

1.2.5 Non-ionic surfactants 21

1.2.6 Oligomeric surfactants 22

1.3 NSAIDs 23

1.4 Self-assembly 25

1.5 Computer Simulations 26

1.5.1 Simulations of multiparticle systems 26

1.5.2 Computer simulations of self-assembly 27

1.5.3 Computer simulations as complementary to experiments 28

1.5.4 Simulations of surfactant systems 29

2 Methods **32**

2.1 Molecular Dynamics 32

2.1.1 Equations of motion 32

2.1.2 Force field 33

2.1.3 Verlet integration 36

2.1.4 Periodic boundary condition 38

2.1.5 Calculation of forces . . . 39
2.1.6 Thermodynamic ensembles . . . 41
2.1.7 Setting up a simulation . . . 44
2.1.8 Analysis of trajectories . . . 46
2.1.9 Visuals . . . 51

3 Impact of drug aggregation on the structural and dynamic properties of Triton X-100 micelles 52

4 NSAID solubilisation promotes morphological transitions in Triton X-114 surfactant micelles 66

5 AICON: A Python package to analyze aspherical nanoparticles 77

5.1 Introduction . . . 77
5.2 Methods . . . 79
5.2.1 Defining the interface . . . 79
5.2.2 Enhancing code performance . . . 81
5.3 Results . . . 83
5.3.1 Volume . . . 83
5.3.2 Densities . . . 85
5.3.3 Code performance analysis . . . 87
5.4 Conclusion . . . 89
5.5 Future work . . . 90

6 Structural properties of Triton X-100- and Tyloxapol-based mixed micelles 92

6.1 Introduction . . . 93
6.2 Methods . . . 95
6.2.1 Molecular dynamics simulations . . . 95
6.2.2 Analysis of trajectories . . . 97
6.2.3 Basic analysis . . . 97

6.2.4 Interface definition and density calculation 98
6.2.5 Volume calculation 99
6.2.6 Neighbour analysis 99
6.3 Results 100
6.3.1 Structural properties of micelles 100
6.3.2 Density calculations 102
6.3.3 Neighbour analysis 104
6.3.4 Conclusions 106
6.3.5 Future work 107

7 Conclusions **108**

8 Future work **111**
8.1 Wrapping up and future prospects 111
8.2 G-quadruplex DNA selective drugs 112

Appendices **114**

A Supporting information for "Impact of drug aggregation on the structural and dynamic properties of Triton X-100 micelles" **114**

B Supporting information for "NSAID Solubilisation Promotes Morphological Transitions in Triton X-114 Surfactant Micelles" **123**

C Analysing code performance in "AICON: A Python package to analyze aspherical nanoparticles" **139**

D Additional analysis for Triton X-100- and Tyloxapol-based mixed micelles **146**

List of Figures

1.1 Simplified structures of four classes of surfactants 15

1.2 Examples of self-assembled structures. 17

1.3 Biopharmaceutics Classification System (BCS) drug classes . . . 20

1.4 Schematic diagram of surfactant oligomers. m monomers are linked by a spacer (in red). 23

1.5 6 classes of NSAIDs. All except from coxibs are non-selective towards COX enzyme. Coxibs on the other hand selectively bind to COX-2. Depicted structures correspond to the first entry of each NSAID subclass. 24

1.6 Snapshot of Tyloxapol-based nanoparticle. Cyan coloring corresponds to the hydrophobic core of the micelle. 28

2.1 Potential terms used in classical MD force field 35

2.2 Martini force-field mapping schematics. Red, blue, grey and green are respectively charged, polar, non-polar and apolar type beads. 36

2.3 Periodic boundary conditions visualized in 2D 39

2.4 Lennard-Jones potential 40

2.5 Convex and non-convex sets. 48

2.6 Convex hull of set of points (red). Purple, green and blue are all convex sets containing the points. Region in red is the minimal convex set, or the intersection of all convex sets enclosing the points. 49

2.7 2D gift wrapping algorithm. For every point on the hull, N points are checked to find the next point. s is the number of vertices on the hull. 50

2.8 A graph and its associated adjacency matrix. 51

5.1 Schematic representation of Riemann sum method. A cross-section of a 3D spherical particle is shown on the left and an isolated slice is shown on the right. 80

5.2 The grid representation of the simulation box in 2D. The initial grid is in black, where $d = 1$Å. The densities are calculated in a larger grid (in red). 81

5.3 Schematic diagram providing a successful Cython workflow. . . 83

5.4 Test structures for the volume calculations: cylinder (left) and sphere (right) 84

5.5 Density of particles in the test structures estimated by a standard approach (left) and the AICON algorithm (right). 84

5.6 Density profiles of water, Triton X-100 hydrophobic tail and hydrophilic head. Comparison of results from two algorithms (left - algorithm of this thesis, right - nanoCISC). 86

5.7 Snapshots of (left) the semi-spherical TX100 micelle and (right) the elongated TX100 micelle. 87

5.8 Density profiles of water, Triton X-100 hydrophobic tail and hydrophilic head. Comparison of results from two algorithms (left - AICON, right - nanoCISC). 87

5.9 Performance time for different techniques to compute densities in AICON algorithm as a function of the number of frames employed. 88

5.10 Linear dependence of the execution time on the number of particles. 89

5.11 A 2D convex hull (red) for a set of particles (blue) for which the interface needs to be defined. Solvent particles (marked with ×) inside of the hull are in green. A concave representation of an interface is in light green. 91

6.1 Snapshots of Tyloxapol ($m = 3$, left) and Triton X-100, and Tyloxapol ($m = 7$, right) and Triton X-100 mixed micelles. Both snapshots are taken from the 50/50 Tyloxapol-Triton X-100 systems 95

6.2 Surfactants from Triton X family. For TX100, $n \approx 9.5$, as for TX114, $n \approx 7.5$. $m \approx 7$ for Tyloxapol. 96

6.3 RMSD of Tyloxapol trimer (left) and heptamer (right) based micelles as a function of time. 101

6.4 Radius of gyration of Tyloxapol trimer (left) and heptamer (right) based micelles as a function of time. 101

6.5 Solvent accessible surface area (SASA) of Tyloxapol trimer (left) and heptamer (right) based micelles as a function of time. . . . 102

6.6 Volumes of TYL3 (left) and TYL7 (right) micelles as a function of time. 103

6.7 Ellipticity of Tyloxapol trimer (left) and heptamer (right) based micelles as a function of time. 104

6.8 Densities of water and carbon atoms in hydrophibic tail and hydrophilic head in pure TYL3 system (left) and pure TYL7 system (right). 104

6.9 Density profiles for Tyloxapol-Triton X-100 mixed micelles. . . . 105

6.10 Percentage of Tyloxapol trimers around TX100 surfactants. . . . 106

6.11 Percentage of Tyloxapol heptamers around TX100 surfactants. . 106

C.1 Output of the profiler 141

C.2 Output of the profiler for the compiled version of the code . . . 142

C.3 Visualized statistics provided by the profiler 143

C.4 The visualization of the results from profiling the AICON code. 145

D.1 Radius of gyration for Tyloxapol and Triton X-100 mixed micelles 147

Chapter 1

Introduction

1.1 Motivation

Development of novel drug delivery nanoparticles is crucial for the pharmaceutical industries to manufacture cheaper and safer drugs. The principal aim of this thesis is to elucidate the mechanisms of the self-assembly of surfactant-based structures. Additionally, the molecular-scale interactions which play a key role in the solubilisation of drugs within these micelles are investigated. This study sheds light on the interactions between surfactant micelles and poorly soluble drugs, the effect of solubilisation on the shape and structure of the micelles, and provides crucial insights for future development of non-ionic surfactant based drug formulations.

Knowledge of the three-dimensional structure of a system, exact coordinates and velocities of each of the atoms, allows one to compute huge variety of properties of this particular system. In this study, Molecular Dynamics (MD) was used, which provides just this throughout the whole evolution of the system in time. Second part of this thesis is partially dedicated to the analysis of such systems. A novel method to calculate the intrinsic density profiles of different species around a nanoparticle is reported. Also, a protocol is described on making Python codes, designed for scientific use, faster, by usage of code compilation and optimised multiprocessing.

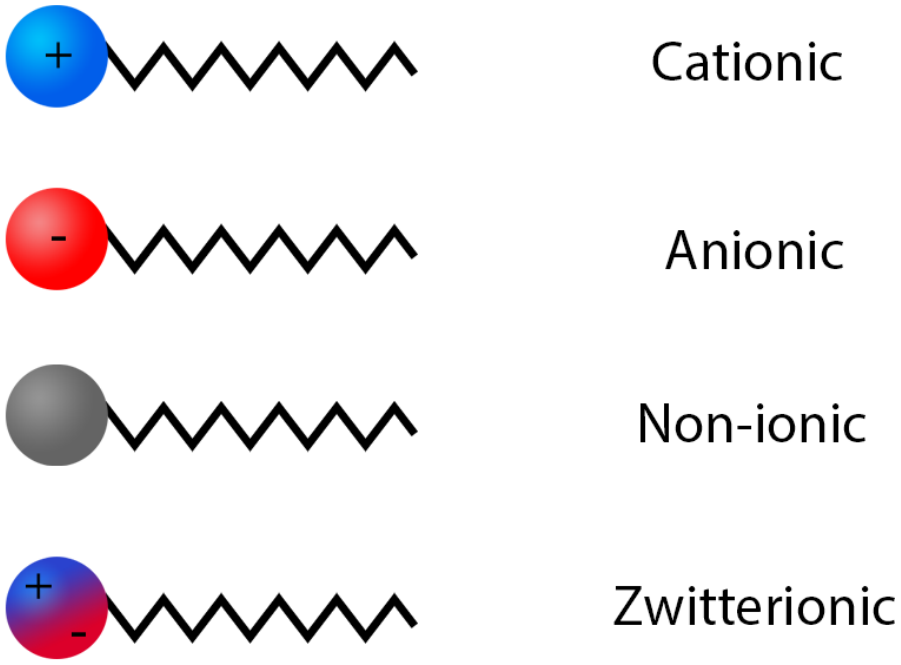


Figure 1.1: Simplified structures of four classes of surfactants

1.2 Surfactants

1.2.1 Overview

Surface active agents or surfactants[1] are molecules that decrease surface tension at the interface of two separate phases. Surfactants are amphiphiles, meaning they are comprised of two parts - a hydrophilic headgroup and hydrophobic tail. These molecules are widely used in detergent products, as emulsifiers, cell lysis agents etc.[2–4] Due to their low production cost and self-assembly into various vesicular structures, over the years surfactants became a popular building block for drug-delivery vehicles (DDV) in pharmacological research.[5–8]

Surfactants can be classified according to the net charge of their polar headgroup. Surfactants are ionic if their headgroup is charged (anionic and cationic for positive and negative charges respectively) and non-ionic otherwise. Ionic surfactants that contain both positive and negative charge on their headgroup, are another class of surfactants, such as betaines, are called amphoteric (or zwitterionic), meaning they behave as bases or acids depending

on the pH of the environment. Schematic representation of different surfactant classes in shown on Figure 1.1.

1.2.2 Surfactants in solution

The usage of surfactants particularly in cleaning products is due to their ability to gather at the interfaces of different phases, e.g. liquid-liquid, liquid-gas, liquid-solid etc. A small concentration of surfactants in water are not fully solvated, instead hydrophilic part remains in water, while the hydrophobic part will try to have as little water around it as possible, eventually finding itself in the air, outside of the liquid phase. As a result, we get a monolayer of surfactants at the water-air interface, with the polar headgroups in water, and non-polar tails outside in the air. With the increase of surfactant concentration, above a certain concentration, namely critical micelle concentration (CMC), surfactants tend to cluster up, forming various structures depending on factors such as their concentration, temperature, presence of other types of molecules.[9] A few examples of such structures are micellar or lamellar structures, cylinders, liposomes etc. (Figure 1.2). In water-in-oil environments a special type of micellar structures, so-called reversed micelles, can be distinguished. However, it is worth noting that the CMC of a micelle formation in a polar solution and the CMC of reverse micelle formation in an apolar solution can differ, as unlike in aqueous solution, where the core of the micelle is comprised of the hydrophobic parts, in case of the reverse micelles, the polar headgroup has less-favorable interaction with the solution, hence forming the core.[10,11]

It was revealed that depending on the concentration of the surfactant in the solution, a number of properties of the solution itself suffer abrupt changes. Changing behaviour of properties such as conductivity, surface tension, turbidity differs below and above the CMC of the surfactant.[9]

Another important parameter when dealing with surfactants (particularly nonionic) is its cloud point (CP). CP of a surfactant is the temperature above which a phase separation between the surfactant and solute is seen, making the

solution turbid. Although it is not to say that a complete phase separation happens, but rather two phases appear, one containing significantly larger concentrations of surfactant than the other. At the cloud point, much larger aggregates of surfactant molecules appear in one of the phases. Surfactants might lose the capabilities necessary, if for the specific application a micellar solution is required. Thus, it is crucial to take this property into consideration for the application in question, and in context of this work, in pharmaceutical development, as too low of a cloud point may reduce the bioavailability and increase the toxicity of the drug.[12,13] The CP can also be affected by the drugs and other substances present inside of the solution.[14,15]

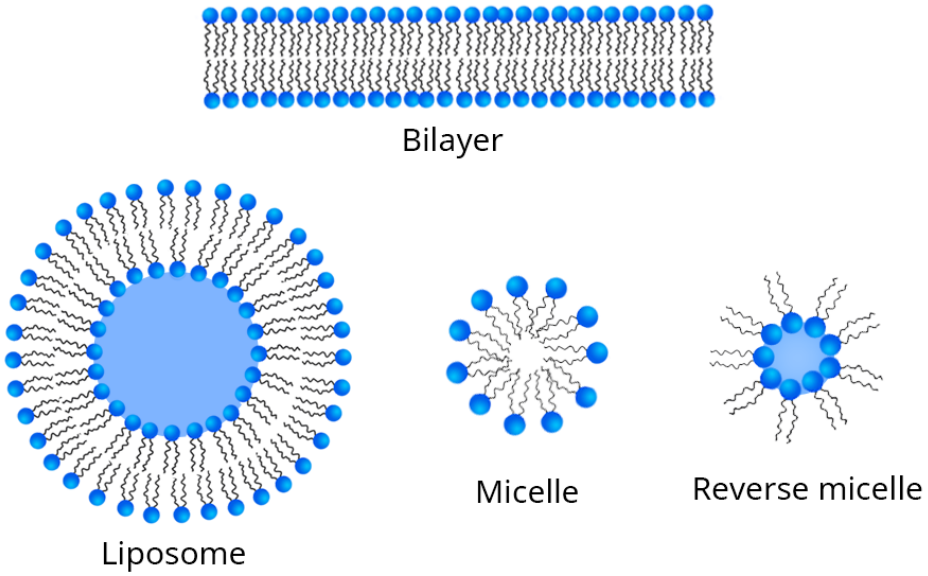


Figure 1.2: Examples of self-assembled structures.

1.2.3 Surfactant applications

With their ability to reduce surface tension, increase bioavailability of hydrophobes and the ease of their production, surfactants are widely used in industry, from food and cosmetics to anti-pollutants and drug delivery agents.[5,16–18] Biodegrading capabilities, as well as protein denaturation abilities of surfactants has made them popular antimicrobial and antiviral agents.[19] Some surfactants have also shown antifungal activity.[20] This subsection will

briefly review some of the applications of surfactants.

Agriculture: With the increase of global population, a substantial need arises to provide all humans with an adequate amount of food.[21] Development of new solutions to expand food production is crucial. This includes development of modified crops with higher yield, more effective pesticides, better fertilizers, etc. Pesticides and other agrochemical formulations often contain substances that are highly hydrophobic, which, of course, represents a serious issue when dealing with foliar uptake by the plants.[22] Surfactants provide a solution to this problem by improving the adhesion of the water insoluble substance on the plant's surface. They can also be used to inhibit various microorganisms ability to degrade the control formulations, such as pesticides or insecticides.[16,23,24] Surfactants are added in so called adjuvants, or additive formulations, that are designed to enhance the effect of the active ingredient.[25,26]

Cosmetics and hygiene: Perhaps the most common use of surfactants is in soaps and detergents. By enhancing the solubility of hydrophobic compounds, which form stains on skin, fabric or other surfaces, they are an important part of our hygiene and of our everyday lives in general.[27,28] They are extensively used in skin and hair care products, such as gels and shampoos. In cosmetics, surfactants are often used in nail and lip products, particularly in water-in-oil emulsion lipsticks, as well as for uniform dispersion of colorants in lip products.[17]

Environmental applications: The presence and accumulation of hydrophobic organic compounds in soil can cause irreversible damage to human and animal health. Soil remediation is commonly done in a process called pump-and-treat, which is achieved by pumping the contaminated groundwater and running it through a process of purification.[29] Initially, it did not prove to be very effective due to the presence of strongly hydrophobic compounds in polluted water.[30] To overcome this issue, an increase of solubilization of these compounds is needed, and can be achieved by application of surfactants.[30,31] Above their critical micelle concentration (CMC), surfactants form micellar

structures, which encapsulate the contaminants, enhancing their solubility, enabling their extraction with water.[32]

Oil and gas industry: Generally, oil-producing wells suffer from poor oil recovery that may be related to the high viscosity of oil, resulting in decrease of mobility, or low permeability of reservoirs.[16] Enhanced oil recovery (EOR) is a technique to address the issues mentioned above. One technique, suggested in the early 20th century and first initiated in the 1980s, was enhanced oil recovery using microbial species (MEOR),[33–35] the essence of which is the injection of microbe-produced substances, particularly biosurfactants, into the reservoir, resulting in a decrease of oil viscosity. Another approach, namely chemical enhanced oil recovery (cEOR), uses the injection of surfactants, polymers and other chemicals into the oil reservoir in order to increase recovery.[36–38]

Another application of surfactants in the field is their utilization as corrosion inhibitors in gas pipelines. Gemini surfactants, that consist of two monomer surfactants cross-linked between their hydrophobic or hydrophilic sites, are of a great research interest as anti-corrosion agents.[39,40] Furthermore, in gas pipelines, ice-like substances called gas hydrates, can form, causing a blockage of the pipe, thus preventing the free-flow of natural gas.[41] Surfactants, when injected in small amounts into the gas, can prevent or reduce their formation by reducing adsorption of gas on hydrate surfaces.[42–44]

Pharmaceutical industry: Although pharmaceutical applications of surfactants are numerous and would require a whole chapter, to cover some of them, a brief summary will be presented here. Firstly, surfactants are used for solubilization of hydrophobic drugs. An estimated amount of $40 - 60\%$ of all drug formulations and drug candidates have hydrophobic active ingredients. This is mostly due to the fact, that apart from high solubility, many drugs need to be highly permeable through the membranes of cells. Figure 1.3 shows four classes of drugs according to the Biopharmaceutics Classification System (BCS)[45] as a functions of their permeability and solubility. A number of potential drug candidates are class II, which have adequate perme-

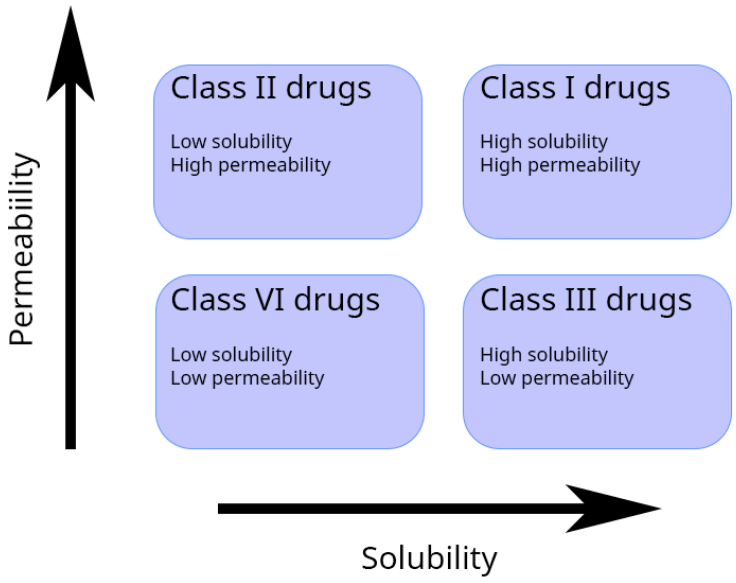


Figure 1.3: Biopharmaceutics Classification System (BCS) drug classes

ability but poor solubility.[46] In order to enhance the solubility of such drugs, one strategy is their encapsulation inside drug delivery formulations.[47–50] Surfactant nanoparticles, particularly ones based on non-ionic surfactants, are often used in development of such formulations. A few examples of surfactant nanoparticle-based drugs available in the market are anti-cancer Abraxane,[51] Doxil,[52] anti-fungal Amphotec,[53] painkiller Flarin,[54] etc. Secondly, surfactants are used as emulsifiers for oil-based drugs, to stabilize them and make the administration easier.[55–57] Furthermore, surfactants are used as tablet lubricants and wetting agents during the tablet manufacturing process. One of the steps in tablet manufacturing is the pressing of drug powder inside of a die with punches. In order to reduce the friction in the die, and avoid powder sticking on the punch or inside of die walls, a proper lubricant must be used. Sodium dodecyl sulfate (SDS), magnesium stearate and other surfactants are often used as lubricating agent in this application.[58–62] Finally, controlled release

can be achieved by incorporation of surfactants in drug formulations. They are used as structure directing agents (SDA),[63] which are modifiers for existing nanoparticles.[64] Carvalho et al.[65] investigated surfactant systems to increase bioavailability and improve release of AZT, an acquired immune deficiency syndrome (AIDS) treatment drug.

It is worth noting, that alongside with the advantages and benefits of surfactants there is also a certain degree of toxicity associated with them and their usage in the applications mentioned above. The next subsection will briefly review some of the issues related to the harm caused by surface active molecules.

1.2.4 Toxicity of surfactants

Despite their wide use in a number of fields, surfactants have some degree of toxicity one must consider. Some surfactants have low biodegradability, making them hard to remove from the environment and toxic for land and aquatic life. Several studies have investigated amounts of different ionic (linear alkylbenzene sulfonates, sodium dodecylbenzenesulfonate) and non-ionic (nonylphenol ethoxylates) surfactants in wastewater treatment plants from where they could be discharged into environment.[66–68] In humans, some surfactants may cause skin and eye irritation. Marrakchi and Maibach[69] studied and showed face skin irritation caused by SDS. Effendy and Maibach in their review[70] talk about the evidence of different surfactants, e.g. SDS, benzalkonium chloride (BAC), cocamidopropyl betaine (CAPB), that cause irritation as well as skin conditions, such as dermatitis.

1.2.5 Non-ionic surfactants

As previously discussed, non-ionic surfactants carry zero net charge on the polar headgroup, thus making them less susceptible to pH and electrolytes in the solution. The lack of net charge can be advantageous especially in drug design, as non-ionic surfactants generally have lower CMCs. This renders them less toxic compared to their ionic counterparts.[71] The reason is, that if

the surfactants are diluted too much (below the CMC), a leakage of drugs may occur, and using surfactants with a lower CMC addresses this issue.[6] Furthermore, it has been shown that non-ionic surfactants cause less irritation than the other three classes of surfactants.[70,72,73]

The surfactants used in this study are Triton X-100 (TX100), Triton X-114 (TX114) and their polymeric variant, called Tyloxapol. Triton X surfactants are non-ionic, that are comprised of hydrophilic polyethylene oxide (PEO) headgroup and a hydrophobic aromatic hydrocarbon tail. Due to their hydrophilic headgroups being longer than their hydrophobic tails, these surfactants form structures resembling those of reversed micelles above their CMC. The difference between TX100 and TX114 is the number of monomers in the PEO chain. Tyloxapol is made of an average of 7 Triton X monomers whose hydrophobic groups are crosslinked.

1.2.6 Oligomeric surfactants

Oligomeric surfactants are formed by covalent cross-linking between the monomers (Figure 1.4). Cross-linked surfactants are known to show properties very different from their precursor molecules. In a study by Espert et al.[74] a dimerized DTAB showed much smaller CMC than the monomeric version, and Kern et al.[75] show higher viscosity of the solution with dimerized form of DTAB than its monomeric counterpart. In more recent studies, an increased anti-microbial activity was demonstrated by the application of oligomerized surfactants.[76–78]

In this thesis, Tyloxapol (or Triton WR-1339), the oligomeric variant of Triton X-100, is studied. In a study conducted by Schott,[79] the difference between these two surfactants and their micellization properties were investigated. The study showed that tyloxapol has a reduced CMC compared to TX100, a trait seen for other surfactants when in monomer or in dimeric/oligomeric form. It also shows an increase in the cloud point by 28°, which is a useful property when dealing with pharmaceutical research. Furthermore, tyloxapol micelles show higher viscosity than TX100 micelles.[80] Studies on

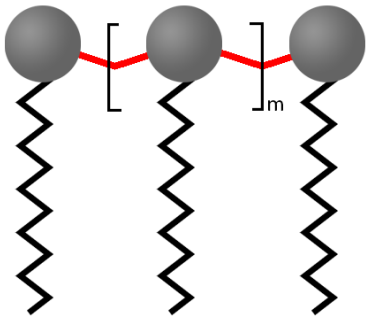


Figure 1.4: Schematic diagram of surfactant oligomers. m monomers are linked by a spacer (in red).

drug solubilization in tyloxapol micelles and niosomes (non-ionic surfactant-based vesicles) were reported by Mehta and Jindal,[18,81] where the carriers show excellent solubilization potential for anti-tuberculosis drugs. A recent study by Dharaiya et al.[82] reported a superior solubility of bisphenol A in tyloxapol micelles, than in TX100 micelles.

1.3 NSAIDs

Non-steroidal anti inflammatory drugs (NSAID) are medicines used for pain relief, fever and inflammation treatments. The first anti-inflammatory drug discovered was salicylic acid, which served as the precursor for the first synthesized NSAID to be produced in 1897 - aspirin.[83] Other notable members of this class of drugs include ibuprofen,[84] naproxen,[85] diclofenac,[86] indomethacin.[87]

Although in a neutral pH NSAIDs are deprotonated, they are still somewhat poorly-soluble. There are several classes of NSAIDS (Figure 1.5), but all of them share the same mechanism of action, that is inhibiting the cyclooxygenase (COX) enzyme that converts arachidonic acid into molecules such as prostaglandins and thromboxanes,[88,89] which are responsible for pain and inflammation. There are two COX enzymes, namely COX-1 and COX-2. As with every drug, there are a number of side-effects associated with

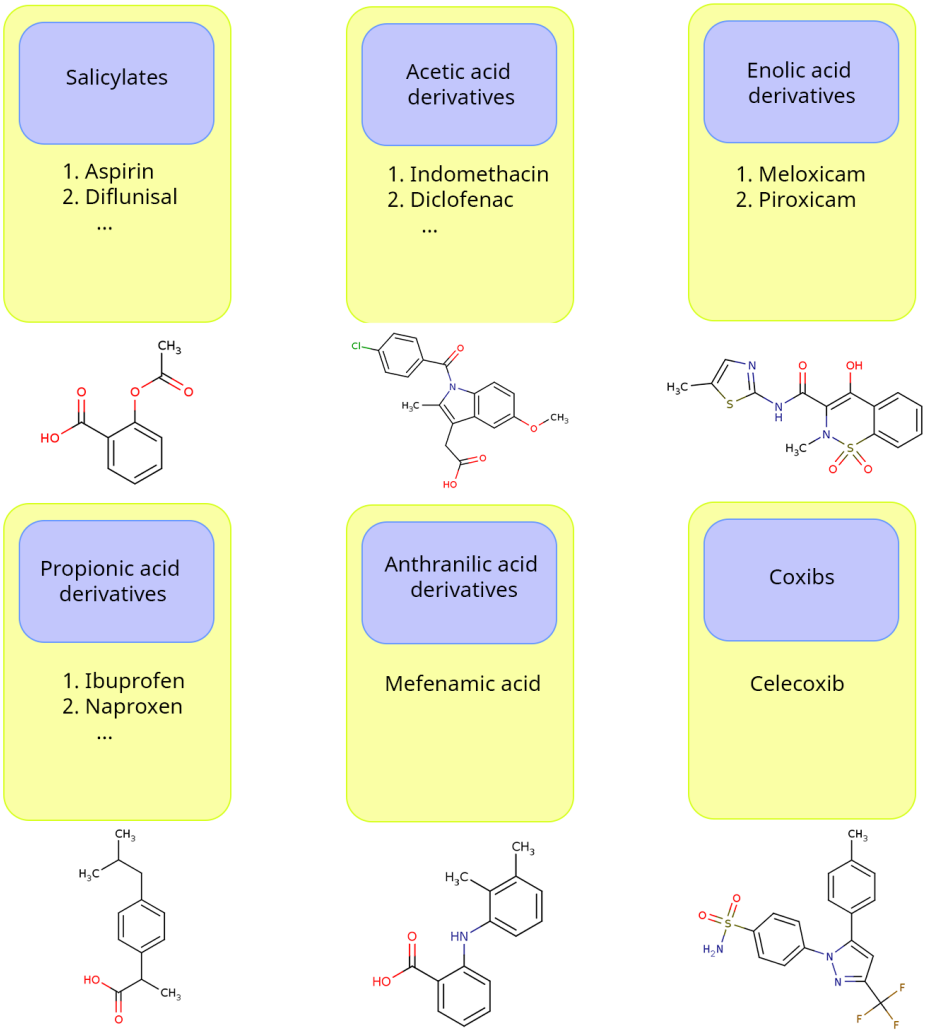


Figure 1.5: 6 classes of NSAIDs. All except from coxibs are non-selective towards COX enzyme. Coxibs on the other hand selectively bind to COX-2. Depicted structures correspond to the first entry of each NSAID subclass.

NSAIDs,[90–92] some of which are directly related to non-selectivity to COX enzymes in majority of NSAIDs. The COX-1 enzyme is also responsible for regulatory processes in cells, such as providing protection for stomach mucosa, blood platelets, kidneys, pancrea, etc,[93] whereas its inhibition causes number of undesired conditions.[94] One way this issue was addressed was by the introduction of coxibs, COX-2 selective inhibitors. An alternative way to make the drugs safer is loading them in drug delivery vehicles (DDV).

In this thesis, two NSAIDs were solubilized within the surfactant DDVs

- ibuprofen and indomethacin. Perhaps the most well-known and wide-spread of all NSAIDs, ibuprofen arrived in markets more than 50 years ago as a prescription drug for treatment of rheumatoid arthritis, and becoming an over-the-counter drug a decade later thanks to its relative safety at normal doses. However, as is commonly true with other NSAIDs, ibuprofen is associated with various adverse effects, such as gastrointestinal, renal, hepatic.[95–99] Indomethacin, synthesized around the same time as ibuprofen, is an acetic acid derivative, that has very potent analgesic and anti-inflammatory capabilities.[100,101] Due to its higher potency and toxicity, indomethacin is prescribed only. Structures of both drugs are presented in Figure 1.5.

1.4 Self-assembly

In broader terms, self-assembly is the emergence of various functional structures from individual building blocks, that are held together due to internal interactions or forces. Self-assembly occurs in nature and is in the basis of many vital compounds existing in all organisms. Proteins, which are chains of amino-acids, are forming their three dimensional structure, which is responsible for their functionality,[102] the complementary DNA strands coming together to form the molecule of life, are two of many examples of self-assembly in nature. A number of different substances can serve as building blocks for self-assembled structures, e.g. nucleic acids, polymers, peptides, lipids, surfactants, etc.[103–106]

In the context of this thesis, self-assembly relates to organization of amphiphiles into micellar structures in an aqueous environment. There are no covalent bonds between self-assembled structures, and their stability is provided by many weaker interactions, such as Van der Waals, hydrophobic and electrostatic interactions and hydrogen bonds, which result in structures that are in thermodynamic minima.[107] The process of self-assembly is spontaneous and requires no external factors. It is worth to note, that different factors, e.g. temperature, concentration, etc. affect the shape and structure of a given self-assembled nanoparticles.

As discussed earlier, surfactants are amphiphiles, and given the right concentration (above the CMC), they spontaneously form such nanoparticles. This work focuses on nanoparticles formed by non-ionic Triton X micelles. Triton X-based structures and their rheological properties for different phases have been extensively studied in experiment[108,109] and, not in the same extent, in computational simulations.[110,111] However little research has been carried out to investigate drug solubilization capabilities of the Triton X-based micelles.[112] This study emphasizes on the drug carrying capabilities of TX micelles as well as the effect of crosslinking between the surfactants on their structural properties.

1.5 Computer Simulations

1.5.1 Simulations of multiparticle systems

Computer simulations date all the way back to the mid of 20th century when the first simulation of a few hundred particles using the Monte Carlo (MC) method in two-dimensional space was carried out.[113] The molecular dynamics (MD) technique, which allows one to obtain the dynamics of a system, were first carried out by Alder and Wainwright in 1957, with a system containing a few hundred particles, modelled as hard spheres in a square-well potential.[114,115] A more realistic model using the Lennard-Jones potential to simulate 900 argon atoms was conducted in 1964 by Rahman.[116] The above mentioned studies prepared the foundation for the rapid development of MD, after which more complex systems, such as diatomic molecular liquids[117,118] and water[119] were simulated. In 1977, the first protein simulation was conducted[120] and was followed by simulations of other complicated systems, such as polymers, nucleic acids,[121] lipids, etc. With the rapid advancements in computational technology, development of high performance CPUs and GPU acceleration, we can now model millions of particles and simulate them in timescales on the order of microseconds in a matter of days.

The value of computer simulations is that it describes the system quan-

titively, providing exact results, that can be compared either with theory or with experiment. In that sense, computational simulations are intermediary between these two. Modelling a theory allows one to test it, and comparing the results with the experiment allows testing the model itself. A good model can be of great use to experimental scientists, acting as a microscope[122] with an atomic level of resolution, unraveling mechanisms of various physical, chemical and biological processes.

1.5.2 Computer simulations of self-assembly

The process of self-assembly in reality could be a process, that exceeds microseconds, which, for certain systems, would be unfeasible to simulate. With the advancement of high performance computing, and refinement of techniques such as coarse-grained (CG) simulations, the investigation of self-assembly with MD simulations started to gain popularity. In some early attempts, united-atom (UA) and all-atom (AA) MD simulations were used to model the self-assembly of amphiphilic systems. Hautman and Klein[123] investigated amphiphile monolayer formation on gold with UA MD simulations. This project was then extended by modelling the same system using an AA approach, which held overall better results. Karaborni et al.[124] simulated aggregates formed by model gemini surfactants, while Griffiths and Hayes[125] successfully simulated self-assembly of surfactant reverse micelles. All of the simulations above were run in scale of 10s - 100s of nanoseconds. In more recent work by Kraft et al., the CG approach enabled simulations of the self-assembly of more sophisticated DHPC lipids to be run for a few μs. Furthermore, the nucleation process of urea using metadynamics has been studied by Salvalaglio et al.[126–128]

There are cases, when one, knowing about the existence of a certain self-assembled structure, is not interested in the exact mechanism of self-assembly, and aims to understand the structural properties of the system, or solubilization of various compounds in it. In this scenario, pre-assembled structure can be used as an initial starting point for the simulation. It was shown in MD

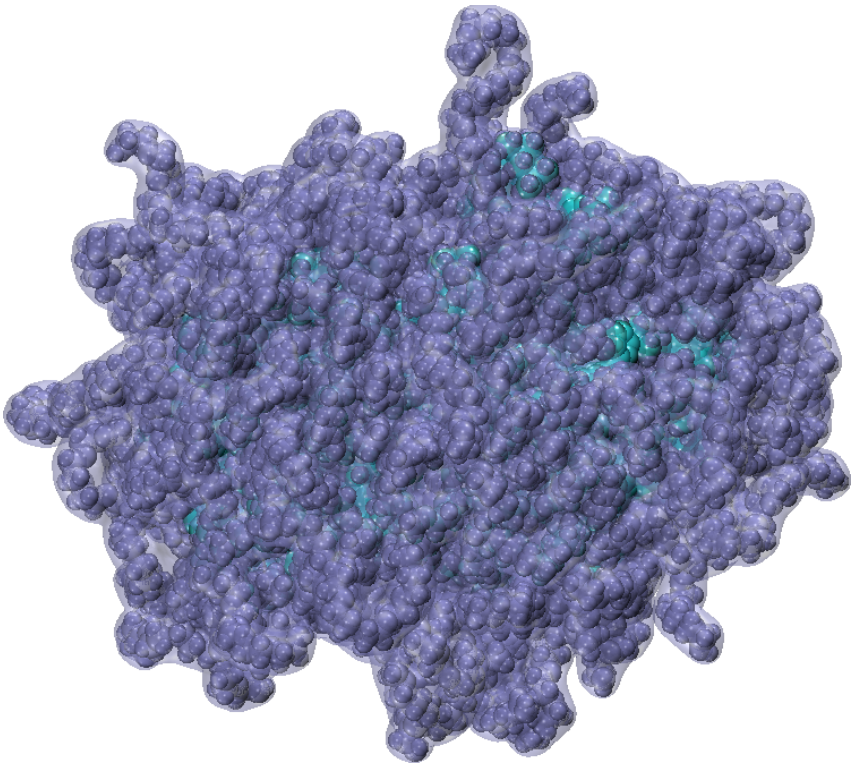


Figure 1.6: Snapshot of Tyloxapol-based nanoparticle. Cyan coloring corresponds to the hydrophobic core of the micelle.

simulations, that pre-assembled micelles and micelles that were self-assembled from surfactants placed randomly in the solution, end up being structurally very similar.[129] The research reported in this thesis was conducted by first pre-assemblying the micelles of interest. Figure 1.6 shows an example of pre-assembled and equilibrated micelle in MD.

1.5.3 Computer simulations as complementary to experiments

Computer simulations are gaining increased popularity as a stand-alone tool, as well as a complementary tool to experiments. In an analysis performed by Web of Science in 2018, it was shown that the number of papers related to MD has grown exponentially over the years.[130] Simulations are now widely used to guide experimental work, as a filter and testing tool for the materials to be used in experiments, and they may even provide a degree of validation for them. One particular advantage of using simulations is that various prop-

erties of the system can be investigated at different short timescales, whereas the experimental methods provide time- and space-averages of aforementioned properties. In this sense too, computer techniques prove to be a great addition to our experimental toolbox. MD is being used extensively in recent years to shed more light on Alzheimer's, Aβ plaque formation in the brain and for development of new therapeutics.[131–134] Manglik et al.[135] used molecular docking to sample millions of substances and identify new ligands for μ-opioid receptors. McCorvy et al.[136] used a combination of docking and MD simulations to suggest a strategy of G protein-coupled receptor (GPCR) selective ligand development. Carlos et al.[137] used computational simulations alongside with neutron diffraction experiments to understand short-range-order of carbon tetrachloride in its liquid and rotator phases. Other examples of MD simulations used as a complement to neutron and X-ray diffraction, include the investigation of methylchloromethane compounds, where an excellent agreement between the values of thermodynamic properties from simulations and experiments was found,[138] and the investigation of cesium salt clustering, again, carrying good accord between the two methods.[139] Finally, Takemoto et al.,[140] alongside with the experiments, applied MD to understand the photocycle of the channelrhodopsin light-gated ion channels. These examples, of course, are but a fraction in wide range of studies, where computational modelling supports experiments.

1.5.4 Simulations of surfactant systems

The first simulations of surfactant molecules were done by Larson in 1988,[141,142] where surfactants in a lattice model were simulated using the Monte Carlo method in different ratios of oil-to-water allowing phase diagrams and free energies to be computed. Early MD simulations of surfactants using the same lattice model were carried out by Smit et al.[143,144] These simulations showed the appearance of surfactant monolayer at water-oil interface, as well as micelle formation separated from the monolayer by a water layer. Oil solubilization in surfactant micelles was simulated by Karaborni.[145] Furthermore simulations

of surfactant interactions with lipid bilayers were done.[146–148] Bandyopadhyay simulated DMPC bilayer in the presence of sodium dodecyl sulfate (SDS) anionic surfactant, which showed an increase of d-spacing and decrease of average area per lipid of the membrane, compared to either pure SDS and pure DMPC bilayer.[149] The loading and release of poorly-soluble molecules in poly-ethylene glycol-based surfactant micelles was investigated in several studies.[150–152] Finally, some computational work has been done in protein denaturation by surfactants. Poghosyan et al. investigated the SDS induced denaturation of ACBP protein.[153] SDS induced denaturation of ubiquitin is currently being investigated experimentally combined with MD simulations by myself in collaboration with Dr. Armen Poghosyan and Prof. Daniel Otzen.

TX100, used in this research, was also studied to a significant extent. Coal wetting by TX100 surfactant was investigated by Liu et al.,[154] while Fatemi et al.[155] found that TX100 molecules accelerate carbon nanotube dispersion. However, TX114 has not been studied to the same extent with MD simulations. Yordanova et al.[111] parameterized TX114 and TX100, and kindly provided them for our research. In the first part of this study (included in this thesis), drug carrying capabilities of two non-ionic surfactant micelles (TX100 and TX114) were investigated. A significant change in shape is observed as micelles are encapsulating more drugs. In two cases, we have seen a disruption of the initial micelle, as it solubilizes a certain amount of drugs, up to the point where it splits into two individually stable daughter micelles.

In the next chapter of this thesis, we will discuss the computational methods, their inner workings, and a review of different analysing techniques and tools applied in this research. A novel method to compute intrinsic surfaces of aspherical nanoparticles is also described. Chapters 3 and 4 will investigate TX100 and TX114 non-ionic surfactant-based micelles respectively, and their capabilities as poorly soluble drug carriers. Chapter 5 will describe a recently developed Python[156] package, and techniques to drastically speed-up compu-

tationally intensive code execution. Finally, chapter 6 examines the effect of cross-linking between surfactant monomers on shape and stability of resulting micelles. Trimers and heptamers of TX100 surfactant are used.

Chapter 2

Methods

2.1 Molecular Dynamics

Molecular dynamics (MD) is a computational method that provides a deterministic description of the dynamical evolution of a system. It is done by iteratively solving the classical equations of motion for a N-particle system. In this chapter, an in-depth discussion of MD simulations will be provided.

2.1.1 Equations of motion

In classical mechanics, the Lagrangian for a system is defined as:

$$L(\dot{\mathbf{q}}, \mathbf{q}) = K(\dot{\mathbf{q}}) - U(\mathbf{q}) \tag{2.1}$$

where K and U are the total kinetic and potential energy of the system, respectively, and q is the set of generalized coordinates. Kinetic energy is a function of velocity of the particle:

$$K(\dot{\mathbf{q}}_i) = \frac{m_i \dot{\mathbf{q}}_i^{\,2}}{2} \tag{2.2}$$

where m_i and $\dot{\mathbf{q}}$ are the mass and the total derivative of the position with respect to time of the i-th particle. On the other hand the potential energy is independent of velocity and can be expressed as a function of coordinates. Therefore, the Lagrangian can be written as:

$$L(\dot{\mathbf{q}}, \mathbf{q}) = \frac{m\dot{\mathbf{q}}^2}{2} - U(\mathbf{q}) \tag{2.3}$$

One of the forms of the equations of motion for N-particle system is defined using the following Lagrangian:

$$\frac{d}{dt}(\frac{\partial L}{\partial \dot{q}_i}) - \frac{\partial L}{\partial q_i} = 0 \tag{2.4}$$

Using the definition in equation 2.3, and swapping the generalized coordinates and their derivatives with Cartesian coordinates and velocities one would get:

$$m\dot{\mathbf{v}}_i + \nabla_i U(\mathbf{r}) = 0 \tag{2.5}$$

$$m\mathbf{a}_i = -\nabla_i U(\mathbf{r}) = \mathbf{f}_i \tag{2.6}$$

where $\mathbf{f}$ is the total force acting on i-th particle. At each step of a MD simulation, net forces on each particles are calculated from the given potential energy function. The exact form of the potential energy in a molecular dynamics engine is given by force-fields, which will be discussed in the next section.

2.1.2 Force field

The force field is the functional form function used in MD simulations to calculate the potential energy of the system. It defines the inter- and intramolecular interactions between particles in the system. The exact forms of these functions and associated parameters are derived empirically as well as from quantum mechanical calculations.[157–159] The basic form of a force field can be expressed as the following equation:[160]

$$U(\mathbf{r}) = U(\mathbf{r})_{bonded} + U(\mathbf{r})_{non-bonded} \tag{2.7}$$

where bonded refers to the potential energy due to chemical bonds, and relative angles between particles inside of a molecule. The non-bonded term includes intra- and intermolecular electrostatic and Van der Waals interactions.

The exact definition of the potential energy function varies in different force fields. In the context of this thesis, where the CHARMM force field[161–163] was used exclusively, its form will be presented.

$$
\begin{aligned}
U = & \sum_{bonds} k_b(r_{ij} - r_0)^2 + \sum_{angles} k_\theta(\theta_{ijk} - \theta_0)^2 + \\
& \sum_{dihedrals} k_\phi(1 + cos(n\phi_{ijkl} - \delta)) + \sum_{impropers} k_\omega(\omega_{ijkl} - \omega_0)^2 + \\
& \sum_{Urey-Bradley} k_u(l_{ik} - l_0)^2 + \\
& \sum_{non-bonded} \left(4\epsilon \left[\left(\frac{\sigma}{r_{ij}} \right)^{12} - \left(\frac{\sigma}{r_{ij}} \right)^{6} \right] + k_e \frac{q_i q_j}{r_{ij}} \right)
\end{aligned}
\tag{2.8}
$$

The first four terms of equation 2.8 are bonded terms. k_r, k_θ, k_ϕ and k_ω are the force constants for bonded interactions, interactions due to angles, dihedrals and improper dihedrals respectively. r_0 is the bond length between i and j particles at rest. θ_0 is the equilibrium angle between ijk connected particles. In the dihedral term, n is the multiplicity, the number of minima around $ijkl$ dihedral angle, which is usually set to 3. An improper angle refers to the angle between ijk plane and jl bond in case when not all the atoms are covalently connected. The CHARMM force-field uses an extra special Urey-Bradley potential term for 1-3 interactions. l_{ik} is the distance between 1-3 bonded atoms and l_0 is the equilibrium distance. This term was introduced as an additional correction for 1-3 angle potential. The last term is the sum of electrostatic and Van der Waals interactions between particles, where ϵ and σ are the Lennard-Jones coefficients, k_e is the Coulomb constant, and q_i and q_j are the charges of particles i and j, respectively. It is worth noting, that in classical potentials, due to the harmonic representation of covalent bonds, their cleavage is impossible. It is possible to model the breakage of bonds by changing the bond potential term to, e.g. Morse potential, and several force fields have implemented it.[164,165] The various terms in the forcefield and their

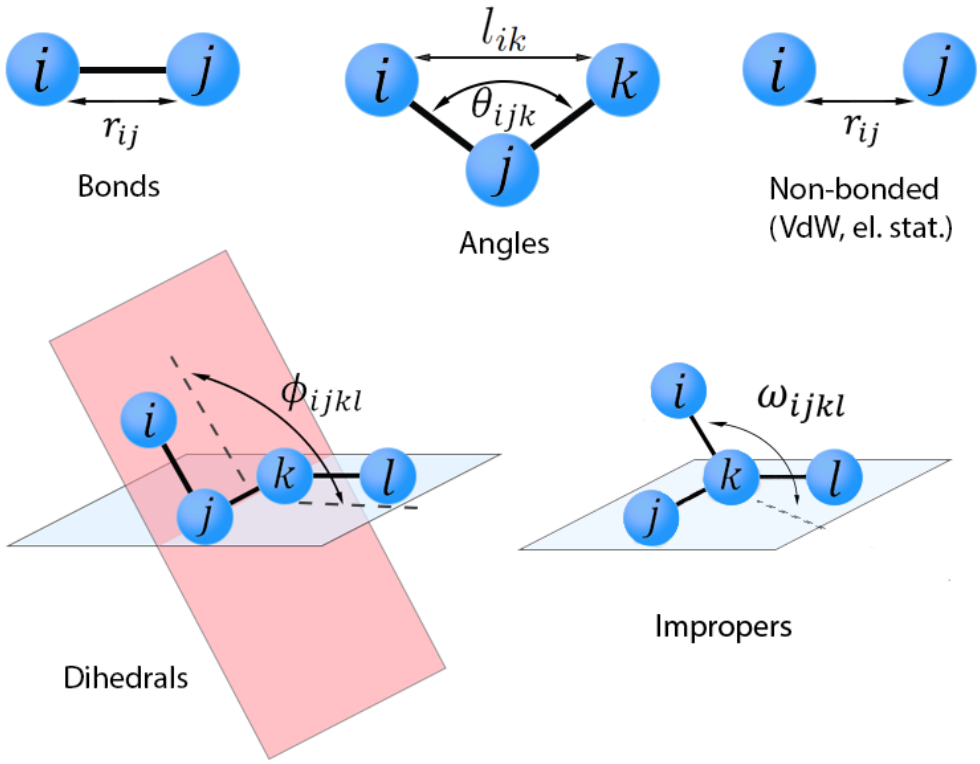


Figure 2.1: Potential terms used in classical MD force field

associated parameters are visualized in Figure 2.1.

The actual parameters may be specific to a force field, as well as to different versions of the same force field. These parameters are obtained from quantum mechanical (QM) calculations, spectroscopic measurements, etc.[166,167] The mentioned methods are especially helpful when acquiring bonded parameters.

Finally, molecules can be modelled with all-atom (AA), united-atom (UA) and coarse-grained (CG) representations. All-atom force fields provide parameters for every atom, including hydrogens, whereas united-atom treats hydrogen-carbon pairs in methyl groups as one particle. Coarse-grain forcefields unite specific functional groups of several atoms into one bead, and are parameterized accordingly. A widely popular Martini forcefield[168,169] does so by mapping in average of 4 atoms to one bead, and is defining four main atom types, polar, non-polar, apolar and charged (Figure 2.2). AA force fields are the most accurate and detailed, but computationally expensive, whereas CG

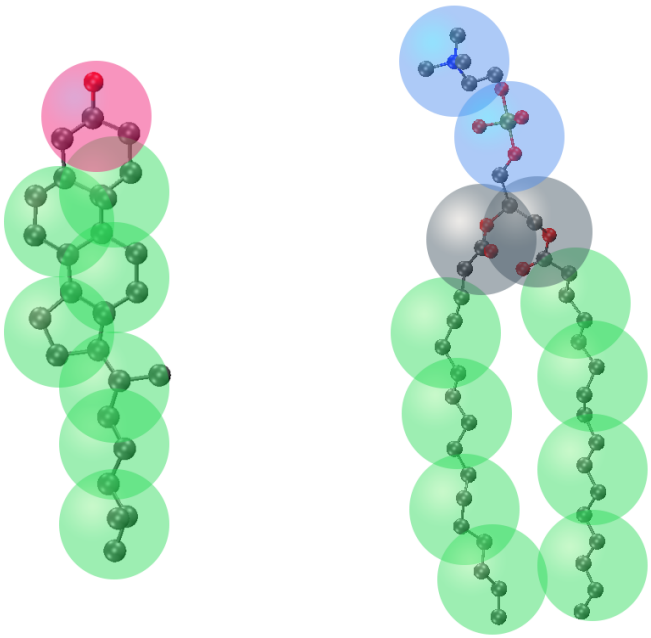


Figure 2.2: Martini force-field mapping schematics. Red, blue, grey and green are respectively charged, polar, non-polar and apolar type beads.

models contain much fewer particles than their AA counterparts, and can simulate systems over significantly longer timescales by sacrificing some chemical features of the system.

2.1.3 Verlet integration

It has been discussed, in theory how the motion of a particle is calculated in a MD simulation. In this section the actual integration algorithm used in a simulation engine will be discussed.

The idea is as follows: given the position, r, and the velocity, v, of a particle at a certain time, t, calculate the position and velocity at time $t + \delta t$, where δt is a short timestep, typically in the order of femtoseconds. The Taylor expansion for position at $t + \delta t$ will be the following:

$$\mathbf{r}(t + dt) = \mathbf{r}(t) + \dot{\mathbf{r}}(t)dt + \ddot{\mathbf{r}}(t)\frac{dt^2}{2} + ... \tag{2.9}$$

By neglecting the terms after the linear term, and solving for the velocity, the following equation is obtained:

$$\dot{\mathbf{r}}(t) = \mathbf{v}(t) = \frac{\mathbf{r}(t+dt) - \mathbf{r}(t)}{dt} \tag{2.10}$$

The exact analytical solution to this equation when $dt \to \infty$, cannot be solved computationally. An approximation can be done by choosing a small enough Δt. This is called finite-difference approximation.

$$\mathbf{v}(t) \approx \frac{\mathbf{r}(t+\Delta t) - \mathbf{r}(t)}{\Delta t} \tag{2.11}$$

In MD simulations, there are some criteria that an integration algorithm must follow. It should ensure the conservation of energy and momentum, and it should be time-reversible.[170] The Velocity Verlet algorithm satisfies both of those conditions. In its explicit form, the Velocity Verlet algorithm can be written as the following set of equations:

$$\mathbf{v}(t + \frac{\Delta t}{2}) = \mathbf{v}(t) + \frac{\Delta t}{2}\mathbf{a}(t) \tag{2.12}$$

$$\mathbf{r}(t + \Delta t) = \mathbf{r}(t) + \Delta t \mathbf{v}\left(t + \frac{\Delta t}{2}\right) \tag{2.13}$$

$$\mathbf{v}(t + \Delta t) = \mathbf{v}\left(t + \frac{\Delta t}{2}\right) + \frac{\Delta t}{2}\mathbf{a}(t + \Delta t) \tag{2.14}$$

Firstly, the velocity for a half timestep is calculated. After that, new positions are calculated based on the new velocity. Finally, velocity at time $t + \Delta t$ is calculated and the next iteration commences. Note, that in between equations 2.13 and 2.14, the new acceleration is calculated based on the new coordinates from potential function:

$$\mathbf{a}(t + \Delta t) = -\frac{1}{m}\frac{dU(\mathbf{r}(t + \Delta t)}{d\mathbf{r}} \tag{2.15}$$

To ensure conservation laws are obeyed, Δt in Velocity Verlet algorithm is limited to 1 fs. This is due to inter-atomic bond vibrations, which have frequencies on a similar time scale,[171] as setting a higher time-step may result in the "blow up" of the system and violation of the conservation of energy. How-

ever, constraint algorithms can be used to hold the bond oscillation frequencies at their equilibrium values, thus allowing for larger timesteps. LINCS[172] and SHAKE[173] are examples of such algorithms. A timestep of 2 fs was used in every simulation within this thesis.

2.1.4 Periodic boundary condition

The number of atoms in a typical MD simulation nowadays can be in range of $10^5 - 10^6$, which is still a tiny number compared to the number of atoms, for example, in a mole ($\sim 6 \times 10^{23}$). In MD simulations, the system of particles is put in a simulation box. The boundaries of the box act as barrier potentials for atoms, which is undesirable when simulating a bulk of a liquid. To overcome this issue, periodic boundary conditions (PBC) are introduced. They are implemented by infinite repetitions, or images, of the simulation box along all dimensions. When an atom from the simulation box reaches and crosses a boundary, an image of that atom enters the box from the opposite side. A 2D visualization of PBC is shown in Figure 2.3.

The most computationally expensive task in MD is the calculation of potentials and forces at each timestep. Without PBC, the calculation of the net force on particle i would require determining the potential energy due to the rest of the N particles. When we introduce PBC, N, practically, tends to infinity as a result of having an infinite lattice of the images of our simulation box. To overcome this, a minimum image convention has been proposed.[113] This means, that the short-range interactions of the particle in question are limited to a cubic region with dimensions of the box and centered around the particle in question. In Figure 2.3, dashed lines represent that region for the green particle. In purple, are the original particles or the images of particles with which the green particle will interact, whereas the particles from the original box outside of the interaction region are grey. This limits the number of interactions to $N(N-1)/2$, which is computationally feasible. Long-range interactions that can span across multiple box images, are handled differently, and will be discussed in the next section.

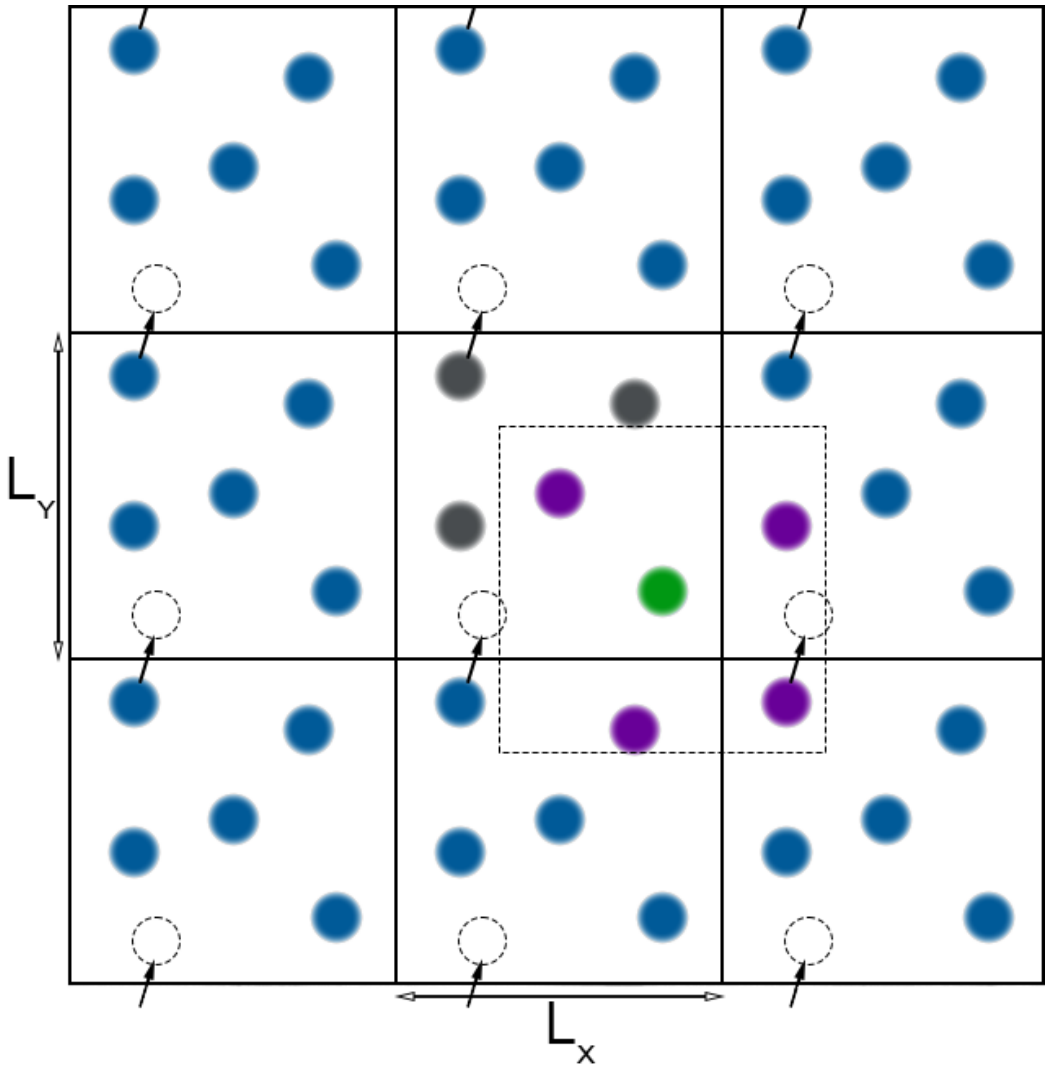


Figure 2.3: Periodic boundary conditions visualized in 2D

2.1.5 Calculation of forces

In equation 2.8, the non-bonded interactions are comprised of van der Waals and Coulomb terms. The corresponding forces in a MD simulation are calculated from the negative gradient of the potential energy function, U, shown in Equation 2.8:

$$\mathbf{F} = -\nabla U(\mathbf{r}) \tag{2.16}$$

The van der Waals term is usually expressed via the Lennard-Jones potential:

$$U_{LJ}(\mathbf{r}) = 4\varepsilon \left[\left(\frac{\sigma}{r_{ij}} \right)^{12} - \left(\frac{\sigma}{r_{ij}} \right)^{6} \right] \tag{2.17}$$

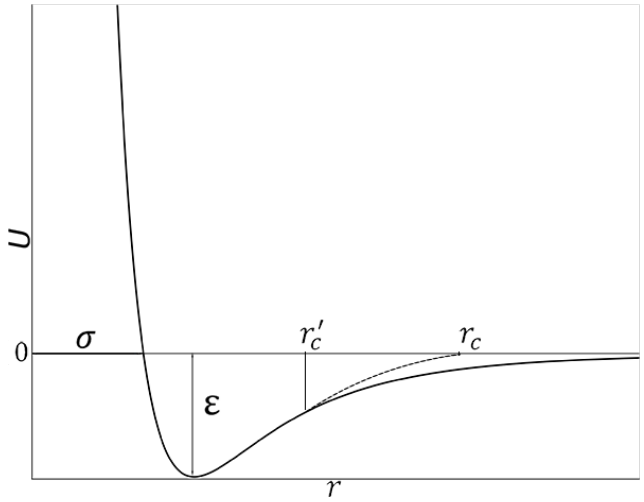


Figure 2.4: Lennard-Jones potential

where ϵ is the depth of the potential well, and σ is the distance at which the potential energy is 0 (Figure 2.4). The first term is considered as the repulsion term, as it is predominate when $r < \sigma$, and the second term represents the attraction between two particles. The Lennard-Jones potential quickly decays as we move further from the particle. This allows having a cut-off at some distance r, so the potential can be written as:

$$U_{LJ\ cut-off}(\mathbf{r}) = \begin{cases} U_{LJ}(\mathbf{r}), & \text{if } r < r_c \\ 0, & \text{if } r > r_c \end{cases} \tag{2.18}$$

This representation, however, is not continuous, and may violate the conservation of energy. Another approach to this, is to use a special "switching" function $S(\mathbf{r})$, which smooths the decay of U_{LJ}. A representative curve is shown as dashed on Figure 2.4.

$$U_{LJ\ smooth}(\mathbf{r}) = \begin{cases} U_{LJ}(\mathbf{r}), & \text{if } r < r_c' \\ U_{LJ}(\mathbf{r})S(\mathbf{r}), & \text{if } r_c' < r < r_c \\ 0, & \text{if } r > r_c \end{cases} \tag{2.19}$$

The long-range electrostatic interactions decay much slower (r^{-1} in the case of particle-particle potential), and they can span across multiple images

of the simulation box, therefore even if a large cut-off is used, it would still be computationally intensive to explicitly calculate the electrostatic interactions between each pair of atoms. In order to improve the efficiency of the determination of these long range interactions, algorithms have been developed in which the electrostatic interaction between only pairs of atoms that are within the LJ cutoff of one another are determined by explicitly calculating the Coulombic interation and then for distances larger than the cutoff an Ewald summation method is used.[174] Particle-mesh Ewald (PME)[175] is an algorithm, developed based upon the Ewald sum, with a reduced time complexity ($O(N\log(N))$ instead of $O(N^{\frac{3}{2}})$), and is the most commonly used Ewald sum implementation in molecular dynamics simulation algorithms.

2.1.6 Thermodynamic ensembles

When discussing the motion of particles in a MD simulation, an assumption was made that the total energy of the system with N particles is constant. This is microcanonical ensemble, or NVE (constant number of particles, N, volume, V, and total energy, E). In real-life experiments, temperature and pressure are regulated by coupling the experimental region with a thermostat or a barostat. In MD, this conditions can be represented by the canonical, NVT (constant number of particles N, volume, V and temperature, T) and isothermal-isobaric ensembles, NPT (constant number of particles N, pressure P, temperature T). This is achieved by coupling the system with a thermal, and/or pressure "bath" using thermostats and barostats. The following subsections will briefly introduce some of the common implementations of those.

Thermostats

The temperature of a system at a given moment can be expressed through the average kinetic energy of all particles:

$$\frac{3}{2}k_bT(t) = \sum_i K_i = \sum_i \frac{m_i\mathbf{v}_i^2}{2} \tag{2.20}$$

where $T(t)$ is the temperature at instance t and k_b is the Boltzmann

constant. Some of the earliest implementations of thermostats are based on rescaling velocities inside of the system after each timestep by a factor, λ, that can be derived[176] from equation 2.20 and written as:

$$\lambda = \sqrt{\frac{T_o}{T(t)}} \tag{2.21}$$

where T_0 is the target temperature and $T(t)$ is the temperature at time, t. Another method uses an extended Lagrangian by adding an additional variable to it.

Berendsen thermostat

The Berendsen thermostat[177] is based on the first method. At each step, velocities are rescaled so that the rate of temperature change is proportional to the temperature difference:

$$\frac{dT(t)}{dt} = \frac{1}{\tau}(T_0 - T(t)) \tag{2.22}$$

where τ is the coupling parameter. The rescaling factor in Berendsen thermostat is the following:

$$\lambda = \sqrt{1 + \frac{\Delta t}{\tau_b}\left(\frac{T_0}{T(t)} - 1\right)} \tag{2.23}$$

where Δt is the timestep, and τ_b is the time constant. When $\tau_b \to \infty$, the thermostat is inactive, resulting in a microcanonical ensemble. Studies show, that Berendsen thermostat does not produce a correct canonical ensemble, therefore it is not recommended for usage in production simulations.[178,179] However, due to the speed of the algorithm and its ability to relax the system to the desired temperature quickly, it is widely used in the equilibration steps of MD.

Nosé-Hoover thermostat

The Nosé-Hoover algorithm[180,181] introduces an additional "bath" variable, with a corresponding mass, Q, and coordinates, $\mathbf{s}$, to the Lagrangian of the system:

$$L(\dot{\mathbf{q}}, \mathbf{q}, \dot{\mathbf{s}}, \mathbf{s}) = \frac{m\dot{\mathbf{q}}^2}{2} - U(\mathbf{r}) + \frac{Q\dot{\mathbf{s}}^2}{2} - \bar{U}(\mathbf{s}) \tag{2.24}$$

where $\bar{U}(\mathbf{s})$, is the "potential energy" due to the newly introduced variable, $\mathbf{s}$. Then, the equations of motion could be rewritten as:

$$\ddot{\mathbf{r}} = \frac{\mathbf{F}}{m} - \gamma\mathbf{r} \tag{2.25}$$

and:

$$\dot{\gamma} = -\frac{1}{\tau_{nh}}\left(\frac{T_0}{T(t)} - 1\right) \tag{2.26}$$

where:

$$\gamma = \frac{\dot{\mathbf{s}}}{\mathbf{s}} \tag{2.27}$$

where τ_{nh} is the Nosé-Hoover time constant and γ is the thermodynamic friction coefficient. This method correctly samples the canonical ensemble and is most commonly used in production runs.

Barostats

Berendsen barostat

The Berendsen barostat is similar to the Berendsen thermostat. The change of pressure in time is proportionate to the difference in pressure:

$$\frac{dP(t)}{dt} = \frac{1}{\tau}(P_0 - P(t)) \tag{2.28}$$

At the end of each simulation step, a rescaling is applied to the box size and coordinates.[177] The rescaling factor is:

$$\mu = \sqrt[3]{\left(1 + \frac{\Delta t}{\tau_b}\beta(P(t) - P_0)\right)} \tag{2.29}$$

where β is the isothermal compressibility, $P(t)$ is the instantaneous pressure and P_0 is the target pressure.

Parinello-Rahman barostat

Much like the Nose-Hoover thermostat, the Parinello-Rahman barostat adds an additional, pressure coupling term into the Lagrangian equation of motion. In a physical sense, that term can be thought of as a piston, that is able to move up and down, and therefore changing the pressure and the volume of the simulation box. In this approach, the box dimensions are time-dependent. A matrix h is defined as:

$$h = \{\mathbf{a}(t), \mathbf{b}(t), \mathbf{c}(t)\} \tag{2.30}$$

Position of each particle therefore will be:

$$\mathbf{r}_i = \alpha_i \mathbf{a}(t) + \beta_i \mathbf{b}(t) + \gamma_i \mathbf{c}(t) = h\mathbf{s}_i \tag{2.31}$$

where α, β and γ are scalars in the range of 0 to 1, and $s = (\alpha, \beta, \gamma)$. The square of the position will be, $\mathbf{r}_i^2 = \mathbf{s}_i^T G \mathbf{s}_i$, where $G = h^T h$ is the metric tensor. The lagrangian, therefore, can be written as:

$$L(\dot{\mathbf{s}}, \mathbf{s}, \dot{h}, h) = \frac{m\dot{\mathbf{s}}_i^T G \dot{\mathbf{s}}_i}{2} - U(\mathbf{s}) + \frac{W \mathrm{Tr}(\dot{h}^T \dot{h})}{2} - p_{ext} V \tag{2.32}$$

where p_{ext} is external pressure, V is the volume of the cell. The equations of motion derived from this extended Lagrangian can be found in the original paper by Parinello and Rahman.[182]

This is not an exhaustive list of thermostats and barostats. There are more algorithms available to apply constant temperature and pressure to a MD system. The ones mentioned in this thesis have been exclusively used for the simulations discussed within the results chapters.

2.1.7 Setting up a simulation

Each MD simulation needs to be carefully set up, before a production run can commence. Firstly, a configuration file must be created, which will represent the system in question. This means, defining the atoms of the system and

assigning their coordinates. There are a lots of ways to do this and many software can ease this process. In simulations conducted for this thesis, the Packmol[183] and GROMACS software packages[184–186] were used to build the initial configuration file. If the system contains a net charge, then this net charge should be neutralised with counter ions. The necessity arises due to the PME method, which might produce artefacts in a system with a net charge.[187]

Energy minimization

During the construction of the initial configuration, the positions of some or all particles are generated randomly, therefore an overlap between atoms, resulting in unnaturally high energies, is possible. These high energy configurations must be corrected in order to proceed with the simulation. This can be done using the gradient descent method. First, the forces and energies are calculated. If any force is greater than the tolerance value (1000 kJ mol^{-1} nm^{-1} in my simulations), the coordinates are shifted along the maximum of the force gradient:

$$\mathbf{r}_{n+1} = \mathbf{r}_n + \frac{\mathbf{F}_n}{max(|\mathbf{F}_n|)} h_n \tag{2.33}$$

where h_n is the maximum displacement and $\mathbf{F}_n$ is the force acting on n-th particle. Then, the forces and energies are calculated again and if $U_{n+1} < U_n$, the new positions, r_{n+1}, are accepted, whereas if $U_{n+1} \geq U_n$, the positions are rejected. In both cases, the displacement, h_n, is changed accordingly for the next step. This process ends when the force values are lower than the tolerance, or user-specified number of steps are finished.

Equilibration

After the minimization step, the velocities for each particle are initialized. Velocities are assigned to each of the atoms according to Maxwell's distribution:

$$\rho(v_{ix}) = \left(\frac{m_i}{2\pi k_b T}\right) e^{-\frac{1}{2}\frac{m_i v_{ix}^2}{k_b T}} \tag{2.34}$$

where m_i and v_{ix} are respectively mass of the i-th particle and the x

component of its velocity. Likewise, the other components are generated. Inevitably, there will be regions in the system with varying densities and temperatures. To even out the densities and to deliver the system to a single, average temperature, an equilibration step is necessary. In this step, the system is coupled with a thermostat and/or a barostat discussed in Section 2.1.6. The duration of equilibration depends on the system (typically order of ns), but generally some parameters, e.g. pressure, energy, can be monitored to see if the system has reached its thermodynamic equilibrium.

2.1.8 Analysis of trajectories

This section will briefly introduce two methods, used and partly developed for this research.

Defining interfaces

Three algorithms for interface definition have been used throughout this thesis. This subsection will provide a brief overview of the inner workings of the aforementioned algorithms.

In Chapter 3, to define the interface and calculate intrinsic densities of different species inside of the system, the nanoCISC[170] algorithm was used. The interface in nanoCISC code is constructed by first defining anchor points, based on which, the interface will be interpolated. Next, two distance vectors are defined, $\mathbf{r}_j$, the distance from the center of mass, c_m, of the nanoparticle to the j-th solvent atom, $\mathbf{s}_i$, the distance from c_m to the i-th anchor point. The distance from the interface to the j-th atom, d_{int}, is defined as the following:

$$d_{int}(\mathbf{r}_j) = |\mathbf{r}_j| - \frac{\sum_{i=1}^{N} \exp\left(-\lambda\theta_{ij}^2\right)|\mathbf{s}_i|}{\sum_{i=1}^{N} \exp\left(-\lambda\theta_{ij}^2\right)} \tag{2.35}$$

where N is the number of anchor points, θ is the angle between the vectors $\mathbf{r}_j$ and $\mathbf{s}_i$ and λ is a parameter determining the smoothness of the interface.

In this method, the densities are determined by dividing the simulation box into spatial intervals and subsequently calculating the ratio of particles in each interval to the volume of that specific interval.

The intrinsic core-shell interface (ICSI) algorithm was used to define the interface of Triton X-114 micelles in Chapter 4. In the ICSI method, instead of anchor points, the residues or moieties that comprise the hydrophobic core of the particle are selected and the interface is automatically constructed. The simulation box is then divided into a user-specified size grid. The location of the ICSI point inside of a bin is chosen as radially the furthest atom from the center of mass of the nanoparticle. If there are no atoms inside the current bin, the average r-value of the adjacent 8 bins is used. The distance from the interface to the i-th atom, d_{int} is then calculated as:

$$d_{int} = r_i - \xi(\theta, \phi) \tag{2.36}$$

where r_i is the position of atom i, ξ is the position of the interface at polar coordinates θ and ϕ.

In Chapter 6, the AICON algorithm was used which is thoroughly discussed in the next subsection.

Identification of the interface of non-spherical nanoparticles

Previously, a few algorithms have been developed to describe the interface of nanoparticles in a MD simulation.[170,188] For spherical or quasi-spherical nanoparticles, these algorithms provide adequate results, however, they are not designed to properly describe the interfaces of elongated or aspherical nanoparticles. The following algorithm was created to address the above-mentioned issue.

The algorithm takes particle groups from the trajectory of a MD simulation, creates a grid of size ($d \times d \times d$), where d is the dimension of the box (considering the box is cubic), and maps the positions of each particle according to this equation:

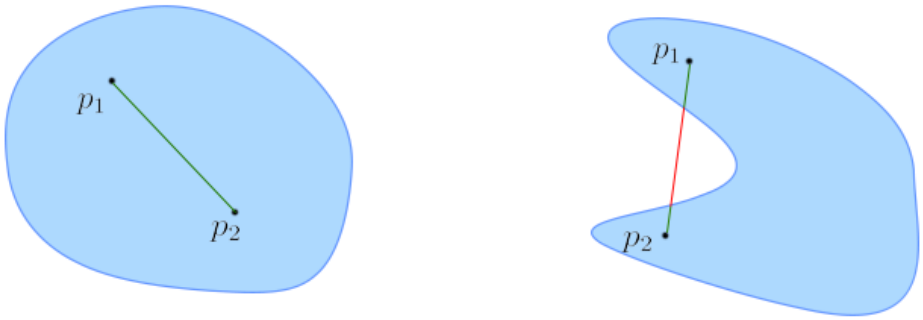


Figure 2.5: Convex and non-convex sets.

$$\begin{aligned} x_{grid} &= \lfloor x \rfloor \\ y_{grid} &= \lfloor y \rfloor \\ z_{grid} &= \lfloor z \rfloor \end{aligned} \tag{2.37}$$

where x_{grid}, y_{grid} and z_{grid} are the mappings of the x, y, z coordinates of a point on the grid. Each of the coordinates is rounded down, and a vector of integers is obtained for each individual particle. That vector represents the coordinates on the grid where the particle will be placed. The number of occupied points on the grid will be $\leq N$, where N is the number of particles. An interface of a nanoparticle is then defined. The interface, in this context, is the border between hydrophobic and hydrophilic regions inside of the system.

Defining the interface. Convex hull

In geometry, a convex set is a subset in Euclidean space, where any two points belonging to the set can be connected by a straight line, that completely lies inside the set (Figure 2.5). The intersection of all convex sets for a given set of points is the convex hull (Figure 2.6). In other terms, the convex hull is the minimal convex set that contains the subset in question.

There are several algorithms developed to calculate the convex hull for a set of points. For simplicity, one of the simplest algorithms will be discussed, which is called the gift wrapping algorithm. The two-dimensional

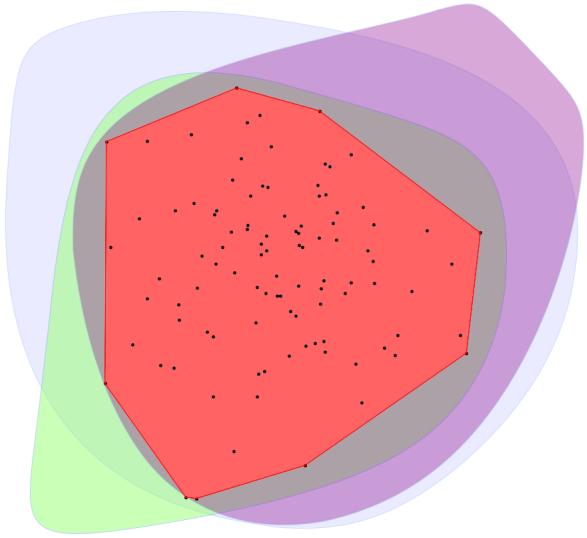


Figure 2.6: Convex hull of set of points (red). Purple, green and blue are all convex sets containing the points. Region in red is the minimal convex set, or the intersection of all convex sets enclosing the points.

case, also known as Jarvis's march, was developed by Jarvis in 1973.[189] In two-dimensions, the algorithm consists of three main steps, 1) taking the leftmost point, p_0, of the set, 2) iterating through all other points and finding p_1, which is leftmost from the others. This can be done by calculating the polar angles of all other points with respect to the selected point. Then, 3) taking p_1 as the initial point and repeating from step 2 to find all points, p_i, on the hull (Figure 2.7). The loop is terminated when $p_i \equiv p_0$. The time complexity of this algorithm is $O(Ns)$ (with a worst case of $O(N^2)$), where N and s are the number of points in the set and on the hull, respectively. This algorithm can be generalized into three dimensions, where the iterations over the points is replaced by iterations over triangles. There are faster algorithms, e.g. quickhull[190] ($O(N \log N)$), which was used in this work.

The interface of a nanoparticle is defined as a 3D convex hull. The particles belonging to the atom group, that represents the interface, are placed on the grid, and the convex hull is constructed.

Neighbour analysis

In the analysis of the trajectories of the mixed surfactant micelles, it is useful to quantify, whether one species of surfactants has selectivity towards itself or the others. If P_1 is the percentage of one type of surfactant in the micelle, and P_2 is the percentage of the other, then non-selectivity would mean that the ratio of the number of molecules of two different neighbouring types would be approximately $\frac{P_1}{P_2}$. A convenient method to quantify the neighbours is the application of graph theory.

Graphs in graph theory, are mathematical structures used to model the relationship between different objects. Graphs consist of nodes and edges, which represent objects and their connectivity respectively. Graphs have an adjacency matrix associated to them. The adjacency matrix is square, and has a dimensionalality n, which is the number of objects. If an element $a_{ij} = 0$, then objects i and j have no connection. Furthermore, a graph can be directed and undirected. Adjacency matrices of undirected graphs are symmetric (Figure 2.8).

Graph theory can be a useful tool for analysing molecular structures and conformational changes by representing individual atoms as nodes, and bonds (covalent, hydrogen) as edges. In this work, graphs were constructed where each node represents the center of mass (COM) of every surfactant monomer. Two nodes are connected, if the distance between corresponding COMs is less than a cut-off, which indicates whether the molecules are at a neighbouring

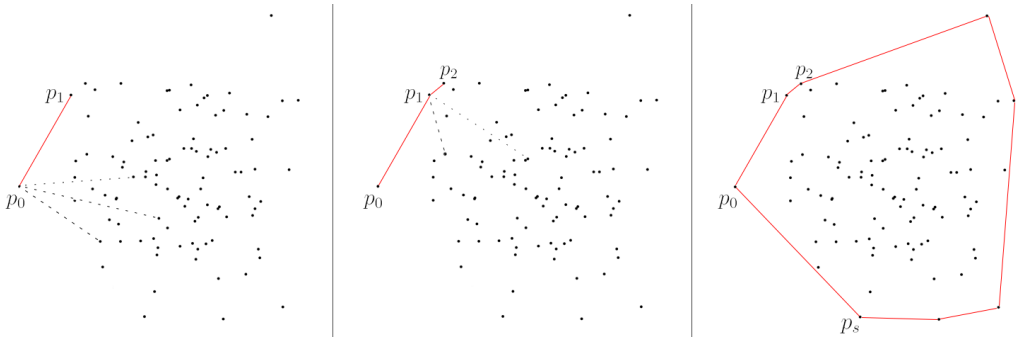
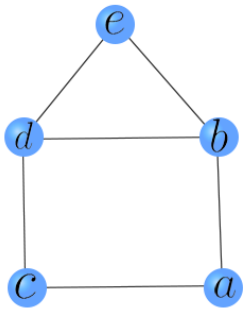


Figure 2.7: 2D gift wrapping algorithm. For every point on the hull, N points are checked to find the next point. s is the number of vertices on the hull.

distance from each other. This allows to conveniently find the neighbours



$$\begin{array}{c|ccccc} & a & b & c & d & e \\ \hline & 0 & 1 & 1 & 0 & 0 \\ & 1 & 0 & 0 & 1 & 1 \\ & 1 & 0 & 0 & 0 & 1 \\ & 0 & 1 & 0 & 0 & 1 \\ & 0 & 1 & 1 & 1 & 0 \end{array}$$

Figure 2.8: A graph and its associated adjacency matrix.

around each surfactant. Additionally, centrality for different nodes in the graph can be calculated, which indicates their position and overall connectivity in the network. The graphs used for the work in this thesis were constructed using NetworkX[191] Python package.

2.1.9 Visuals

The snapshots of various structures used in this thesis were made by Visual Molecular Dynamics (VMD) program.[192,193] Graphs were plotted using Matplotlib[194] library for Python.[156] The refinements on some of the existing images used and the creation of the rest of the images were done using Adobe Photoshop 2021.[195]

Chapter 3

Impact of drug aggregation on the structural and dynamic properties of Triton X-100 micelles

The following chapter investigates the solubilization of poorly-soluble drugs within non-ionic surfactant Triton X-100-based micelles. Ibuprofen and indomethacin are non-steroidal anti-inflammatory drugs (NSAID), having poor solubility despite the fact of being deprotonated in a neutral pH. In this work, the encapsulation of ibuprofen and indomethacin inside of Triton X-100 micelles, the structural changes of the micelle caused by the drugs, were studied using all-atom molecular dynamics simulations. The capacity of micelles with an aggregation number of 150 were shown. A transition of the micelle from spherical to a rod-like structure, caused by an increasing number of drugs solubilizing inside of it, was seen and quantitatively described. Indomethacin-loaded micelle split into two stable micelles during the simulation, the mechanism of which has been explained and described. Overall, this study provides results, that are crucial in synthesis of new, better and high quality drug formulations.

In this manuscript, the algorithm that is used to measure contacts between

molecules produces a matrix that stores the number of contacts between each pair of molecules within the simulated system. This matrix is then normalized by dividing each entry by the maximum number of contacts between any two pair of atoms. These normalized values are then used to define the 'amount of contact', which is referred to throughout the manuscript.

The article included in this chapter has been published in *Nanoscale* in 2022 with Hrachya Ishkhanyan as its first author. The molecular dynamics simulations were performed and the trajectories were analyzed by Hrachya Ishkhanyan. The scripts and tools for the analysis, unless stated otherwise, were developed by Hrachya Ishkhanyan. The manuscript was written by Hrachya Ishkhanyan and edited by Natasha H. Rhys, M. Jayne Lawrence, Dave J. Barlow and Christian D. Lorenz. SANS experiments were performed and the data was provided by Dave J. Barlow. Figures, diagrams and graphs were produced by Hrachya Ishkhanyan. The supplementary information to this article is shown in Appendix A.

Nanoscale

PAPER

View Article Online
View Journal | View Issue

Check for updates

Cite this: *Nanoscale*, 2022, **14**, 5392

Impact of drug aggregation on the structural and dynamic properties of Triton X-100 micelles†

Hrachya Ishkhanyan,[a] Natasha H. Rhys,[a] David J. Barlow,[b] M. Jayne Lawrence [b] and Christian D. Lorenz *[a]

Surfactants are used in a wide range of chemical and biological applications, and for pharmaceutical purposes are frequently employed to enhance the solubility of poorly water soluble drugs. In this study, all-atom molecular dynamics (MD) simulations and small-angle neutron scattering (SANS) experiments have been used to investigate the drug solubilisation capabilities of the micelles that result from 10 wt% aqueous solutions of the non-ionic surfactant, Triton X-100 (TX-100). Specifically, we have investigated the solubilisation of saturation amounts of the sodium salts of two nonsteroidal anti-inflammatory drugs: ibuprofen and indomethacin. We find that the ibuprofen-loaded micelles are more non-spherical than the indomethacin-loaded micelles which are in turn even more non-spherical than the TX-100 micelles that form in the absence of any drug. Our simulations show that the TX-100 micelles are able to solubilise twice as many indomethacin molecules as ibuprofen molecules, and the indomethacin molecules form larger aggregates in the core of the micelle than ibuprofen. These large indomethacin aggregates result in the destabilisation of the TX-100 micelle, which leads to an increase in the amount of water inside of the core of the micelle. These combined effects cause the eventual division of the indomethacin-loaded micelle into two daughter micelles. These results provide a mechanistic description of how drug interactions can affect the stability of the resulting nanoparticles.

Received 2nd December 2021,
Accepted 15th March 2022

DOI: 10.1039/d1nr07936k

rsc.li/nanoscale

Introduction

Without a drug delivery vehicle (DDV), consistent *in vivo* drug concentrations would be difficult to ensure which then would lead to unpredictable effectiveness and safety of the therapeutic treatment.[1,2] With the advances of nanomedicine, more stable, controllable and precise drug delivery is possible.[3–6] Increasingly drugs are loaded into nano-sized vesicles, which are constructed and optimised for the nature of the drug and its biological target.[7,8] DDVs including nano-sized carriers offer a wide range of advantages including greater drug solubility, lower toxicity and more targeted delivery. With their high surface area to volume ratio, nano-carriers are used to solubilise small drug molecules, nucleic acids, and proteins with good efficiency and are used for targeted as well as non-targeted therapy.[9]

A popular family of nano-DDV are self-assembled structures, which are cost efficient and simple to make. Self-assembly is the process of the organisation of materials into structures based on non-covalent interactions. Alongside the self-assembled structures abundant in nature, artificially designed ones are of great interest in biomedical applications, particularly as antimicrobial and detection agents[10] or drug delivery vesicles.[11–13] There is a vast range of materials such as biopolymers, peptides, nucleic acids and inorganic compounds used as building blocks for self-assembled structures.[14–16] Peptides can be self-assembled into nanotubes preserving their biological recognition properties and used in microelectronics to easily construct electrical circuits[17] while nucleic acids and surfactants can be self-assembled into structures suitable for drug delivery.[18,19]

Surfactants are surface active molecules widely used as solubilising agents, emulsifiers, antimicrobial agents, and drug and gene delivery systems.[20,21] Traditional surfactants are low molecular weight amphiphiles that in aqueous solution can self-assemble into various structures such as micelles or

[a]*Biological & Soft Matter Research Group, Department of Physics, Faculty of Natural, Mathematical & Engineering Sciences, King's College London, London, UK. E-mail: chris.lorenz@kcl.ac.uk*
[b]*Division of Pharmacy and Optometry, School of Health Sciences, Faculty of Biology, Medicine and Health, University of Manchester, Stopford Building, Oxford Road, Manchester, UK*

†Electronic supplementary information (ESI) available: Packmol input for building initial micelle; radial distribution functions for water around polar atoms in ibuprofen and indomethacin; contact maps of indomethacin and ibuprofen in their crystalline structures; snapshots of representative configurations showing the interactions between indomethacin and ibuprofen encapsulated within Triton X-100 micelles and between the Triton X-100 tails; plots showing the amount of water found in the core of the different micelles. See **https://doi.org/10.1039/d1nr07936k**

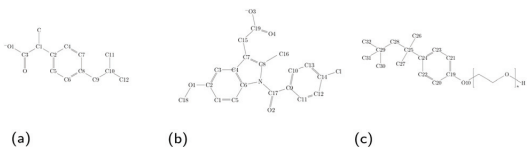
This journal is © The Royal Society of Chemistry 2022

liposomes. There are four main categories of surfactants classified on the basis of their charge: non-ionic, cationic, anionic and zwitterionic. Due to their ability to self-assemble, surfactant micelles are easy to produce and consequently have a low production cost. Additionally, micelles have a large drug solubilisation capacity and can increase the bioavailability of poorly soluble drug molecules. Therefore surfactants, particularly the non-ionic variety, are attractive candidates when forming drug delivery vesicles.

In this work, we investigate the structural properties and drug solubilisation capabilities of Triton X-100 (TX-100) (Fig. 1c) micelles using a combination of all-atom molecular dynamics (MD) simulations and small-angle neutron scattering (SANS) experiments. TX-100 is a non-ionic surfactant with a hydrophilic polyethylene oxide headgroup and a hydrophobic tail. TX-100 is widely used for protein and cell organelle extraction, cell lysation, and membrane permeabilisation.[22,23] More recently, TX-100 has become increasingly investigated for its application in drug delivery.[24–27]

The self-assembly of TX-100 surfactant molecules into micelles in an aqueous environment has been extensively investigated experimentally.[28–30] The first average aggregation number and molecular weight of the resulting TX-100 micelles was determined using static light scattering by Kushner and Hubbard in 1954.[31] The size and shape of the TX-100 micelles in different solvent environments and at different temperatures has also been investigated in numerous studies.[29–34] However, to date there is still no consensus about the shape of TX-100 micelles in an aqueous environment. For example, Robson and Dennis used the results of hydrodynamic and viscosity measurements to argue that TX-100 micelles are non-spherical in shape.[30] Paradies[29] and Podo *et al.*[35] used the results of Nuclear Overhauser Effect SpectroscopY (NOESY) NMR and hydrodynamic measurements to suggest that at low aggregation numbers the shape of TX-100 micelles is slightly non-spherical, and as the aggregation numbers increase the micelles become increasingly non-spherical.

While there has been a significant amount of experimental investigation of the structural properties of self-assembled TX-100 micelles there have been comparatively few investigations of these micelles using MD simulations. Yordanova *et al.* reported the CHARMM force field parameters for Triton X series surfactants.[36] Also, Milano *et al.* have used all-atom and coarse-grain simulations, as well as their MD-self-consistent field theory (MD-SCF) approach, to explore the self-assembly of TX-100 and the structure and shape of the resultant micelles.[37,38] In their original paper, they report on numerous structural properties of TX-100 micelles in aqueous solutions and show that the shape of the micelles become increasingly non-spherical as the aggregation number of the micelle increases. While in their more recent paper, they show that the transition from the more spherical micelles to the more non-spherical micelles is a result of the energetic cost due to the growth of the interfacial region, and the resulting larger hydrophobic surface exposed to the aqueous environment, as the aggregation number increases.



(a) (b) (c)

Fig. 1 Structures of molecules in simulations, including (a) the ibuprofen ion, (b) the indomethacin ion and (c) the TX-100 surfactant molecule.

In our study, we investigate how the solubilisation of two non-steroidal anti-inflammatory drugs (NSAIDs), ibuprofen ($C_{13}H_{18}O_2$) and indomethacin ($C_{19}H_{16}ClNO_4$) (chemical structures shown in Fig. 1),[39–41] affects the structural properties of TX-100 micelles. Both drug molecules contain a benzene ring and carboxyl group, which has a low pK_a [42] resulting in both drugs being deprotonated at neutral pH. Despite being deprotonated, both molecules are poorly soluble in aqueous solutions, and therefore in order to increase their bioavailability they are best solubilised in some kind of a drug delivery vehicle. Previously, Bahadur *et al.* have investigated the effect of the solubilisation of small molecules within TX-100 micelles.[43,44] In both publications, they have shown that the solubilisation of more hydrophobic small molecules results in the growth of the TX-100 micelles, while the solubilisation of more hydrophilic small molecules results in the micelles staying approximately the same size.

We show here that the sodium salts of both ibuprofen and indomethacin are solubilised within TX-100 micelles. We find that TX-100 micelles consisting of approximately 147 surfactant molecules are able to solubilise approximately twice as much indomethacin than ibuprofen. Once solubilised within the core of the micelles, the drug molecules reorient in order to allow their carboxyl groups to remain hydrated by the water in the aqueous environment surrounding the core of the micelles. We find that there are more extensive interactions between indomethacin molecules than between ibuprofen molecules. As a result, the indomethacin molecules form larger aggregates within the core of the micelle than ibuprofen. Furthermore, we observe that the indomethacin-loaded micelle divided into two after reaching its maximum loading. The division of the indomethacin-loaded micelle is a result of the growth of the solubilised indomethacin aggregates which destabilise the core of the micelle. In the following sections of the manuscript, we present the methods we have used in order to conduct this investigation, and then report on the structural properties of the TX-100 micelles with and without drugs, as well as the drug solubilisation process.

Methods

Molecular dynamics simulations

In this study, three systems (summarised in Table 1) have been investigated with all-atom molecular dynamics simulations

Table 1 Description of the simulated systems. For each simulated system, the system name and the number of drug, Triton X-100 and water molecules are presented. Underlined are the concentration values of Triton X-100 in the system

System	Drug	Triton X-100	Water
TX-100	0	150 (10.0 wt%)	52 266
TX-100-IBUP	100	150 (7.0 wt%)	75 181
TX-100-INDO	100	150 (8.0 wt%)	65 673

using the GROMACS 2018.2 simulation engine.[45–47] The CHARMM36 force-field[48] was used to describe the interactions of the TX-100 molecules[36] and the Na^+ ions in solution. The drug molecules were parameterised using the CHARMM general force field.[49] The interactions of the water molecules were modelled using the CHARMM-modified version of the TIP3P potential.

In order to build an initial configuration of the TX-100 system, we pre-assembled a spherical micelle containing 150 TX-100 surfactant molecules using Packmol.[50] The input code is presented in the ESI.† Then for the systems containing ibuprofen (TX-100-IBUP) and indomethacin (TX-100-INDO) we placed 100 drug molecules randomly around the pre-assembled micelle. In each system, water molecules are then added to fill the simulation box with dimensions of 120 Å × 120 Å × 120 Å for the TX-100 system and 130 Å × 130 Å × 130 Å for the TX-100-IBUP and TX-100-INDO systems (Table 1). In the drug containing systems, we also added 100 sodium (Na^+) ions as counterions to the negatively charged drug molecules.

Each system was simulated using the same protocol. First the system underwent 5000 steps of minimisation with the steepest descent method. Then a 50 ps NVT simulation using the V-rescale thermostat and a 200 ps NPT simulation using the same thermostat and the Berendsen barostat were conducted in order to equilibrate the temperature and pressure of the system, respectively. Finally, a production simulation using the NPT ensemble with the Nosé–Hoover thermostat and Parrinello–Rahman barostat was conducted. The production simulation was run for long enough for the size and shape of the micelle to equilibrate. Therefore, the production simulations were run for 200 ns (TX-100), 300 ns (TX-100-IBUP) and 600 ns (TX-100-INDO) using a timestep of 2 fs. The resulting simulation box sizes were 119.4 Å × 119.4 Å × 119.4 Å, 134.2 Å × 134.2 Å × 134.2 Å and 129.0 Å × 129.0 Å × 129.0 Å for the TX-100, TX-100-IBUP and TX-100-INDO systems, respectively.

In all simulations, the target pressure and temperature were set to 1 atm and 303.15 K respectively. Cut-off distances for Coulomb and Lennard-Jones interactions were set to 1.2 nm. Long-range electrostatic interactions were calculated using the particle-mesh Ewald method. Hydrogen containing bonds were constrained using the LINCS algorithm.[51]

Analysis of MD simulations

The physical properties of each simulated system were analysed using in-house Python scripts and the MDAnalysis package.[52,53] In order to characterise the shape of the micelles, we have calculated the ellipticity of the entire micelle, defined as:

$$\varepsilon = \frac{I_{\max}}{I_{\min}}$$

where $I_{\max}$ and $I_{\min}$ are the largest and smallest terms in a diagonal inertia tensor. For a sphere, ε is equal to 1, and ε increases as the shape becomes increasingly elliptical. The shape of the micelle can be further characterised by comparing the diagonal terms in the inertia tensor. If two axes of the ellipsoid are equal and greater or less than the third axes, the ellipsoid is oblate or prolate respectively. Otherwise, when all three axes are equal, the structure is spherical.

The solvent-accessible surface area (SASA) algorithm represents the surfaces of our micelles as overlapping spheres with van der Waals radii of the corresponding atoms, and uses a probe with a small radius, that is typically 1.4 Å to represent a water molecule, to determine the maximum permitted contact with the surface.[54] In this study, the FreeSASA[55] module was used to calculate the SASA of the various micelles.

In order to determine whether a drug molecule was solubilised in a micelle, we first calculated the distance between the center of mass of drug molecules and the micelle. If the distance is less than 5 Å, the drug is considered to be solubilised. A cut-off distance of 5 Å is chosen as it is roughly the distance to the first neighbouring atom. This value is used throughout the rest of the analysis.

Further analysis was performed to characterise the hydration of drugs throughout the simulation. The number of water molecules around each drug has been plotted against Δr, which is defined as:

$$\Delta r = r_d - r_s$$

where r_d is the distance of a heavy (non-hydrogen) atom of interest in the drug molecule from the center of mass of the micelle, and r_s is the distance of the O10 atom in the surfactant molecule (see Fig. 1c) nearest the drug molecule from the center of mass of the micelle. Thus r_d is the distance of the drug from the centre of the mass of the micelle and r_s is the distance of the interface of the micelle with which the drug is interacting to the centre of mass of the micelle. As a result, if Δr is positive, then the drug is outside of the hydrophobic core, and negative if the drug molecule is solubilised within the core of the micelle.

Finally, drug–drug and drug-TX-100 interactions were characterised by creating contact maps. The distance between the heavy (non-hydrogen) atoms of the molecules of interest that were 5 Å away from one another were considered in contact. The number of contacts were counted between each pair of heavy (non-hydrogen) atoms on the molecules of interest, and then the maximum number of contacts between any two pair of atoms was used to normalise the various values, such that the pair of atoms most frequently in contact had a value of 1.0 in the contact maps.

This journal is © The Royal Society of Chemistry 2022

Small-angle neutron scattering

Small angle neutron scattering (SANS) studies were performed on the SANS2D small angle diffractometer at the ISIS pulsed neutron source (ISIS, Rutherford Appleton Laboratory, STFC, Didcot, Oxford). The SANS2D diffractometer was configured to provide a scattering vector $Q = (4\pi\lambda)\sin(\theta/2)$ in the range of 0.0045 Å^{-1} < Q < 0.4 Å^{-1}. All the protiated surfactant solutions were prepared using D_2O as the solvent. When preparing the solutions with D_2O, the weight ratio of surfactant to D_2O was re-calculated to ensure the molar ratio of surfactant to D_2O was the same as in H_2O. The samples were measured in quartz banjo cells of 2 mm path length. All measurements were performed at 298 ± 0.1 K. The measured SANS data were model-fitted using SasVView.[56] A range of models/scattering form factors ($P(Q)$) including core–shell spheroids (namely sphere, oblate, prolate) and triaxial micelles were considered. As the TX-100 concentrations used were large, it was necessary to account for any interparticulate interactions ($S(Q)$), which was achieved using a hard sphere model. The best model found to fit the data was a core–shell spheroid model. The modelling of the SANS data assumed a flat background correction to allow for any mismatch in the incoherent and inelastic scattering between the samples and solvent and the fitted background levels were checked to ensure they were of a physically reasonable magnitude.

Results

In the following sections we summarise the results from our all-atom MD simulations and compare them to the results of our neutron scattering experiments in order to provide a detailed description of the size, shape and internal structure of a TX-100 micelle. We also provide a detailed description of how these properties change when ibuprofen and indomethacin are loaded within the micelle.

Structural properties of pure Triton X-100 micelles

As can be seen in the snapshot shown in Fig. 2b, the pure TX-100 micelle relaxes into a non-spherical structure. The equilibrated micelle contains an average of 147 TX-100 molecules, with the remaining three molecules in a dynamic equilibrium of joining and leaving the micelle. In order to quantify the shape of this micelle (TX-100), we calculated the ellipticity as a function of time (Fig. 3a). The shape of the TX-100 micelle was found to remain slightly non-spherical throughout the production simulation ($\varepsilon \sim 1.48$) with a prolate shape and a length of 107.8 ± 0.8 Å along the primary axis. Likewise, the measured SASA of the micelle was found to remain nearly constant over time (Fig. 4a), averaging 6.01×10^4 ($\pm 0.01 \times 10^4$) Å^2.

In order to characterise the internal structure of the micelle, we first needed to identify the intrinsic surface of the hydrophobic core of the micelle. In order to identify this intrinsic surface, we used the NANOCISC code.[57] We chose the carbon atom in the aromatic ring of the surfactant (atom C19 in Fig. 1c) bonded to the first oxygen in the polyethyllene oxide (PEO) as the anchor point, which was then used to define the surface of the hydrophobic core of the micelle and was therefore defined as where r = 0 in Fig. 2a and 6. Furthermore, the intrinsic densities of water (using the oxygen atoms in the water molecules) and the TX-100 molecules were calculated (Fig. 2a). At large distances, the number density of the oxygen atoms in the water molecules is 0.033 Å^{-3}, which is consistent with the bulk water density found in our previous

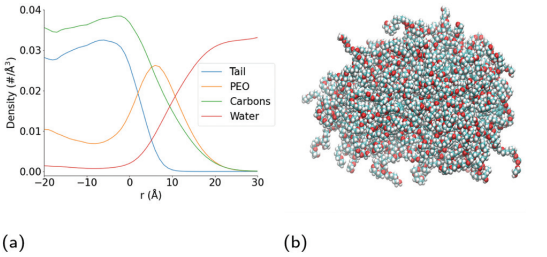


Fig. 2 Structural properties of Triton X-100 micelle. (a) Plot of intrinsic density of the oxygen atoms in the water molecules (red curve), and the carbon atoms in the Triton X-100 surfactant molecules (green curve), as well as the hydrophobic tail (orange curve) and poly(ethylene oxide) chain (blue curve) of the surfactant molecules, as a function of distance r (Å) from the surface of the hydrophobic core of the micelle. (b) Snapshot of equilibrated micelle. The different coloured spheres represent different atomic species (cyan – carbon, red – oxygen, white – hydrogen).

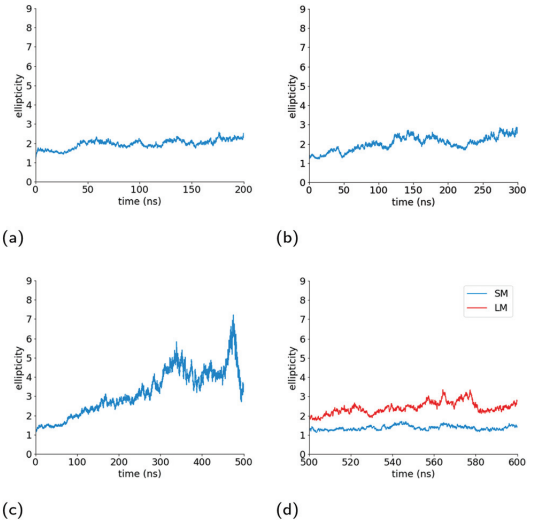


Fig. 3 Ellipticity of the micelles. The ellipticity is plotted as a function of time for the (a) pure Triton X-100 micelle, (b) Triton X-100 micelle loaded with ibuprofen, (c) the parent Triton X-100 micelle loaded with indomethacin and (d) the daughter Triton X-100 micelles (LM – larger micelle, SM – smaller micelle) loaded with indomethacin.

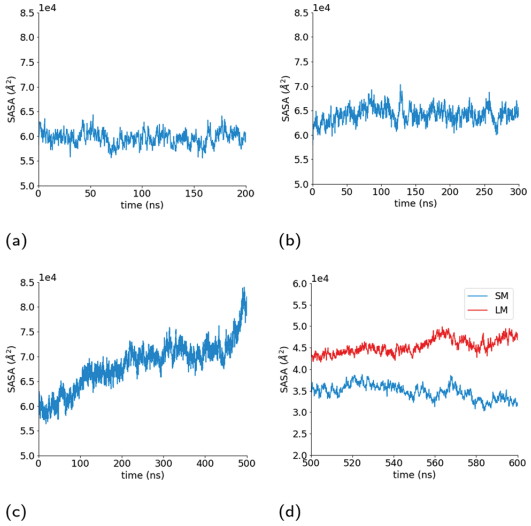


Fig. 4 Solvent accessible surface area (SASA) of micelles. Plots of the SASA as a function of time for the (a) pure Triton X-100 micelle, (b) Triton X-100 micelle loaded with ibuprofen, (c) the parent Triton X-100 micelle loaded with indomethacin and (d) the daughter Triton X-100 micelles (LM – larger micelle, SM – smaller micelle) loaded with indomethacin.

studies.[57–59] The water density begins to decrease slightly at a distance of 25 Å from the micelle's core surface and continues to decrease until it reaches a minimum of 0.02 Å^{-3} at a distance of $r \sim -9$ Å (*e.g.*, 9 Å inside of the hydrophobic core of the micelle). Then in the centre of the micelle ($r \sim -20$ Å), the number density of water is 0.002 Å^{-3}, indicating the existence of a small amount of water inside of the micelle core.

Additionally, we have determined the intrinsic densities of the carbon atoms in the whole micelle (green curve), the poly (ethylene oxide) chain (blue curve) and the hydrophobic tail of the surfactant (orange curve) as shown in Fig. 2a. Some of the PEO chains extend up to a distance of $r \sim 25$ Å, which corresponds to the distance at which the density of water begins to decrease. The thickness of the PEO headgroup, which we define as the distance from the surface of the hydrophobic core of the micelle at which the density of the PEO chains becomes larger than the density of the water, is $r \sim 10.7$ Å. The peak density of the PEO chains is found at a distance of $r \sim 7$ Å from the surface of the hydrophobic core of the micelle. In the hydrophobic core of the micelle, the density of PEO decreases until it reaches a minimum at $r \sim -7.5$ Å and then increases to a density of ~0.011 Å^{-3} at $r = -20$ Å. In the core of the micelle, PEO makes up approximately one-third of the surfactant's density.

Meanwhile the hydrophobic tails of the Triton X-100 molecules, which consist of the benzene ring and the attached short hydrocarbon chain, are found primarily within the core of the micelle ($r < 0$ Å). The hydrophobic tails take a variety of orientations at the interface of the hydrophobic core and the surrounding aqueous environment which results in the small density of these groups found within 7.5 Å of this interface (the end-to-end distance of the hydrophobic tail is ~7.5 Å). Within the core of the micelle, the density of the surfactant tails begins to decrease at $r = -7.5$ Å, which is the distance within the core where we observe the increase in the PEO density. The hydrophobic tails of the Triton X-100 molecules interact *via* a combination of hydrophobic interactions of the benzene rings and the attached methyl groups, as can be seen in Fig. S4.†

Triton X-100 micelles loaded with ibuprofen

Structural properties. As in the TX-100 micelle, we find that the equilibrated micelle loaded with ibuprofen consists of almost all of the TX-100 molecules (~147), although there are a few surfactant molecules that are attempting to join and leave the micelle. In the presence of ibuprofen, the value of the ellipticity of the TX-100 micelle increases from 1.5 to 2.8 and then plateaus at a mean value of 2.51 ± 0.01 (Fig. 3b). Over time, therefore, the semi-spherical micelle becomes more rod-like (triaxial) in shape, with a maximum length of 116.5 ± 0.4 Å. Therefore the TX-100 micelle loaded with ibuprofen has a maximum length that is ~8% larger than the micelle in the absence of the drug.

The surface area of the micelle initially increases as the ibuprofen molecules are solubilised within (Fig. 4b), as can be seen by an increase in the SASA value from an initial value of 6.17 × 10^4 Å^2 SASA to a value of 6.4 ± 0.006 × 10^4 Å^2. As the SASA values plateau after approximately 75 ns and the ellipticity after 150 ns, it appears that the micelle continues to become increasingly rod-like in such a manner that it maintains a constant surface area.

The structure of the micelle when loaded with ibuprofen is similar to that found for the TX-100 micelle. As such, the PEO chains of the surfactant molecules are found on the surface of the hydrophobic core of the micelle, extending into the surrounding aqueous environment, while the benzene ring and corresponding short hydrocarbon chain of the surfactant molecules are generally hidden from exposure to the surrounding aqueous environment.

Solubilisation of ibuprofen

As shown in Fig. 5a, the number of ibuprofen molecules solubilised within the micelle converges to an average of 49 after 50 ns. On average, 39 of these ibuprofen molecules are solubilised within the core of the micelle, and interestingly the number of ibuprofen molecules within the core stabilises at approximately the same point in time.

In order to assess how the hydration of the ibuprofen molecules changes during the solubilisation process, we first measured the radial distribution functions (rdfs) (Fig. S1†) of the polar oxygen atoms within the ibuprofen molecule and the oxygen atom in surrounding water molecules.

From these rdfs, we determined a first neighbour distance between the water molecules and these oxygen atoms of 2.8 Å.

This journal is © The Royal Society of Chemistry 2022

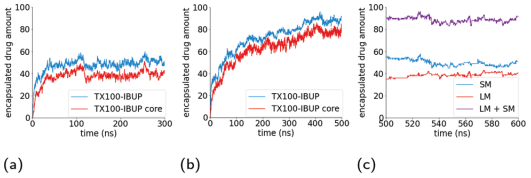


Fig. 5 Solubilisation of drugs. Figures (a) & (b) show the number of drug molecules that have been solubilised within the Triton-X 100 micelle (blue) and within the core (orange) as a function of time for ibuprofen and indomethacin, respectively. Figure (c) shows the number of indomethacin molecules that are solubilised within the smaller daughter micelle (SM), the larger (LM) daughter micelle, and the total number of indomethacin in both after the original micelle divided.

We then counted the number of water molecules within 2.8 Å of the polar oxygen atoms within each ibuprofen during the course of the simulation, and have plotted the average number of water molecules hydrating each of the two oxygen atoms as a function of the intrinsic distance from the interface of the hydrophobic core of the micelle (Fig. 6(a) & (b)), which is defined by the location of the benzene ring of the TX-100 molecules.

As can be seen in Fig. 6b, the number of water molecules around the O1 and O atoms of the ibuprofen molecules remain approximately constant until the drug molecules get within 25 Å of the surface of the hydrophobic core of the micelle (2.18 ± 0.02 water molecules around O1 and O). Then at a distance of 25 Å, which corresponds to the maximum extent of the PEO chains of the TX-100 molecules from the surface of the micelle's core, the number of water molecules around each oxygen decreases slightly. Then at a distance of 20 Å the number of water molecules around each atom increases and reaches a peak at ~7.5 Å which corresponds to the distance which the hydrophobic tails of TX-100 extend from the surface of the core of the micelle into the aqueous environment. Both oxygen atoms of the ibuprofen molecules then become significantly dehydrated as the ibuprofen molecule crosses from the corona of the micelle into the core of the micelle. This dehydration of the oxygens at the interface of the hydrophobic core of the micelle is likely due to the large steric barrier that exists for the drug molecules when they cross into the core of the micelle. When the ibuprofen molecules enter into the core of the micelle, they generally reorientate such that the oxygens in the ibuprofen molecules are at the interface of the core with the aqueous environment and become hydrated to nearly the same level as in the bulk aqueous environment, which is demonstrated by the peak in hydration of the oxygen atoms observed at $\Delta r \sim -7.5$ Å in Fig. 6b. The oxygen atoms on the drug molecules deeper into the core of the micelle become significantly dehydrated once again.

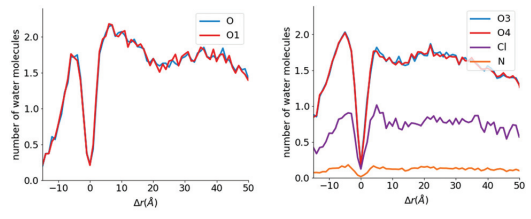


Fig. 6 Hydration of drug molecules during the solubilisation process. Number of water molecules hydrating the (a) O1 and O atoms in the ibuprofen molecules and (b) O3, O4, N and Cl atoms in indomethacin as a function of the distance of each atom from the interface of the core of the micelle. Atom labels are the same as shown in Fig. 1.

In Fig. S7b,† we show the number of water molecules as a function of Δr at various time points during the drug solubilisation process. This figure shows that there is a very slight increase in the number of water molecules deep within the core of the micelle ($\Delta r < -10$ Å) as time passes, which demonstrates that the ibuprofen molecules do not bring a significant amount of water into the micelles with them. In comparison to the TX-100 micelle (Fig. S7a†) formed in the absence of drug, there is very little difference in the number of water molecules within the core micelle of over the course of the two simulations.

Internal structure of ibuprofen-loaded Triton X-100 micelles

To better understand the surfactant–drug and drug–drug interactions, we have measured the amount of contact between the various regions of the molecules. In doing so, we have constructed contact maps, which are generated by calculating the distance between each heavy (non-hydrogen) atom of a TX-100 (or ibuprofen) molecule and a neighbouring ibuprofen molecule. In order to determine a distance at which the molecules are in contact, we first calculated the minimum distance between a TX-100 (or ibuprofen) molecule and an ibuprofen molecule when they interact with each other. From these measurements, we observed that the minimum distance plateaus to ~5 Å when two molecules aggregate with one another. Therefore, if any two heavy (non-hydrogen) atoms are within 5 Å of one another then we count that as a contact between the two molecules.

The regions of the TX-100 surfactant molecules that have the most contact with the ibuprofen molecules are the hydrophobic tails, which correspond to atoms C19–C32 on horizontal axis on Fig. 7a. Meanwhile, the regions of the ibuprofen molecule which are in contact with the surfactant molecules are the two terminal methyl carbon atoms, C11–C12, as highlighted in Fig. 7b. Also we find that the carboxyl group on the ibuprofen molecules makes no contact with the surfactant molecules. Thus the ibuprofen molecules are solubilised within the micelle *via* hydrophobic interactions between themselves and the surfactants while the oxygen atoms remain solvated by the aqueous environment surrounding the core of the micelle.

Within the core of the micelle, the ibuprofen molecules aggregate with one another. In doing so, we find that methyl carbon atoms and the carbon in between them (C10, C11 and

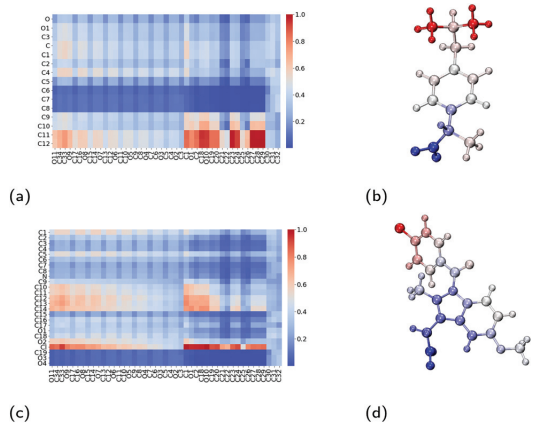


Fig. 7 Interactions between Triton X-100 surfactants and drug molecules. Contact maps which show the amount of contact between an atom on the surfactant molecule (*x*-axis) and an atom on the drug molecule (*y*-axis) for (a) ibuprofen and (c) indomethacin. Diagrams of (b) ibuprofen and (d) indomethacin molecules which have been coloured by their amount of contact with neighbouring Triton X-100 molecules, where the colours are consistent with those used in the contact maps. Atom labels used within the contact maps are those shown in Fig. 1.

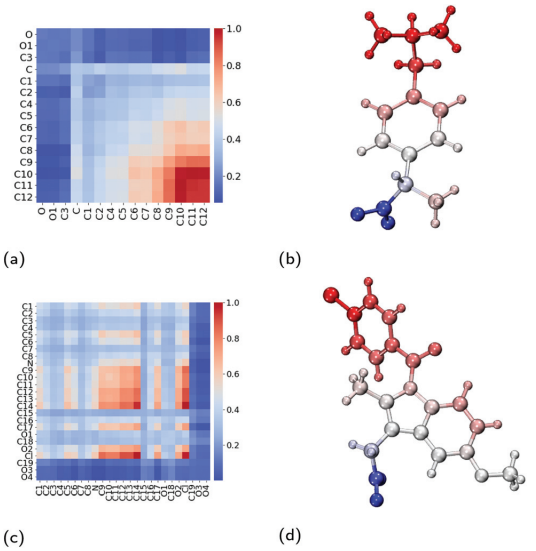


Fig. 8 Interactions between pairs of neighbouring drug molecules. Contact maps which show the amount of contact between two atoms on two neighbouring drug molecules for (a) ibuprofen and (c) indomethacin. Diagrams of (b) ibuprofen and (d) indomethacin molecules which have been coloured by their amount of contact with neighbouring drug molecules, where the colours are consistent with those used in the contact maps. Atom labels used within the contact maps are those shown in Fig. 1.

C12) form contacts with one another, as shown in Fig. 8a and visualised in Fig. 8b. Representative aggregates of ibuprofen molecules formed within the core of the micelle can be seen in Fig. S5.† We have also investigated the contacts which exist within the crystalline form of ibuprofen, which are shown in Fig. S2a.† By comparing these two contact maps (Fig. S3a†), we find that the packing of the drugs within the micelle are significantly different than within their crystalline form. This is largely due to the reorientation of the drugs in the micelle such that the carboxyl group can interact with the surrounding aqueous environment.

Triton X-100 micelles loaded with indomethacin

Structural properties. Like the other systems, we find that the equilibrated micelle loaded with indomethacin consists of almost all of the TX-100 molecules (~146), but there are a few surfactant molecules that are attempting to consistently join and leave the micelle. As with ibuprofen, the solubilisation of the indomethacin molecules causes the micelle to elongate. However, this effect is more significant in the presence of indomethacin (Fig. 3c), where the ellipticity increases to a value of ~7. After forming this elongated structure, the single elongated micelle then splits into two smaller micelles (Fig. 9). The daughter micelles that result from the division of the initial micelle consist of 88 and 62 TX-100 molecules. Both of these daughter micelles have smaller values of ellipticity than the parent micelle before it split. One of the daughter micelles is found to be still elongated and prolate in shape (ellipticity = 2.41 ± 0.01) with a maximum length of 92.7 ± 0.5 Å, while the other is nearly spherical (1.36 ± 0.01), with a maximum length of 78.0 ± 0.2 Å. Both of these values are smaller than the value we found for the TX-100 micelle loaded with ibuprofen.

The SASA of the TX-100 micelle loaded with indomethacin grows until it reaches a maximum value of ~8.0×10^4 Å^2 (Fig. 4c). After the micelle splits into two, the SASA values of the daughter micelles remain fairly constant during the rest of the simulation, as can be seen in Fig. 4d. Interestingly the sum of the SASA values of the two daughter micelles ($3.48 \pm 0.01 \times 10^4$ Å^2 & $4.53 \pm 0.01 \times 10^4$ Å^2) is approximately the same as the SASA value found for parent micelle before it split (~8.3×10^4 Å^2).

Solubilisation of indomethacin

Fig. 5b shows the number of indomethacin molecules that have been solubilised within the micelle and the core of the micelle, respectively, as a function of time. While the amount of ibuprofen loaded into the micelle saturated after approximately 100 ns, the amount of solubilised indomethacin continues to increase until approximately 400 ns. At which point, the number of indomethacin molecules solubilised in the micelle and the core of the micelle reach values of 87 ± 1 and 77 ± 2, respectively. The amount of indomethacin that is solubilised into the core of the micelle is approximately twice the number of ibuprofen molecules solubilised in the core of the micelle.

This journal is © The Royal Society of Chemistry 2022

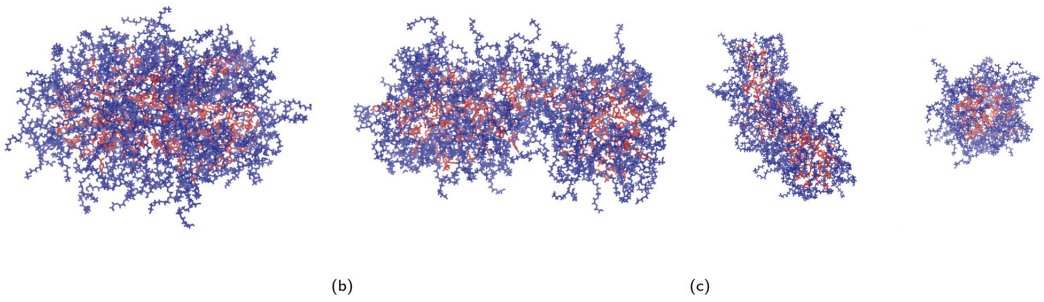


Fig. 9 Snapshots of the indomethacin-loaded Triton X-100 micelle at (a) t = 100 ns, (b) t = 300 ns and (c) t = 600 ns. As shown in these snapshots, the Triton X-100 micelle splits into two daughter micelles of different sizes after 300 ns during the indomethacin solubilisation process. Red and blue show the tails and the headgroups of surfactants respectively.

The number of solubilised indomethacin molecules continues to increase after 400 ns and as a result the values of the ellipticity and the solvent-accessible surface area for the parent micelle continue to increase until the micelle splits. The parent micelle divides into two after it solubilises ~80 indomethacin molecules into the core of the micelle which results in the micelle continuing to elongate until it becomes destabilised and finally divides. After the parent indomethacin-loaded TX-100 micelle divides into the two daughter micelles, the amount of drug in each of the two new micelles is constant and none of the drugs that remained in solution were observed to solubilise into the micelles (Fig. 5c). The smaller micelle which consists of 62 TX-100 molecules, solubilises 40 ± 1 indomethacin molecules, whereas the larger micelle, which consists of 88 surfactant molecules, solubilises 50 ± 3 drug molecules. The ratio of indomethacin to TX-100 in the two daughter micelles (0.65 & 0.57) is similar to that found in the parent indomethacin-loaded micelle before it divided (0.61). This ratio for the daughter micelles (and the parent micelle) of the indomethacin-loaded systems, however, is twice that found for the ibuprofen-loaded micelle (0.34).

As was done for the ibuprofen molecules, we have calculated the hydration of the indomethacin molecules as they approach the surface of the hydrophobic core of the micelle (Fig. 6b). For the indomethacin molecules, we have used the chlorine atom, nitrogen atom and the two oxygen atoms in the carboxyl group in order to characterise the hydration of the drug molecules. At large distances (r > 40 Å) from the hydrophobic core of the micelle, there are 0.80 ± 0.01, 1.86 ± 0.05, 1.85 ± 0.05 and 0.15 ± 0.01 water molecules around the chlorine, O3, O4 and nitrogen atoms, respectively. The hydration of all of the atoms remains constant until a distance of ~15 Å from the surface of the hydrophobic core of the micelle. Then the hydration of the N and Cl atoms increase slightly until the drugs are approximately 5 Å from the surface of the micelle's hydrophobic core, and then are dehydrated as the drugs get close to the interface of the core of the micelle. Then the oxygens, nitrogen and chlorine atoms are significantly dehydrated as they cross into the hydrophobic core of the micelle.

After the drug molecules pass the interface of the core of the micelle, all of the atoms are hydrated again to approximately the same amount as in the bulk aqueous environment. Also the hydration of all four of the atoms we investigated for the indomethacin molecules deeper inside the core of the micelle (Δr < −10 Å) is larger than that found for the ibuprofen molecules in the same region of the micelle.

We then looked at the number of water molecules as a function of Δr at various time points through the solubilisation process (see Fig. S7c†). As time increases, which in the case of the indomethacin-loaded micelle also corresponds to more and more indomethacin in the core of the micelle (see Fig. 5b), we observe an increase in the amount of water within the core of the micelle. At times larger than 400 ns, we observe that the amount of water in the core of the micelle exceeds that found in either the TX-100 micelle (Fig. S7a†) or the ibuprofen-loaded micelles (Fig. S7b†).

Internal structure of indomethacin-loaded Triton X-100 micelles

As was calculated for the ibuprofen-loaded micelle, we again determined the contacts between indomethacin and the surfactant molecules, and between the indomethacin molecules. The indomethacin molecules interact with the TX-100 surfactant molecules primarily *via* its chlorine atom (Cl), which interacts with the benzene ring and the hydrocarbon chain (atoms C19–C32) which form the hydrophobic tail of the surfactants (Fig. 7c & d). Meanwhile, the indomethacin molecules in the core of the micelle bind to one another primarily *via* their chlorobenzene group (atoms C9–C14 & Cl). Representative clusters of indomethacin molecules within the core of the micelle are shown in Fig. S6.† The carboxyl group (atoms C19, O3 & O4) of the indomethacin molecules are not interacting with either the surfactants or other indomethacin molecules. Instead the carboxyl groups are oriented such that they are interacting with the aqueous environment surrounding the micelle.

As a point of comparison, we have determined the contact map between neighbouring indomethacin molecules in its crystalline form, as shown in Fig. S2b.† When comparing the contact maps for the indomethacin in the core of the micelle and that found for the drug in its crystalline form (Fig. S3a†), we find that the chlorobenzene group plays a significant role in the interactions between the drugs in both cases. In the micelle, because the indomethacin molecules are oriented such that their carboxyl group remains hydrated by the surrounding aqueous environment, there is more disorder in the respective orientations of the drug molecules than is found in the crystalline form.

Discussion & conclusions

All-atom molecular dynamics simulations have been used to investigate the internal structure of Triton X-100 micelles with an aggregation number of ~147 molecules. We find that there the PEO chains of the Triton X-100 molecules are present alongside the hydrophobic tails of the surfactant inside of the core of the micelle. While we have not observed such behaviour in our investigations of surfactants with smaller hydrophilic headgroups,[58,60] the intrusion of PEO chains into the hydrophobic core of micelles has been previously observed experimentally Backspace in other PEO containing surfactant molecules.[61–64]

We find that the TX-100 micelles without any drug are non-spherical, which is consistent with the findings of Milano *et al.*[38] for micelles of a similar aggregation number. When investigating the solubilisation of ibuprofen and indomethacin into these micelles, we found that nearly twice as many indomethacin as ibuprofen molecules are solubilised within the micelles. After becoming saturated with drug molecules, we find that the size and shape of the equilibrated ibuprofen-loaded micelles were elongated compared to the TBackspaceX-100 micelles without any drug. In comparison, upon becoming saturated with drug molecules, the indomethacin-loaded micelles become increasingly asymmetric eventually spontaneously dividing into two daughter micelles – a smaller, slightly asymmetric one and a larger, significantly asymmetric one. In addition, we have determined the ellipticity of the hydrophobic core of the two daughter micelles over time, which shows that the core of the larger of the daughter micelles is more dynamic than the smaller micelle.

The SANS experiments that we have conducted in parallel to these simulations show that the TX-100 micelle is non-spherical being model-fitted as a core–shell prolate ellipsoid when it is not loaded with any drug molecules (Fig. 10a & Table 2), which is consistent with what we find *via* our MD simulations. We, also, find that the average maximum diameter of our simulated micelle is 107.8 Å, which is in reasonable agreement with the longest dimension of the micelle as suggested by the fitting of the SANS data (((20.4 Å × 3.8) + 6.7 Å) = 168.8 Å). It is worth commenting that the aggregation numbers obtained from SANS and the MD simulations are not

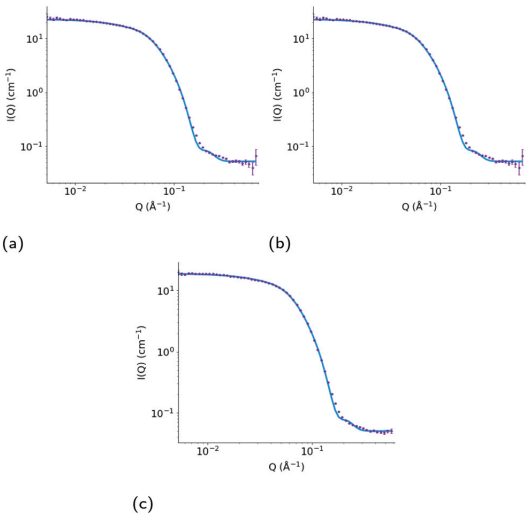


Fig. 10 Measured SANS profile for (a) a 10 wt% dispersion of Triton X-100 in D_2O and for a 7.5 wt% dispersion of Triton X-100 in D_2O with added (b) ibuprofen and (c) indomethacin. Error bars show the standard errors on the measured data, and the model fitted curve in each plot (red) shows the calculated scattering intensity ($I(Q)$, cm^{-1}) as a function of momentum transfer (Q, $Å^{-1}$), assuming the parameters presented in Table 2.

exactly the same because of the limitation of using only one contrast (*i.e.* protiated drug and surfactant dispersed in D_2O) for the SANS data which does not allow us to establish whether any PEO is intruding into the core of the micelle. To establish this, it would be necessary to use additional contrasts using deuterated drug and surfactant (neither of which are readily available) and then to perform a simultaneous constrained model fit across all of the measured data. However, the SANS data shows that the ibuprofen-loaded TX-100 micelles are more asymmetric than the indomethacin-loaded TX-100 micelles, which in turn are more asymmetric than the micelles with no drug. When considering the MD simulations, and in particular the average ellipticity of the two daughter micelles which form after the unstable, indomethacin-saturated micelle divides in two, the results are reassuringly consistent with the SANS results. (It should be noted here that the measured SANS profiles, recorded over several minutes, will show the scattering arising from individual aggregates weighted according to their volume.) The ibuprofen-loaded micelle is more asymmetric than the average of the two daughter, indomethacin-loaded, micelles, which are both more asymmetric than the micelle in the absence of any drug.

As the drug molecules are solubilised in the micelle, we find that the polar atoms are significantly dehydrated as they pass from the hydrated PEO rich corona of the micelle to the micelle's core. Once they have penetrated into the micelle core, the drug molecules reorient such that their carboxyl groups are rehydrated by the water in the aqueous environ-

This journal is © The Royal Society of Chemistry 2022

Table 2 Structural parameters for aqueous dispersions of Triton X-100 micelles in D_2O, determined through model fitting of the corresponding SANS data (with the goodness-of-fit between the observed and calculated scattering quantified by means of reduced chi-squared)

System	Core equatorial radius (Å)	Core axial ratio	Shell thickness (Å)	Overall micelle dimensions (Å)	χR^2
No drug	20.4 ± 0.1	3.8 ± 0.1	6.7 ± 0.1	168 × 84	1.9
Ibuprofen	20.1 ± 0.2	5.3 ± 0.1	8.1 ± 0.1	229 × 56	1.3
Indomethacin	18.6 ± 0.1	5.0 ± 0.1	8.8 ± 0.1	207 × 55	1.7

ment. As the interactions between the indomethacin molecules were more extensive than those between ibuprofen molecules, this resulted in the formation of several larger aggregates within the core of the micelle than is found with ibuprofen. The formation of these larger aggregates of indomethacin within the drug-saturated micelle result in the destabilisation of the initial micelle such that it divides into two smaller micelles. Significantly, we do not observe any such destabilisation of the ibuprofen-loaded micelle which is considered to be due to the fact that the ibuprofen molecules do not interact as extensively with one another in the micelle and therefore do not aggregate as much. A previous experimental investigation of the solubilisation of various drug molecules in sodium lauryl sulfate found more loading of indomethacin than ibuprofen in their resulting micelles,[65] which is the same trend we observe with our simulations. The results in our study provide details of the molecular scale mechanisms which lead to this trend and in our case the disruption of the micelles that form when solubilising the indomethacin. These results show that when designing drug-delivery vehicles the interactions between all of the components present (drugs and surfactant(s)) will play a significant role in the stability of the formulation and the size and shape of the nanoparticles that result.

Author contributions

HI – data curation, formal analysis, investigation, methodology, software, validation, visualisation, writing – original draft. NHR – supervision, writing–review & editing. DJB – conceptualisation, supervision, data curation, formal analysis, methodology, resources, writing–review & editing. MJL – conceptualisation, supervision, funding acquisition, resources, writing–review & editing. CDL – conceptualisation, supervision, funding acquisition, resources, project administration, writing–review & editing.

Conflicts of interest

There are no conflicts to declare.

Acknowledgements

Through C. D. L.'s membership within the UK HPC Materials Chemistry Consortium, which is funded by the Office of Science and Technology through the EPSRC High End Computing Programme (grant no. EP/L000202, EP/R029431), the use of ARCHER, the UK National Supercomputing Service (**https://www.archer.ac.uk**) and the UK Materials and Molecular Modelling Hub (MMM Hub), which is partially funded by the EPSRC (EP/P020194/1, EP/T022213), was used for the molecular dynamics simulations presented in this work. A special thanks to "Tekeyan Trust London" whose funding has made H. I.'s research at KCL possible. N.H.R. is supported by a King's Prize Fellowship funded by a Wellcome Trust (**https://wellcome.ac.uk/**) Institutional Strategic Support Fund grant to King's College London (204823/Z/16/Z). Experiments at the ISIS Neutron and Muon Source were supported by beamtime allocation from STFC, and the SANS data are available at **https://doi.org/10.5286/ISIS.E.RB1710299**. This work benefited from the use of the SasView application, originally developed under National Science Foundation award DMR-0520547. SasView also contains acode developed with funding from the European Union's Horizon 2020 research and innovation program under the SINE2020 project, grant no. 654000.

Notes and references

1 V. Patravale, P. Dandekar and R. Jain, *Nanoparticulate Drug Delivery*, Woodhead Publishing, 2012, pp. 29–85.
2 R. H. Muller and C. M. Keck, *J. Biotechnol.*, 2004, **113**, 151–170.
3 A. Puri, K. Loomis, B. Smith, J. H. Lee, A. Yavlovich, E. Heldman and R. Blumenthal, *Crit. Rev. Ther. Drug Carrier Syst.*, 2009, **26**, 523–580.
4 K. Möller and T. Bein, *Chem. Mater.*, 2019, **31**, 4364–4378.
5 V. Karthika, P. Kaleeswarran, K. Gopinath, A. Arumugam, M. Govindarajan, N. S. Alharbi, J. M. Khaled, M. N. Al-anbr and G. Benelli, *Mater. Sci. Eng., C*, 2018, **90**, 589–601.
6 M. Medina-Sánchez, H. Xu and O. G. Schmidt, *Ther. Delivery*, 2018, **9**, 303–316.
7 M. J. Haney, N. L. Klyachko, Y. Zhao, R. Gupta, E. G. Plotnikova, Z. He, T. Patel, A. Piroyan, M. Sokolsky, A. V. Kabanov and E. V. Batrakova, *J. Chem. Rev.*, 2015, **207**, 18–30.
8 K. Cho, X. Wang, S. Nie, Z. Chen and D. Shin, *Clin. Cancer Res.*, 2008, **14**, 1310–1316.
9 F. U. Din, W. Aman, I. Ullah, O. S. Qureshi, O. Mustapha, S. Shafique and A. Zeb, *Int. J. Nanomed.*, 2017, **12**, 7291–7309.
10 L.-L. Li, H.-W. An, B. Peng, R. Zheng and H. Wang, *Mater. Horiz.*, 2019, **6**, 1794–1811.

11 G. S. Kwon and T. Okano, *Pharm. Res.*, 1999, **16**, 597–600.
12 C. J. Drummond and C. Fong, *Curr. Opin. Colloid Interface Sci.*, 1999, **4**, 449–456.
13 Y. Jin, L. Tong, P. Ai, M. Li and X. Hou, *Int. J. Pharm.*, 2006, **309**, 199–207.
14 S. Zhang, *Nat. Biotechnol.*, 2003, **21**, 1171–1178.
15 I. Marzuoli, C. H. B. Cruz, C. D. Lorenz and F. Fraternali, *Nanoscale*, 2021, **13**, 10342–10355.
16 I. E. Kepiro, I. Marzuoli, K. Hammond, X. Ba, H. Lewis, M. Shaw, S. B. Gunnoo, E. D. Santis, U. Lapriska, S. Pagliara, M. A. Holmes, C. D. Lorenz, B. W. Hoogenboom, F. Fraternali and M. G. Ryadnov, *ACS Nano*, 2020, **14**, 1609–1622.
17 X. Gao and H. Matsui, *Adv. Mater.*, 2005, **17**, 2037–2050.
18 V. Linko, A. Ora and M. A. Kostiainen, *Trends Biotechnol.*, 2015, **33**, 586–594.
19 I. F. Uchegbu and S. P. Vyas, *Int. J. Pharm.*, 1998, **172**, 33–70.
20 M. J. Lawrence, *Eur. J. Drug Metab. Pharmacokinet.*, 1994, **19**, 257–269.
21 A. Makhlouf, I. Hajdu and I. Badea, *Organic Materials as Smart Nanocarriers for Drug Delivery*, William Andrew Publishing, 2018, pp. 561–600.
22 A. Rajagopal, A. C. Pant, S. M. Simon and Y. Chen, *Cancer Res.*, 2002, **62**, 391–396.
23 D. Hipfner, S. Gauldie, R. Deeley and S. Cole, *Cancer Res.*, 1994, **54**, 5788–5792.
24 A. Solomonov, Y. Marfin, E. Rumyantsev, E. Ragozin, T. Shekhter, G. Gellerman, A. Tesler, F. Muench, A. Kumagai and A. Miyawaki, *Mater. Sci. Eng., C*, 2019, **99**, 794–804.
25 A. Mukhija and N. Kishore, *J. Mol. Liq.*, 2018, **265**, 1–15.
26 A. Das and R. K. Mitra, *Colloid Polym. Sci.*, 2013, **292**, 635–644.
27 A. Kalatizaki, M. Poulopoulou, A. Xeankis and V. Papadimitriou, *Colloids Surf., A*, 2014, **442**, 80–87.
28 E. A. Dennis, *Arch. Biochem. Biophys.*, 1974, **165**, 764–773.
29 H. H. Paradies, *J. Phys. Chem.*, 1980, **84**, 599–607.
30 R. J. Robson and E. A. Dennis, *J. Phys. Chem.*, 1977, **81**, 1075–1078.
31 L. M. Kushner and W. D. Hubbard, *J. Phys. Chem.*, 1954, **58**, 1163–1167.
32 K. Streletzky and G. D. J. Phillies, *Langmuir*, 1995, **11**, 42–47.
33 A. S. Sadaghiani and A. Khan, *Langmuir*, 1991, **7**, 898–904.
34 A. Mandal, S. Ray, A. Biswas and S. Moulik, *J. Phys. Chem.*, 1980, **84**, 856–859.
35 F. Podo, A. Ray and G. Nemethy, *J. Am. Chem. Soc.*, 1973, **85**, 6164–6171.
36 D. Yordanova, I. Smirnova and S. Jakobtorweihen, *J. Chem. Theory Comput.*, 2015, **11**, 2329–2340.
37 A. De Nicola, T. Kawakatsu, C. Rosano, M. Celino, M. Rocco and G. Milano, *J. Chem. Theory Comput.*, 2015, **11**, 4959–4971.
38 W. Murakami, A. D. Nicola, Y. Oya, J.-I. Takimoto, M. Celino, T. Kawakatsu and G. Milano, *ACS Appl. Nano Mater.*, 2021, **4**, 4552–4561.
39 T. G. Kantor, *Ann. Intern. Med.*, 1979, **91**, 877–882.
40 N. M. Davies, *Clin. Pharmacokinet.*, 1998, **34**, 101–154.
41 G. Alván, M. Orme, L. Bertilsson, R. Ekstrand and L. Palmér, *Clin. Pharmacol. Ther.*, 1975, **18**, 364–373.
42 *National Center for Biotechnology Information (2021). PubChem Compound Summary for CID 3715, Indomethacin. Retrieved April 28, 2021 from* **https://pubchem.ncbi.nlm.nih.gov/compound/Indomethacin**.
43 U. Patel, N. Dharaiya and P. Bahadur, *J. Mol. Liq.*, 2016, **216**, 156–163.
44 N. Dharaiya and P. Bahadur, *Colloids Surf., A*, 2012, **410**, 81–90.
45 M. J. Abraham, T. Murtola, R. Schulz, S. Páll, J. C. Smith, B. Hess and E. Lindahl, *SoftwareX*, 2015, **1–2**, 19–25.
46 E. Lindahl, *Solving Software Challenges for Exascale*, 2015, pp. 3–27.
47 S. Pronk, S. Páll, R. Schulz, P. Larsson, P. Bjelkmar, R. Apostolov, M. R. Shirts, J. C. Smith, P. M. Kasson, D. van der Spoel, B. Hess and E. Lindahl, *Bioinformatics*, 2013, **29**, 845–854.
48 J. Huang, S. Rauscher, G. Nawrocki, T. Ran, M. Feig, B. L. de Groot, H. Grubmüller and A. D. MacKerell, *Nat. Methods*, 2017, **14**, 71–73.
49 K. Vanommeslaeghe, E. Hatcher, C. Acharya, S. Kundu, S. Zhong, J. Shim, E. Darian, O. Guvench, P. Lopes, I. Vorobyov and A. D. Mackerell, *J. Comput. Chem.*, 2010, **31**, 671–690.
50 L. Martínez, R. Andrade, E. G. Birgin and J. M. Martínez, *J. Comput. Chem.*, 2009, **30**, 2157–2164.
51 B. Hess, H. Bekker, H. J. C. Berendsen and J. G. E. M. Fraaije, *J. Comput. Chem.*, 1997, **18**, 1463–1472.
52 R. J. Gowers, M. Linke, J. Barnoud, T. J. E. Reddy, M. N. Melo, S. L. Seyler, J. Domański, D. L. Dotson, S. Buchoux, I. M. Kenney and O. Beckstein, Proceedings of the 15th Python in Science Conference, 2016, pp. 98–105.
53 N. Michaud-Agrawal, E. J. Denning, T. B. Woolf and O. Beckstein, *J. Comput. Chem.*, 2011, **32**, 2319–2327.
54 B. Lee and F. M. Richards, *J. Mol. Biol.*, 1971, **55**, 379–400.
55 S. Mitternacht, *F1000Research*, 2016, **5**, 189.
56 M. Doucet, J. H. Cho, G. Aline, J. Bakker, W. Bouwman, P. Butler, K. Campbell, M. Gonzales, R. Heenan, A. Jackson, P. Juhas, S. King, P. Kienzle, J. Krzywon, A. Markvardsen, T. Nielsen, L. O'Driscoll, W. Potrzebowski, R. F. Leal, T. Richter, P. Rozycko, T. Snow and A. Washington, *SasView version 4.2*, 2018.
57 D. T. Allen and C. D. Lorenz, *J. Mol. Model.*, 2017, **23**, 1–11.
58 D. T. Allen, Y. Saaka, M. J. Lawrence and C. D. Lorenz, *J. Phys. Chem. B*, 2014, **118**, 13192–13201.
59 R. M. Ziolek, P. Smith, D. L. Pink, C. A. Dreiss and C. D. Lorenz, *Macromolecules*, 2021, **54**, 3755–3768.
60 C. D. Lorenz, C.-M. Hsieh, C. A. Dreiss and M. J. Lawrence, *Langmuir*, 2011, **27**, 546–553.
61 P. H. Elworthy and M. S. Patel, *J. Pharm. Pharmacol.*, 1982, **34**, 543–546.

This journal is © The Royal Society of Chemistry 2022

62 T. Arnarson and P. H. Elworthy, *J. Pharm. Pharmacol.*, 1982, **34**, 87–89.
63 P. H. Elworthy and M. S. Patel, *J. Pharm. Pharmacol.*, 1984, **36**, 116–117.
64 P. H. Elworthy and M. S. Patel, *J. Pharm. Pharmacol.*, 1984, **36**, 565–568.
65 M. N. Alizadeh, A. Shayanfar and A. Jouyban, *J. Mol. Liq.*, 2018, **268**, 410–414.

This journal is © The Royal Society of Chemistry 2022

Chapter 4

NSAID solubilisation promotes morphological transitions in Triton X-114 surfactant micelles

The following chapter investigates micelles formed by Triton X-114 non-ionic surfactants and their morphological transition induced by drugs solubilizing inside of the micelle. The encapsulation of two poorly-soluble, non-steroidal anti-inflammatory drugs (NSAIDs), ibuprofen and indomethacin, was investigated. The results show a larger number of indomethacin molecules being encapsulated inside of the micelle, than ibuprofen molecules. The encapsulation process results in elongation of the initially semi-spherical micelles, whereas the pure micelle remains semi-spherical. Furthermore, indomethacin solubilization induced a disruption in the initial micelle, resulting it to be split in two. This work extends the previous chapter by examining how a micelle formed by a shorter Triton X-114 (8 ethylene glycol units) surfactant will differ in its solubilizing and structural properties from those formed by Triton X-100 (10 ethylene glycol units). The results have shown an increased number of ibuprofen molecules solubulizing in Triton X-114 micelles in comparison with the micelles formed by Triton X-100, which indicates that due to the shorter hydrophilic sections in Triton X-114, the diffusion of poorly-soluble drugs is enhanced.

In the results section of the paper, the contact maps and structure diagrams of the molecules are presented. The color-coding in these diagrams is the same as used in the the contact maps: atoms with the largest amount of contact are depicted in red, while atoms engaged in the least number of contacts are represented in blue.

The article included in this chapter has been published in *Journal of Molecular Liquids* in 2022 with Hrachya Ishkhanyan as its first author. The molecular dynamics simulations were performed by Hrachya Ishkhanyan. The trajectories were analyzed by Hrachya Ishkhanyan except for the calculation of the intrinsic densities. The scripts and tools for the analysis, unless stated otherwise, were developed by Hrachya Ishkhanyan except for the code that calculates the intrinsic densities. The manuscript was written by Hrachya Ishkhanyan and edited by Robert M. Ziolek, David J. Barlow, M. Jayne Lawrence, Armen Poghosyan and Christian D. Lorenz. Figures, diagrams and graphs were produced by Hrachya Ishkhanyan and Robert M. Ziolek. The supplementary information to this article is shown in Appendix B.

Journal of Molecular Liquids 356 (2022) 119050

Contents lists available at ScienceDirect

Journal of Molecular Liquids

journal homepage: www.elsevier.com/locate/molliq

NSAID solubilisation promotes morphological transitions in Triton X-114 surfactant micelles

Hrachya Ishkhanyan [a], Robert M. Ziolek [a], David J. Barlow [b], M. Jayne Lawrence [b], Armen H. Poghosyan [c,*], Christian D. Lorenz [a,*]

[a] Biological Physics and Soft Matter Group, Department of Physics, King's College London, London WC2R 2LS, United Kingdom
[b] Division of Pharmacy and Optometry, School of Health Sciences, Faculty of Biology, Medicine and Health, University of Manchester, Stopford Building, Oxford Road, Manchester M13 9PG, United Kingdom
[c] International Scientific-Educational Center of National Academy of Sciences, M. Baghramyan Ave. 24d, 0019 Yerevan, Armenia

ARTICLE INFO

Article history:
Received 17 December 2021
Revised 26 March 2022
Accepted 28 March 2022
Available online 30 March 2022

Keywords:
Triton X-114
Ibuprofen
Indomethacin
Solubilisation
Micelles
NSAIDs

ABSTRACT

The structural properties of micelles formed by the non-ionic surfactant, Triton X-114 (TX-114), were investigated using all-atom molecular dynamics (MD) simulations. Additionally, we investigated the effect of the solubilisation of the sodium salts of two nonsteroidal anti-inflammatory drugs, ibuprofen and indomethacin, upon the structural properties of TX-114 micelles. The micelle in absence of the drugs has an aspherical shape. We find that as the micelle continues to solubilise drug molecules, its shape becomes even more elongated. The solubilised drug molecules are observed to take orientations within the core of the micelle that allows their carboxyl groups to remain hydrated by the surrounding interfacial solvent. Also we find that the increased aggregation of indomethacin via $\pi - \pi$ stacking of its chlorobenzene group leads to destabilisation of the micelle. In the ibuprofen-loaded micelle, where the solubilised drug molecules do not aggregate to the same degree, we find that the drug-loaded micelle remains stable. These results provide a mechanistic description of how the solubilisation of NSAIDs drives morphological changes in TX-114 micelles. Additionally, we show how the physico-chemical properties of both surfactants and drug molecules can play a significant role in the stabilisation of drug delivery vehicles.

© 2022 The Author(s). Published by Elsevier B.V. This is an open access article under the CC BY license (http://creativecommons.org/licenses/by/4.0/).

1. Introduction

Drug delivery systems are used to control the precise delivery of therapeutics to a biological target. With advances in nanotechnology, drug carriers are continually improving, providing better solubilisation properties and more precise control over where drug molecules are delivered [1,2]. A wide range of materials are used to manufacture drug delivery vehicles (DDV), including polymers, lipoproteins, nanoparticles, and surfactants [3–13].

One major family of DDVs are self-assembled nanostructures. Self-assembly enables a simple and cost-efficient method for creating nanoparticles. During the self-assembly process, the materials organize into ordered nanostructures through non-covalent interactions. In the work reported here, we focus on surfactant-based DDVs. Surfactants (a portmanteau of 'surface active agents') are amphiphilic molecules, which have two covalently linked moieties - a hydrophilic headgroup and a hydrophobic tail. As a result, they self-assemble in aqueous solutions into structures such as micelles or liposomes [14–16]. Because of these unique properties, surfactants are commonly used as detergents, emulsifiers, antimicrobial agents, protein denaturation agents and DDVs [17–19]. Non-ionic surfactants have become attractive materials for the latter, because of their biodegradability and their lower toxicity relative to the charged surfactants [20]. With their high drug-loading capacity, cost-efficiency and simplicity of production, surfactant-based micelles are attractive candidates as DDVs [14].

In this manuscript, we are investigating the non-ionic surfactant Triton X-114 (TX-114). TX-114 surfactants consist of a hydrophilic polyethylene oxide (PEO) headgroup, comprising eight EO units, and a 4-(1,1,3,3-tetramethylbutyl)-phenyl hydrophobic tail. TX-114 is well-known to self-assemble into micelles in aqueous solution [21] and is commonly used in cell lysis and protein extraction [22]. However, only a small number of previous studies have investigated this surfactant and its self-assembly using computational methods. Yordanova et al. reported optimized CHARMM parameters for TX-114, which we have used in this work [23]. Fur-

* Corresponding authors.
E-mail addresses: sicnas@sci.am (A.H. Poghosyan), chris.lorenz@kcl.ac.uk (C.D. Lorenz).

https://doi.org/10.1016/j.molliq.2022.119050
0167-7322/© 2022 The Author(s). Published by Elsevier B.V.
This is an open access article under the CC BY license (http://creativecommons.org/licenses/by/4.0/).

thermore, Ritter *et al.* described the prediction of the micelle water partition coefficients for different micelles including those made from TX-114, [24] using the COSMOmic software package [25].

Nonsteroidal anti-inflammatory drugs (NSAIDs) are therapeutic agents used primarily for the treatment of pain and inflammation [26–29]. The poor solubility of NSAIDs complicates the development of oral or injectable pharmaceutical formulations used to deliver these drugs and restricts their application in oral and parenteral applications [30–34]. Therefore, the design of formulations for NSAIDs is challenging, requiring investigations into the solubility of this class of drugs in the presence of surfactants [35–42]. Understanding the atomistic interactions that underlie the solubilisation of NSAIDs within surfactant micelles, as revealed in this work, provides important information that is necessary to further improve these formulations.

In this study, we use all-atom molecular dynamics (MD) simulations to investigate the solubilisation of ibuprofen ($C_{13}H_{18}O_2$) and indomethacin ($C_{19}H_{16}ClNO_4$) sodium ions (Fig. 1), and their effect on the structural properties of TX-114 micelles. Both of these drugs are deprotonated at neutral pH. Nevertheless, despite this ionisation, these drugs are poorly soluble in aqueous solution, and in order to increase their bioavailability, DDVs are used. Our simulations show that significantly more indomethacin than ibuprofen is solubilised in the Triton X-114 micelles. This increased solubilisation of indomethacin is found to be driven by strong interactions between different indomethacin molecules in the core of the micelle, which leads to large aggregates of drug molecules within the micelle. As a result, we find that the solubilisation process of the indomethacin ions results in the Triton X-114 micelle finally splitting into two daughter micelles, which are unequal in size.

2. Methods

2.1. Molecular dynamics simulations

We have studied three systems: a TX-114 micelle in aqueous solution, and a TX-114 micelle interacting with each of the two NSAIDs, ibuprofen and indomethacin (Fig. 1a & b, respectively). The CHARMM36 General Force Field (CGenFF) was used to model ibuprofen and indomethacin [43]. The TX-114 molecules were modelled by the CHARMM parameters reported by Yordanova et al. [23]. Water was modelled with the CHARMM-modified TIP3P potential [44]. All simulations were performed using the GROMACS 2020 simulation engine[45].

The TX-114 micelle was pre-assembled into a spherical structure using Packmol [46]. The micelle-only simulation was conducted with a box of initial dimensions $120 \times 120 \times 120$ Å^3. In the case of the two NSAID-containing systems, 100 ibuprofen or indomethacin molecules were randomly placed in at a minimum distance of 38 Å from the surface of the pre-assembled micelle within a $130 \times 130 \times 130$ Å^3 simulation box. All systems were solvated with water molecules. Table 1 shows the number of water, surfactant and drug molecules in each of the simulated systems. Since both of the drugs are singly deprotonated in neutral pH, 100 sodium ions were added to neutralise the total charge of each drug-containing system.

The steepest descent algorithm was used to minimise the energy of each system (5×10^3 steps). Then each system was brought to thermal equilibrium in the NVT ensemble for 75 ps, reaching a target temperature of 303.15 K using the Nosé-Hoover thermostat [47,48]. Subsequently, the density was equilibrated to 1 bar at 303.15 K within 300 ps using the Nosé-Hoover thermostat and Parrinello-Rahman barostat [49]. A final box size of $118.8 \times 118.8 \times 118.8$ Å^3 was reached for the pure micelle system and $133.8 \times 133.8 \times 133.8$ Å^3 for systems containing the NSAIDs. All equilibration simulations were performed without constraints, using a 1 fs timestep. Production simulations were performed in the NPT ensemble at 303.15 K and 1 bar, again using the Nosé-Hoover thermostat and Parrinello-Rahman barostat. A 200 ns simulation of the TX-114 micelle in solution was sufficient to observe structural equilibration of the micelle, as judged by the rapid equilibration of its radius of gyration and ellipticity. Each simulation for the drug-containing micelles was run for 1 μs, to allow for drug molecules to diffuse towards, and interact with, the micelle. The cut-off distances for electrostatic and Lennard-Jones potentials were set to 12 Å. Long-range electrostatic interactions were calculated using the Particle-Mesh Ewald method. In each of the production simulations, hydrogen-containing bonds were constrained using the LINCS algorithm [50] in order to use a timestep of 2 fs.

2.2. Analysis

All simulation analysis was performed using in-house Python codes, which make wide use of the MDAnalysis package [51,52]. Simulation visualisations were produced using VMD [53].

Structure of the micelles. The radius of gyration (r_g) of a micelle consisting of N atoms, each having mass m_i and Cartesian coordinates $\mathbf{r}_i$, is defined with reference to the micelle's center of mass ($\mathbf{r}_{COM}$) as:

$$r_g = \sqrt{\frac{1}{M}\sum_{i=1}^{N} m_i |\mathbf{r}_i - \mathbf{r}_{COM}|^2} \quad (1)$$

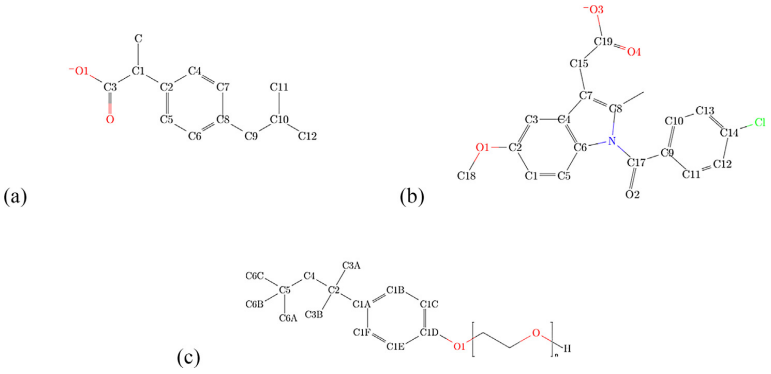


Fig. 1. Chemical structures of molecules studied by MD simulations. (a) ibuprofen, (b) indomethacin, and (c) Triton X-114 (for which n = 8).

Table 1
Composition of the different simulation systems. The number of different molecular species included in each simulation and the concentration of TX-114 in each simulation.

System	NSAID	Surfactant	Water	TX-114 Conc. [mol dm^{-3}]
TX-114	0	150	51958	0.14
TX-114 - IBUP	100	150	74779	0.11
TX-114 - INDO	100	150	74437	0.11

The shape of the micelle was characterized by its ellipticity (ϵ), which is defined as:

$$\epsilon = \frac{I_{max}}{I_{min}}, \tag{2}$$

where I_{max} and I_{min} are the largest and smallest moments of inertia of the micelle. We note that in the case of a perfect sphere, $\epsilon = 1$ and ϵ increases as the micelle becomes more non-spherical. The shape of the micelle can be further characterized by comparing the moments of inertia with respect to principal axes of the micelle. The micelle is oblate, if two values are close to each other and larger than the third, prolate, if smaller than the third, spherical if all values are approximately the same and triaxial, if all values differ. The solvent-accessible surface area (SASA) of the micelles was calculated using the Shrake-Rupley algorithm with a probe radius of 1.4 Å[54,55].

The intrinsic core–shell interface (ICSI) algorithm was used to investigate the internal and interfacial structure of the TX-114 micelle in solution, as previously applied to polymer micelles made from Tetronic 904 and Pluronic L64 [56,57]. The intrinsic density of each micelle component (in this case, the hydrophobic TX-114 tails, its hydrophilic PEO chains, and water) is expressed as follows, using a spherical polar coordinate (r, θ, ϕ) basis:

$$\tilde{\rho}(r) \equiv \left\langle \sum_i \frac{\delta[r - (r_i - \xi(\theta, \phi))]}{\bar{S}_i(r)} \right\rangle \tag{3}$$

Here r_i is the r-position of atom i and $\xi(\theta, \phi)$ is the r-position of the intrinsic core–shell interface. Since the normalisation factor, the

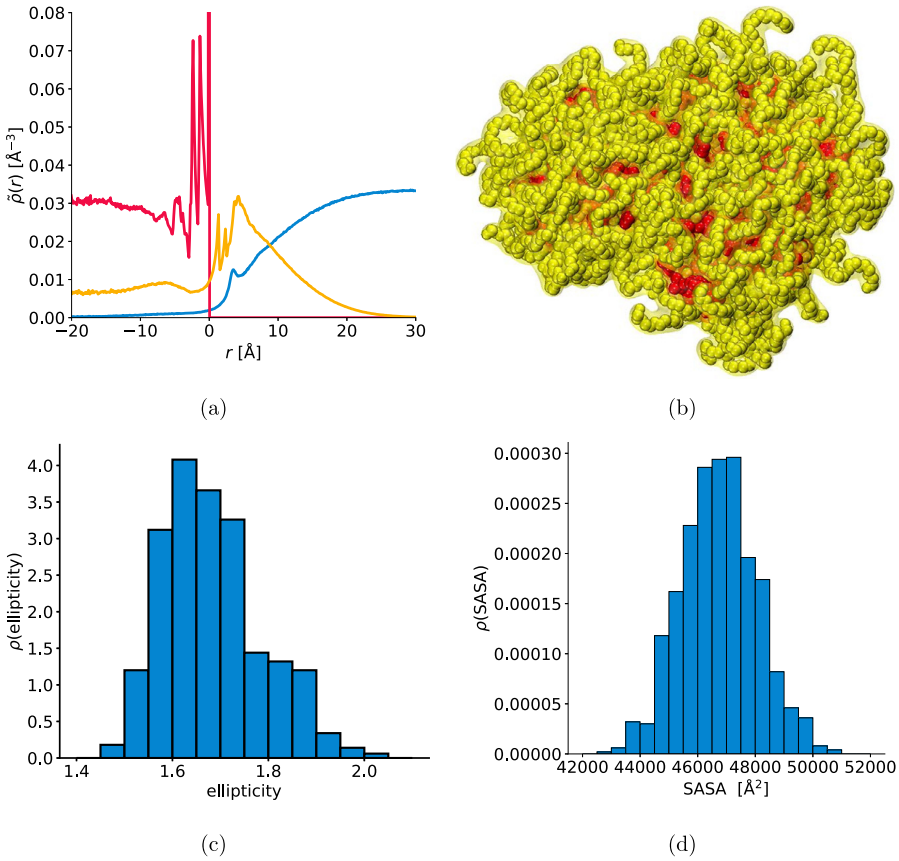


Fig. 2. Structure of the TX-114 micelle. (a) Intrinsic density of the TX-114 micelle obtained using the ICSI method: hydrophobic tails (red), hydrophilic PEO chains (orange) and water (blue). (b) Snapshot of TX-114 micelle. Probability distributions of the different values of (c) ellipticity and (d) the solvent accessible surface area (SASA).

average volume of each shell, $\overline{S}_i(r)$, cannot be found analytically, we use Monte Carlo integration to find this quantity as

$$\overline{S}_i(r) = \frac{n_i \overline{V}_{box}}{N}, \quad (4)$$

Note that n_i is the number of random points identified in the shell in which atom i is found and $\overline{V}_{box}$ is the average volume of the simulation box (both averaged over all of the different frames analysed). N is the total number of random points used in the normalisation process. Given the highly non-spherical and disordered nature of the TX-114 micelles in the presence of the drug molecules, it was not appropriate to use this method, with its spherical polar coordinate basis, to investigate these systems in the same way.

Drug solubilisation within the micelles. To evaluate drug solubilisation, the distances between the centers of masses (COM) of drug molecules and the TX-114 surfactants were calculated. If a drug is found within 5 Å of the nearest surfactant, it is considered to be solubilised (Fig. S15). The cut-off distance of 5 Å was selected by measuring the minimum distance between reference atoms within ibuprofen and indomethacin molecules and in Triton X-114 surfactant molecules.

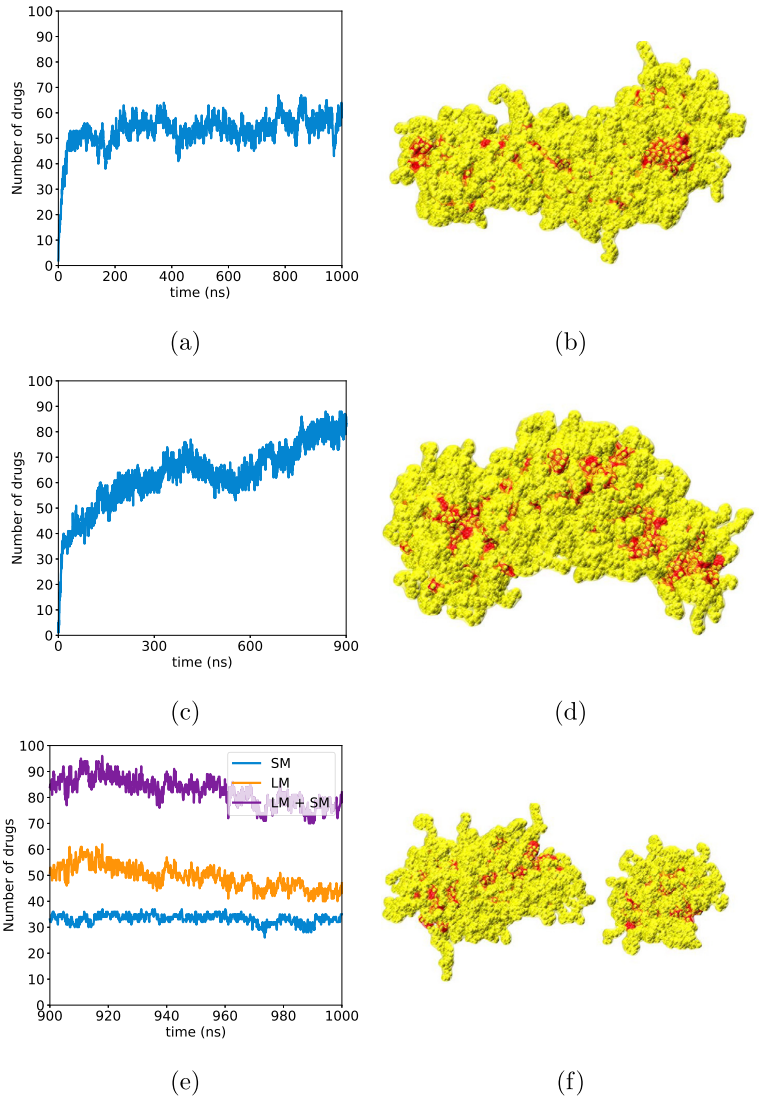


Fig. 3. Solubilisation of drugs within TX-114 micelles. The number of drug molecules solubilised within the micelle as a function of time for the (a) ibuprofen and (c) indomethacin systems. (e) The number of indomethacin molecules solubilised within the smaller daughter micelle (SM), the larger (LM) daughter micelle, and the total number of indomethacin in both micelles after the original micelle splits. Snapshots of the systems: (b) TX-114-IBUP, (d) TX-114-INDO before splitting and (f) TX-114-INDO after splitting.

The hydration of the drug molecules was characterized by calculating the number of water molecules as a function of their radial distance from the nearest surfactant $\Delta r = r_d - r_s$, where r_d and r_s are the radial distances of the drug molecule and the hydrophobic tails of its nearest surfactant, respectively, from the micelle's center of mass. A value of $\Delta r > 0$ indicates that the drug molecules are outside of the hydrophobic core of the micelle, while $\Delta r < 0$ implies the drug is buried within the micellar core. This analysis is useful since the disordered structures of the micelles in the presence of NSAIDs are otherwise challenging to analyse.

The radial distribution function (RDF) is defined as

$$g(r)_{i,j} = \frac{\rho(r)_{i,j}}{\rho_j} \tag{5}$$

where $g(r)_{i,j}$ is the probability of finding a particle of type j at a distance r from a reference particle of type i, $\rho(r)_{i,j}$ is the density of type j particles at a distance r from a type i particle and ρ_j is the average density of type j particles. The coordination number of water around selected drug atoms of interest was calculated using the position of the first minimum in their respective RDFs (Fig. S1). Values of 3.5 Å and 7.2 Å were used for the chlorine and nitrogen atoms in indomethacin, respectively. A value of 2.8 Å was used for the carboxylate oxygen atoms found in both drugs.

Contact maps were generated to characterise the drug-drug and drug-surfactant interactions in detail. The distances between all of the non-hydrogen atoms of the corresponding molecules were calculated, with any distance less than 5 Å deemed to indicate atoms in contact. These calculations were averaged over the final portion of the trajectories, where the number of solubilised drug molecules had reached stationarity. The contacts maps are normalised independently, with a value of 1 identifying the most frequent interaction in each case. The distribution of drug cluster sizes at different times during the simulation was calculated using a graph-theoretical approach described previously [56]. Here, we used a cutoff distance of 7.5 Å between N atoms (for indomethacin) and C8 atoms (for ibuprofen).

3. Results

3.1. Pure Triton X-114 micelle

The Triton X-114 micelle is stable in an aqueous environment, as demonstrated by the distribution of the number of surfactant molecules found in the micelle shown in Fig. S2, which shows at most a few molecules are found isolated in solution at any one time. The distribution of PEO headgroups and the hydrophobic tails of the TX-114 molecules within the micelle are shown in the plot of the intrinsic density (Fig. 2a). We note that the core of the micelle

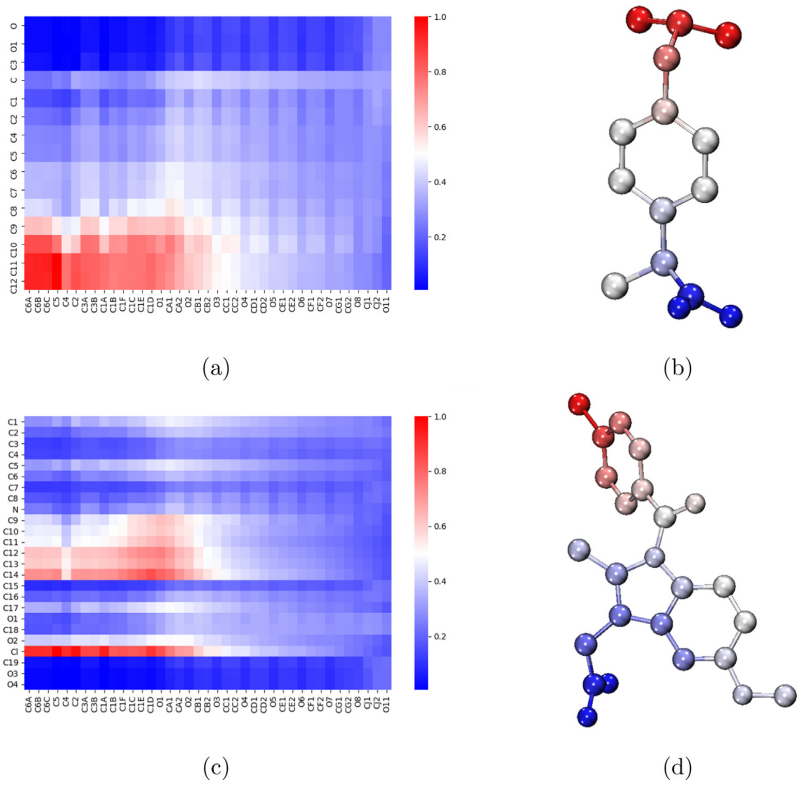


Fig. 4. Interactions between TX-114 surfactants and drug molecules. Contact maps which show the amount of contact between an atom on the surfactant molecule (x-axis) and an atom on the drug molecule (y-axis) for (a) ibuprofen and (c) indomethacin. Diagrams of (b) ibuprofen and (d) indomethacin molecules which have been coloured by their amount of contact with neighbouring Triton X-114 molecules, where the colours are consistent with those used in the contact maps. Atom labels used within the contact maps are those shown in Fig. 1.

consists predominantly of the hydrophobic tails of TX-114, as expected for the micelles formed by a typical amphiphile. The peaks in the hydrophobe intrinsic density for $-10\,\text{Å} < r < 0\,\text{Å}$ are indicative of the reordering of the tails at the interface with water. We also observe a significant population of PEO chains within the core of the micelle, which has been proposed to occur previously by Elworthy et al [58]. This is different to the analogous observation for micelles made of amphiphilic block copolymers with larger hydrophobic blocks: a more effective partitioning is observed in the case of Pluronic L64 and Tetronic 904 [57], where very little PEO density is observed in the core of the micelle. We do, however, observe the exclusion of water from the hydrophobic core of the micelle. We also see a small peak in the density of water at approximately 3.5 Å, which is a characteristic signature of water ordering at a hydrophobic interface. Additionally, from the application of the ICSI method, we are able to determine the average core radius of the micelle as 19.8 ± 0.4 Å.

The ellipticity of the TX-114 micelle, which remains approximately constant during the course of the production simulation (Fig. S4a), is 1.6 ± 0.1 (Fig. 2c). Therefore, the micelle has adopted a triaxial shape, where the length of its primary axis is found to be 101.2 ± 0.2 Å. The surface area of the micelle is determined by measuring its solvent accessible surface area (SASA), which also remains approximately constant throughout the production simulation (Fig. S6a) and has an average value of $4.745 \pm 0.009 \times 10^4$ Å^2 (Fig. 2d).

3.2. Solubilisation of NSAIDs within the TX-114 micelle

After ibuprofen and indomethacin are placed into the aqueous environment around a TX-114 micelle, we see that approximately 40 drug molecules solubilise in the micelle within 40 ns (Fig. 3a & c). In the case of ibuprofen we find that the there is a slight increase in the amount of drugs solubilised within the micelle and then after 200 ns the amount of drug in the micelle remains approximately constant (51 ± 4). Approximately 64% of the ibuprofen molecules are solubilised within the hydrophobic core of the micelle, while the remainder are solubilised within the EO hydrophilic corona of the micelle. The solubilisation of ibuprofen within the micelle results in the micelle transitioning to a prolate, rod-like shape (ellipticity $\sim 2.53 \pm 0.03$, Fig. S4b). With this transition in shape of the micelle, the major axis of the micelle is 36% longer than the pure micelle (137.7 ± 7.3 Å) and the solvent accessible surface area increases to $5.621 \pm 0.007 \times 10^4$ Å^2 (Fig. S6b).

During the solubilisation of indomethacin, we observe that the amount of drug solubilised in the micelle continues to increase until $t \approx 900$ ns. During this time, 80 ± 3 indomethacin molecules are solubilised within the micelle, which is approximately 1.4 times larger than found with ibuprofen. We find that approximately 66% of the indomethacin molecules are solublised in the hydrophobic core of the micelle, with the remaining 34% located in the corona of the micelle. As with the ibuprofen-loaded micelle, we observe that the micelle transitions to a rod-like shape (elliptic-

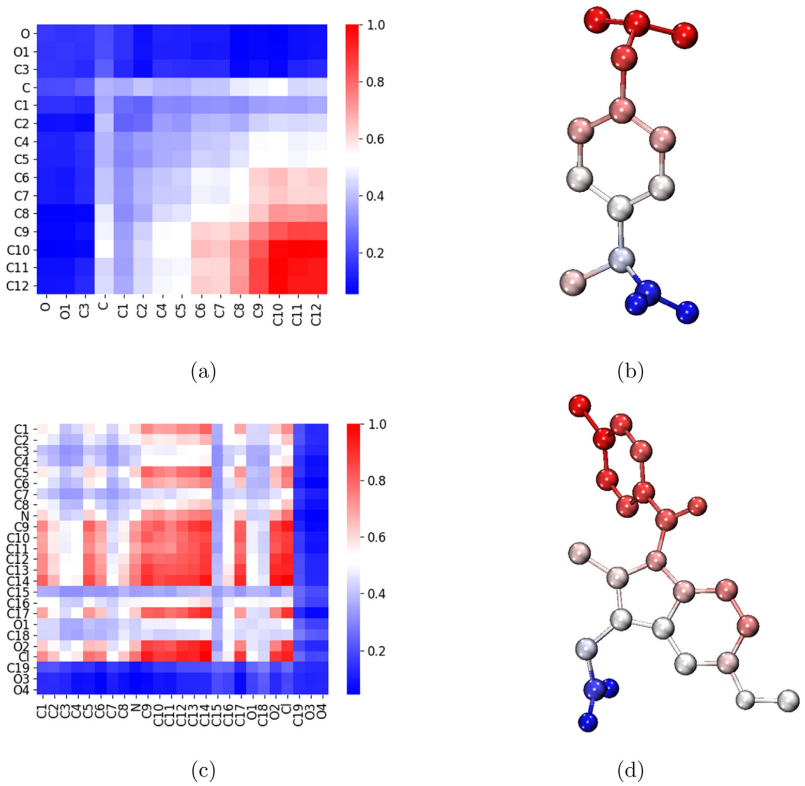


Fig. 5. Interactions between pairs of neighbouring drug molecules. Contact maps which show the amount of contact between two atoms on two neighbouring drug molecules for (a) ibuprofen and (c) indomethacin. Diagrams of (b) ibuprofen and (d) indomethacin molecules which have been coloured by their amount of contact with neighbouring drug molecules, where the colours are consistent with those used in the contact maps. Atom labels used within the contact maps are those shown in Fig. 1.

ity $\sim 3.71 \pm 0.02$, Fig. S4c). As a result of this change in shape, the solvent accessible surface area of the micelle also increases to $6.575 \pm 0.018 \times 10^4$ Å^2 (Fig. S6c).

Unlike with ibuprofen, we find that the solubilisation of indomethacin destabilises the drug-loaded micelle within the simulation timescale. We note that dynamic morphology changes occur for surfactant micelle with and without the solubilisation of small molecule,[59,60], however only as a result of indomethacin solubilisation are we are able to observe this phenomenon here directly on a millisecond timescale. The original TX-114 micelle splits into two daughter micelles. The two resulting micelles have different aggregation numbers, where the larger micelle consists of 100 surfactant molecules and the smaller micelle consists of 50. Indomethacin molecules are solubilised in both of the daughter micelles with 43 ± 2 and 32 ± 2 drug molecules in the larger and smaller micelle, respectively. In both of the daughter micelles, 70% of the drug molecules are solubilised in the hydrophobic core of the micelle and the rest are found in the hydrophilic corona of the micelle.

Both of the daughter micelles are more spherical than the parent micelle was when it destabilised, with the smaller daughter micelle having a spherical shape (ellipticity $\sim 1.32 \pm 0.01$) and the larger one remaining prolate (ellipticity $\sim 1.88 \pm 0.01$) as shown in Fig. S4d. As shown in Fig. S6d, the larger daughter micelle has a major axis length of 109.7 ± 0.9 Å and a solvent accessible surface area of $3.960 \pm 0.007 \times 10^4$ Å^2, while the smaller micelle has a major axis length of 73.4 ± 0.2 Å and a SASA of $2.207 \pm 0.004 \times 10^4$ Å^2.

3.3. Specific Interactions between NSAIDs and TX-114 Micelles

Fig. 4 shows the contacts between the drug molecules and the TX-114 surfactant molecules, where each axis is labeled with the atom names shown in Fig. 1. For both drugs we find that they primarily interact with the same regions of the TX-114 surfactant: the 4-(1,1,3,3-tetramethylbutyl) group (atoms C5 & C6) and the benzene ring (atoms C1A - C1F) found in the hydrophobic tail of the surfactant molecule. Also, we find that the regions of the two drug molecules that interact with the surfactant molecules are largely driven by the fact that the drug molecules orient themselves within the core of the micelle so that their carboxylate groups remain hydrated by the water at the interface of the core of the micelle (Fig. S5). As a result, the carboxylate groups of the ibuprofen and indomethacin ions have only minimal contact with the EO monomers in the hydrophilic headgroups of the surfactant molecules (Fig. 4b & d). The methyl groups of the ibuprofen molecules are the primary portion of the drug molecule that is in contact with

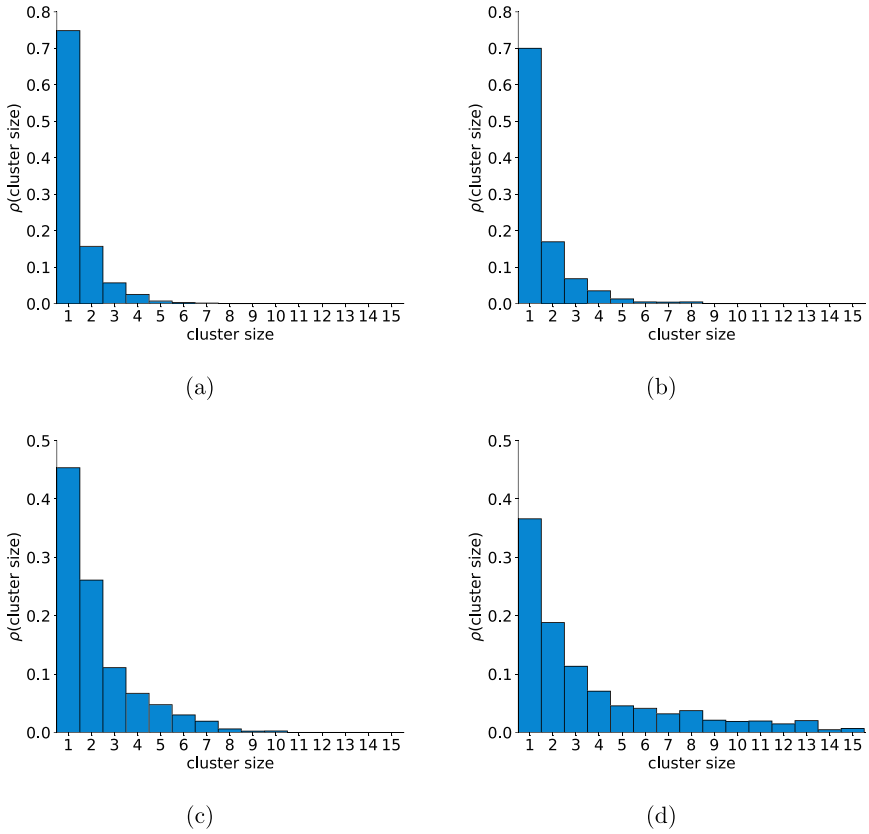


Fig. 6. Evolution of drug clustering during the simulations. Distribution of cluster sizes for ibuprofen during the initial stages (a) and the final stages of the simulation (b). Distribution of cluster sizes for indomethacin during the initial stages of the simulation (c) and the final stages of the simulation (d). We see that solubilisation does not particularly affect the aggregation of ibuprofen, while the assembly of large indomethacin aggregates are promoted by solubilisation.

the surfactant molecules. As for indomethacin, we see that the Cl atoms and the C12 - C14 carbons in the neighbouring benzene ring make significant contact with the hydrophobic tails of the surfactant molecules (Fig. 4d).

In Fig. 4, we show that during the solubilisation process of each drug there is some interaction of the drug molecules with the EO headgroups of the TX-114 surfactant molecules (atoms CA1 - CB2 & O1 - O3). For both ibuprofen and indomethacin the contact with the EO groups is distributed across the whole drug molecule, which indicates that there is no preferential interaction between the drugs and the EO groups, only that the drugs pass by them while moving towards the core of the micelle.

3.4. Aggregation of NSAIDs within Triton X-114 micelles

In order to determine the amount of aggregation of the two different NSAIDs within the core of the micelles, we have measured the amount of contact between the solubilised drug molecules. In Fig. 5a, we see that the ibuprofen molecules interact with one another via the methyl groups (atoms C9 - C12) on one end of the drug molecule (Fig. 5b). It is worth noting that the same region of ibuprofen is involved in the interactions with other ibuprofen molecules as well as the surrounding surfactant molecules.

Meanwhile the interactions between solubilised indomethacin molecules show that significant interactions are found between the chlorine (Cl) atom, the atoms in the neighbouring benzene ring (atoms C9 - C14) and then the ketone group (atoms O2 & C1) (Fig. S13a). As such, the primary mechanism of interaction between the indomethacin molecules is $\pi - \pi$ stacking of their aromatic rings. Then the indomethacin molecules interact via their Cl atoms with the surfactant molecules.

Fig. 6 shows the distribution of drug cluster sizes at the start and end of each simulation. As we have demonstrated in previous sections, at the start of each simulation, most drug molecules are found free in solution, while by the end of each simulation, these molecules are mostly interacting with the TX-114 micelles. We see that at early stages of the simulations, $\approx 75\%$ of ibuprofen clusters contain only a single molecule, while only $\approx 45\%$ of indomethacin clusters correspond to free molecules at the same time. Interestingly, we note that interactions with the micelle do not particularly promote aggregation of ibuprofen, while a range of larger indomethacin aggregates are formed later in the simulations, driven by interactions with the micelle.

To probe these observations in more detail, we calculated the average drug cluster size as a function of its degree of solubilisation within the micelle (denoted by the number of contacts between each drug molecule and non-hydrogen surfactant atoms). We used a rather large interaction cutoff definition (10 Å) when measuring drug-surfactant contacts so as to be sensitive to the overall local environment of the entire drug molecule. These results are presented in Fig. S16. We note that significant clustering of indomethacin is promoted by contact with a relatively small number of TX-114 interactions and that its clustering is reduced as indomethacin molecules come into contact with a greater number of TX-114 atoms. The dependence of clustering upon the degree of TX-114 contacts is not seen as dramatically in the case of ibuprofen but follows a similar overall trend.

4. Conclusions

In this manuscript, we report on the size, shape and structural properties of a Triton X-114 micelle with an aggregation number of ~ 150 molecules. Previously, Yordanova et al. investigated the self-assembly of TX-114 micelles with MD simulations and determined the eccentricity values for micelles of various aggregation numbers [23]. Their results show that micelles with an aggregation number of more than 33 are non-spherical, which is consistent with the observation made here for our significantly larger micelles.

We have also investigated how the solubilisation of NSAIDs affect the structural properties of Triton X-114 micelles. In doing so, we have observed that TX-114 micelles solubilise more ibuprofen molecules than their TX-100 counterparts [61], during the same timescales. This trend is consistent with the experimental observation that for a variety of NSAIDs more drug molecules are solubilised in Triton X-114 micelles than those consisting of Triton X-100 [41,42]. In those experimental studies, the authors have suggested that this is due to the larger aggregation number found for Triton X-114 micelles in comparison to Triton X-100 micelles, and therefore a larger micelle size that accommodates more drug molecules. However, our two investigations, in which we have chosen to use the same aggregation number for each surfactant, suggest that it is not merely due to the difference in aggregation number and instead is a result of the smaller number of ethylene oxide monomers in the hydrophilic headgroups of the Triton X-114 surfactants, which allow for faster diffusion of the drug molecules to the core of the micelle where they are solubilised. In the case of indomethacin, we observed that as the micelle solubilises indomethacin molecules it becomes increasingly large in size and increasingly rod-like in shape until eventually it divides into two unequally sized daughter micelles. These daughter micelles are then, of course, smaller than the pure Triton X-114 micelles. This was also observed in the case of our previous work in which we investigated indomethacin-loaded Triton X-100 micelles [61]. Experimentally, Ullah et al. have found that Triton X-100 and X-114 micelles reduce in size when loaded with Meloxicam and Celecoxib, two other NSAIDs, unlike micelles made of other nonionic surfactants, including Tween 20, Tween 80, Brij 30 and Brij 35, whose size remains unchanged [42]. Our observation of the micelle division into smaller micelles upon loading of indomethacin provides a potential mechanistic description of the process by which this decrease in size occurs.

We find that both of the NSAIDs that we have studied primarily solubilise in the hydrophobic core of the micelle (64% of ibuprofen & 70% of indomethacin) but both drugs have significant numbers solubilised within the hydrophilic corona of the micelle as well. Within the hydrophobic core of the Triton X-114 micelles, we find that both drugs take preferential orientations. We find that they align such that their carboxylate groups are at the interface of the hydrophobic core of the micelle where they can remain hydrated by surrounding water molecules, and the rest of the drug molecules are located deeper within the core of the micelles where they form hydrophobic interactions with the hydrophobic tails of the Triton X-114 molecules and the hydrophobic groups of neighbouring drug molecules. The interactions we observe between the carboxylate group and the 4-(1,1,3,3-tetramethylbutyl) group of the ibuprofen molecules and the benzene ring of the Triton X-114 molecules are consistent with the experimental findings of Rub which showed that the same two molecules interact via their respective hydrophobic regions [40].

Importantly, we show here that the interactions between the drug molecules themselves and between the drugs and surfactants within a drug delivery vehicle are both important to consider when designing a stable formulation. As in the case of the indomethacin-loaded TX-114 micelles, we observe that there is significant aggregation of the drug molecules within the core of the micelle, which leads to the destabilisation of the micelle. The ibuprofen molecules do not form large clusters within the core of the micelle, and the micelle remains stable with the larger aggregation number. This insight provides important information for the further optimisation of Triton-based drug delivery formulations.

CRediT authorship contribution statement

Hrachya Ishkhanyan: Software, Validation, Formal analysis, Investigation, Data curation, Writing – Original Draft, Writing – Review & Editing, Visualisation, Funding acquisition. **Robert M. Ziolek:** Software, Validation, Formal analysis, Writing – Original Draft, Writing – Review & Editing, Visualisation. **David J. Barlow:** Conceptualization, Methodology, Writing – Review & Editing. **M. Jayne Lawrence:** Conceptualization, Methodology. Writing – Review & Editing. **Armen H. Poghosyan:** Writing – Review & Editing, Supervision. **Christian D. Lorenz:** Conceptualization, Methodology, Resources, Writing – Original Draft, Writing – Review & Editing, Supervision, Project administration, Funding acquisition.

Declaration of Competing Interest

The authors declare that they have no known competing financial interests or personal relationships that could have appeared to influence the work reported in this paper.

Acknowledgement

Through C.D.L.'s membership within the UK HPC Materials Chemistry Consortium, which is funded by the Office of Science and Technology through the EPSRC High End Computing Programme (Grant No. EP/L000202, EP/R029431), the use of ARCHER, the UK National Supercomputing Service (http://www.archer.ac.uk) and the UK Materials and Molecular Modelling Hub (MMM Hub), which is partially funded by the EPSRC (EP/P020194/1, EP/T022213), was used for the molecular dynamics simulations presented in this work. A special thanks to "Tekeyan Trust London" whose funding has made H.I.'s research at KCL possible. R.M.Z acknowledges the Engineering and Physical Sciences Research Council (EPSRC) for the funding that allowed him to work on this project (EP/V049771/1).

Appendix A. Supplementary material

Supplementary data associated with this article can be found, in the online version, at https://doi.org/10.1016/j.molliq.2022.119050.

References

[1] S. Senapati, A.K. Mahanta, S. Kumar, P. Maiti, Signal Transduct. Target. Ther. 3 (2018) 7.
[2] M. Akhtar, M. Jamshaid, M. Zaman, A.Z. Mirza, J. Drug Deliv. Sci. Technol. 60 (2020) 102079.
[3] P. Couvreur, F. Puisieux, Protein Therapeutics Using Recombinant Technology, Adv. Drug Deliv. Rev. 10 (1993) 141–162.
[4] D.D. Lasic, Nature 380 (1996) 561–562.
[5] Z. Ahmad, A. Shah, M. Siddiq, H.-B. Kraatz, RSC Adv. 4 (2014) 17028–17038.
[6] P. Walde, S. Ichikawa, Biomol. Eng. 18 (2001) 143–177.
[7] L. Sanderson et al., PLOS Negl. Trop. Dis. 15 (2021) e0009276.
[8] I. Marzuoli, C.H.B. Cruz, C.D. Lorenz, F. Fraternali, Nanoscale 13 (2021) 10342–10355.
[9] D.L. Pink, O. Loruthai, R.M. Ziolek, A.E. Terry, D.J. Barlow, M.J. Lawrence, C.D. Lorenz, J. Colloid Interface Sci. (2021) 12.
[10] I.E. Kepiro, I. Marzuoli, K. Hammond, X. Ba, H. Lewis, M. Shaw, S.B. Gunnoo, E. De Santis, U. Lapriska, S. Pagliara, M.A. Holmes, C.D. Lorenz, B.W. Hoogenboom, F. Fraternali, M.G. Ryadnov, ACS Nano 14 (2020) 1609–1622.
[11] D.L. Pink, O. Loruthai, R.M. Ziolek, P. Wasutrasawat, A.E. Terry, M.J. Lawrence, C.D. Lorenz, Small 15 (2019) 1903156.
[12] D.T. Allen, Y. Saaka, M.J. Lawrence, C.D. Lorenz, J. Phys. Chem. B 118 (2014) 13192–13201.
[13] C.D. Lorenz, C.-M. Hsieh, C.A. Dreiss, M.J. Lawrence, Langmuir 27 (2011) 546–553.
[14] I.F. Uchegbu, S.P. Vyas, Int. J. Pharm. 172 (1998) 33–70.
[15] S. Schreier, S.V. Malheiros, E. de Paula, Biochimica et Biophysica Acta (BBA) - Biomembranes 1508 (2000) 210–234, Detergents in Biomembrane Studies.
[16] Surfactants and Interfacial Phenomena, John Wiley & Sons Inc, 2012, pp 123–201.
[17] M.J. Lawrence, Eur. J. Drug Metab. Pharmacokinet. 19 (1994) 257–269.
[18] A. Makhlouf, I. Hajdu, I. Badea, in: A.M. Grumezescu (Ed.), Organic Materials as Smart Nanocarriers for Drug Delivery, William Andrew Publishing, 2018, pp 561–600.
[19] A.H. Poghosyan, N.P. Schafer, J. Lyngsø, A.A. Shahinyan, J.S. Pedersen, D.E. Otzen, Protein Engineering, Design Select. 32 (2019) 175–190.
[20] M.A. Rub, N. Azum, F. Khan, A.M. Asiri, J. Phys. Org. Chem. 30 (2017) e3676, e3676 POC-16-0215.R1.
[21] L. Koshy, A.H. Saiyad, A.K. Rakshit, Colloid Polym. Sci. 274 (1996) 582–587.
[22] C. Bordier, J. Biol. Chem. 256 (1981) 1604–1607.
[23] D. Yordanova, I. Smirnova, S. Jakobtorweihen, J. Chem. Theory Comput. 11 (2015) 2329–2340, PMID: 26574428.
[24] E. Ritter, D. Yordanova, T. Gerlach, I. Smirnova, S. Jakobtorweihen, Fluid Phase Equilibria 422 (2016) 43–55, Special issue on Biothermodynamics.
[25] A. Klamt, U. Huniar, S. Spycher, Keldenich J. 112 (2008) 12148–12157.
[26] N.E. Lane, J.M. Thompson, Am. J. Med. 103 (1997) 25–35.
[27] P. Needleman, P.C. Isakson, J. Rheumatol. 24 (1997) 2–7.
[28] G.A. Green, Clin. Cornerstone 3 (2001) 50–59.
[29] C.S. Boynton, C.F. Dick, G.H. Mayor, J. Clin. Pharmacol. 28 (1988) 512–517.
[30] E.H. Gesine, C.M. Christel, J. Pharm. Sci. 86 (1997) 854–857.
[31] J. Simon, T. Lionel, M. Charles, Int. J. Pharm. 268 (2003) 37–45.
[32] L. Fabrice, P. Fabienne, M. Myriam, J. Pharm. Biomed. Anal. 23 (2000) 793–802.
[33] T. Benbow, J. Campbell, Drug Dev. Ind. Pharm. 45 (2019) 1849–1855.
[34] M. Ahuja, A.S. Dhake, S.K. Sharma, D.K. Majumdar, AAPS J. 10 (2008) 229.
[35] C.A. Heyneman, C. Lawless-Liday, G.C. Wall, Drugs 60 (2000) 555–574.
[36] J. Araújo, E. Gonzalez, M.A. Egea, M.L. Garcia, E.B. Souto, Nanomed.: Nanotechnol. Biol. Med. 5 (2009) 394–401.
[37] M.L. McPherson, N.M. Cimino, Pain Med. 14 (2013) S35–S39.
[38] A. Gliszczyńska, M. Nowaczyk, Molecules 26 (2021) 1576.
[39] D. Yordanova, E. Ritter, T. Gerlach, J.H. Jensen, I. Smirnova, S. Jakobtorweihen, J. Phys. Chem. B 121 (2017) 5794–5809.
[40] M.A. Rub, J. Lumin. 197 (2018) 252–265.
[41] I. Ullah, M.K. Baloch, S. Niaz, A. Sultan, I. Ullah, J. Solution Chem. 48 (2019) 1603–1616.
[42] I. Ullah, M.K. Baloch, G.F. Durrani, J. Solution Chem. 40 (2011) 1341–1348.
[43] K. Vanommeslaeghe, E. Hatcher, C. Acharya, S. Kundu, S. Zhong, J. Shim, E. Darian, O. Guvench, P. Lopes, I. Vorobyov, A.D. Mackerell Jr, J. Comput. Chem. 31 (2010) 671–690.
[44] W.L. Jorgensen, J. Chandrasekhar, J.D. Madura, R.W. Impey, M.L. Klein, J. Chem. Phys. 79 (1983) 926–935.
[45] M.J. Abraham, T. Murtola, R. Schulz, S. Páll, J.C. Smith, B. Hess, E. Lindahl, SoftwareX 1–2 (2015) 19–25.
[46] L. Martinez, R. Andrade, E.G. Birgin, J.M. Martìnez, J. Comput. Chem. 30 (2009) 2157–2164.
[47] S. Nosé, Mol. Phys. 52 (1984) 255–268.
[48] W.G. Hoover, Phys. Rev. A 31 (1985) 1695–1697.
[49] M. Parrinello, A. Rahman, J. Appl. Phys. 52 (1981) 7182–7190.
[50] B. Hess, H. Bekker, H.J.C. Berendsen, J.G.E.M. Fraaije, J. Comput. Chem. 18 (1997) 1463–1472.
[51] Richard J. Gowers, Max Linke, Jonathan Barnoud, Tyler J.E. Reddy, Manuel N. Melo, Sean L. Seyler, Jan Domanski, David L. Dotson, Sébastien Buchoux, Ian M. Kenney, Oliver Beckstein, MDAnalysis: A Python Package for the Rapid Analysis of Molecular Dynamics Simulations, in: Proceedings of the 15th Python in Science Conference, 2016, pp. 98–105.
[52] N. Michaud-Agrawal, E.J. Denning, T.B. Woolf, O. Beckstein, J. Comput. Chem. 32 (2011) 2319–2327.
[53] W. Humphrey, A. Dalke, K. Schulten, J. Mol. Graph. 14 (1996) 33–38.
[54] S. Mitternacht, F1000 Res. 5 (2016) 189.
[55] B. Lee, F.M. Richards, J. Mol. Biol. 55 (1971) 379–400.
[56] R.M. Ziolek, J. Omar, W. Hu, L. Porcar, G. Gonzalez-Gaitano, C.A. Dreiss, C.D. Lorenz, Macromolecules 53 (2020) 11065–11076.
[57] R.M. Ziolek, P. Smith, D.L. Pink, C.A. Dreiss, C.D. Lorenz, Macromolecules 54 (2021) 3755–3768.
[58] P.H. Elworthy, M.S. Patel, J. Pharm. Pharmacol. 36 (1984) 116–117.
[59] G. Zaldivar, M. Conda-Sheridan, M. Tagliazucchi, Langmuir 37 (2021) 3093–3103, PMID: 33683125.
[60] R. Takahashi, T. Narayanan, S.-I. Yusa, T. Sato, Macromolecules 51 (2018) 3654–3662.
[61] H. Ishkhanyan, N.H. Rhys, D.J. Barlow, J.M. Lawrence, C.D. Lorenz, Nanoscale (2022), https://doi.org/10.1039/D1NR07936K.

Chapter 5

AICON: A Python package to analyze aspherical nanoparticles

Being able to accurately describe the interface of a nanoparticle is key to understanding key aspects including the internal structure and interfacial properties which govern the functionality of the nanoparticle. Currently, the computational methods that exist to define the interface of a nanoparticle provide reasonable results for sphere-like nanoparticles but are not suitable to analyze aspherical structures, such as capsules, or rod-like structures. In this chapter, aspherical interface constructor for nanoparticles (AICON), a new algorithm which can be used to describe both sphere-like and aspherical nanoparticles is proposed. With the accurate description of the location of the interface of the nanoparticle, this algorithm then allows for various other important quantities (e.g. densities of different atom/molecule types relative to the interface, volume of the nanoparticle, amount of solubilized molecules within the nanoparticle) to be calculated. Furthermore, a protocol is described, that can help enhance the performance of Python codes for computationally intensive projects.

5.1 Introduction

In biomedicine, nanoparticles have become an important area of research, with a wide-range of applications, e.g. biomedical imaging,[196,197] drug delivery.[198,199]

Understanding their interfacial properties, which governs their interactions with the solute, the substrate and with each other, is crucial, in order to develop high quality materials. The surface of a nanoparticle can be modified in numerous ways, to alter its functionality and tailor it for a specific target.[200,201] The shape, size and surface area of a nanoparticle also play an important role in various interactions, and therefore are used to optimise nanoparticles and nanoparticle formulations.[202]

Molecular dynamics (MD) simulations provide time-dependent atomistic description of coordinates and forces for a many-particle system. By obtaining every atom's position, one is able to describe the water-nanoparticle interface in many ways. Furthermore, having information about the interface, allows one to quantify various useful properties, such as volume, hydration, density profiles, solubilization of different molecules inside of the nanoparticle, etc. There are several methods to describe surfaces and interfaces, such as the marching cubes algorithm,[203] Willard-Chandler method,[204] etc.

Allen and Lorenz[170] suggested a method to construct continuous interfaces for simulated nanoparticles. Ziolek et al,[188] proposed an alternative approach to describe the intrinsic core–shell interface (ICSI) of a structure. The above-mentioned methods show great results with nanoparticles that have spherical or quasi-spherical shape. However, this methodology is not suited to describe situations in which the nanoparticles are not highly symmetric. In this work, an algorithm to define a core-shell interface regardless of the asphericity of the nanoparticle is proposed. Furthermore, calculations of the volume and density profiles of different atoms in regard to the interface are demonstrated. Additionally, a detailed description of the algorithmic implementation using Python programming language has been included highlighting software optimization for dealing with intensive computational cases.

5.2 Methods

The AICON package has been written in Python and Cython[205] with an extensive use of MDAnalysis,[206,207] NumPy,[208] and SciPy[209] libraries.

5.2.1 Defining the interface

To define the interface, one must first provide a list of the atoms that make up the core of the nanoparticle. In order to input this list of atoms, the algorithm utilises the capability of MDAnalysis to easily generate atomic group definitions. Then, to define the internal and interface regions of a nanoparticle, convex hull algorithm, as implemented in the SciPy library, was used. As described in Chapter 2, a convex hull for a given set of points is the smallest convex set containing these points. After defining the hull, the volume and densities can be calculated.

Volume calculation: The volume can be calculated via two well-established methodologies - Monte Carlo integration, or a Riemann sum method. In the first case, the grid is populated by random points, and for every point a check occurs whether the point is inside of the hull or not. The check is done in the following manner. Vectors, $\mathbf{p}_i$, are constructed from the centroid of each triangle, that forms the interface, to the i-th generated point and the cross-product is calculated between p_i and normal vector $\mathbf{n}$ of the triangle. The point is inside if the following equation holds:

$$\sum_i \sigma(\mathbf{p}_i \times \mathbf{n}) \equiv -S \tag{5.1}$$

where S is the number of facets or triangles on the hull and σ is the sign function. The volume can be estimated as:

$$V = \frac{N_{in}}{N_{tot}} V_{box} \tag{5.2}$$

where N_{tot} and N_{in} are the numbers of generated points in total, and the ones that are inside of the convex hull respectively. V_{box} is the volume of the simulation box. In the Riemann method, the interface is divided into smaller

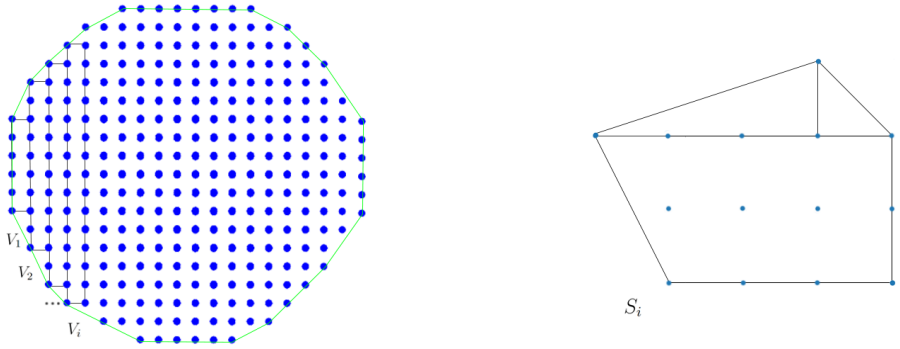


Figure 5.1: Schematic representation of Riemann sum method. A cross-section of a 3D spherical particle is shown on the left and an isolated slice is shown on the right.

slices, V_i, with a cross-section area of S_i (Figure 5.1). The grid allows one to easily calculate volumes of each slice by iterating over the 2D planes of the grid, calculating the surface area, S_i, of each cross-section and multiplying it by the grid step d. Then, the total volume can be approximated as:

$$V = \sum_i V_i = \sum_i S_i d \tag{5.3}$$

where V_i and S_i are the volume and surface area of i-th slice of the nanoparticle, and d is the grid spacing. V_i for each slice can be computed trivially. If the surface of the slice contains less than three points, it is ignored, and the value of d is incremented by d until a valid surface is encountered, otherwise the surface will be a combination of trapezoids and triangles.

Density calculation: In order to calculate number densities, the number of particles in each grid cell must be calculated and divided by the volume of that cell. The spacing, d, of the grid is 1Å, whereas the size of one water molecule is roughly ∼3Å, so it is impossible to find more than one particle in a grid cell. To overcome this issue, the grid cells are merged into larger cells of equal sizes. The new cells have dimensions of $c_r d$, where rescale factor, c_r, is a non-zero integer. Then, the number density of particles is calculated for each large cell, rather than for the initial smaller cells.

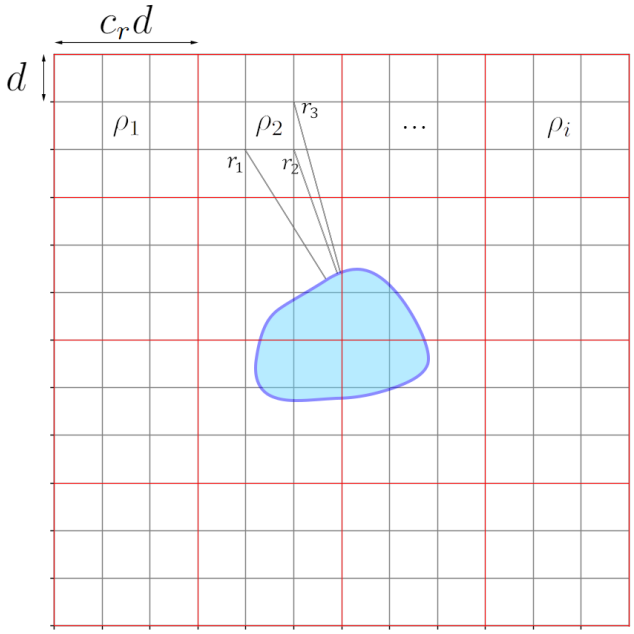


Figure 5.2: The grid representation of the simulation box in 2D. The initial grid is in black, where $d = 1$Å. The densities are calculated in a larger grid (in red).

$$\rho_i = \frac{N_i}{V_i} \tag{5.4}$$

where i is the i-th region. The distance between each particle and the hull is calculated using the PyGEL3D library.[210,211] If the particle is inside of the hull, the distance is multiplied by -1. Then, the distance is discretised such that it is binned by the size of the larger cells, and the density is stored in an array whose index is representative of the bin number of the particle (as shown in Figure 5.2, the density at d_1, d_2 and d_3 is ρ_2). Finally, for each distance, r, the average of the density across all the bins at distance r is taken.

5.2.2 Enhancing code performance

A timescale for an average molecular dynamics simulation is on the order of 100's - 1000's of nanoseconds. Assuming a timestep of 0.002 fs, a 500 ns simulation will contain $2.5 * 10^8$ steps, out of which $10^3 - 10^5$ trajectory points

(frames) will be written to the disk. Statistically relevant macroscopic parameters are obtained by using a significant portion of frames following the law of large numbers. Hence, the algorithmic design and its implementation must be fine tuned to provide both accuracy and performance. Here, a novel software design, providing large performance enhancements when compared to the original implemented Python algorithm, is described. Three major components attribute to the increased performance for a Python code - optimized code, compilation of slow functions and code parallelization. Code optimization is outside of the scope of this work, but it is something to always keep in mind when developing a program in any language. The next subsections will discuss the impact of the other components.

Compilation

In its standard implementation (CPython),[156] Python is an interpreted language, meaning that the code does not need to be compiled into an executable in order to be executed. There is, however, an intermediate compilation step performed (into bytecode), which is subsequently executed by the interpreter rather than processed as a machine code. That is a significant optimization, but not enough to compete with some compiled languages. However, there are different frameworks and Python implementations available, that allow Python code to be compiled. Examples are Cython,[205] Numba,[212] Pypy,[213] etc. In this case and following the structure of the Python project, Cython has been selected to provide further performance optimization.

In simple words, Cython is a superset of Python, that can compile a Python (.py file), or an extended Python (.pyx file) script into a C code, which then can be compiled into an extension module, which is allowed to be imported and used in pure Python code (Figure 5.3). Any Python file can be compiled, but Cython offers additional features, such as type definitions, global interpreter lock (GIL) release, and working directly with C extensions, to name a few, that can further improve performance. In this project, the functions were compiled after simply defining the variable types using the special syntax



Figure 5.3: Schematic diagram providing a successful Cython workflow.

of Cython.

Parallelization

Modern hardware architectures provide computers with multi-core processors enabling different parallelization schemes as suggested in the Flynn's Taxonomy.[214] As a starting point, the original algorithm generates instructions (tasks) which are sequentially executed and subsequently collected producing the desired result. Thus, if the algorithm generates these instructions that can be executed using many threads (tasks) then an enhancement in the execution performance is expected. However, it is important to understand that this strategy also demands a synchronization strategy coordinating the access to an object or resources to avoid the so-called race-condition.[215] In CPython, a single thread is allowed to run in the interpreter at any given time, and it is assured by the global interpreter lock (GIL). Although, GIL ensures thread-safety, it can be a huge bottleneck in Python programs that would benefit from multi-threading. The Python community has developed new tools, such as the multiprocessing library, that enables to harvest the power of multi-threaded machines while still complying with thread-safety synchronization. In this work,the multiprocessing module from the Python standard library was used.

5.3 Results

5.3.1 Volume

Volume calculations were tested on structures with known volumes - a cylinder with a radius, and half-height of 2.9 nm and a sphere with a radius of 2.9 nm (Figure 5.4). For the cylinder, Monte Carlo integration gave a result of 154.17

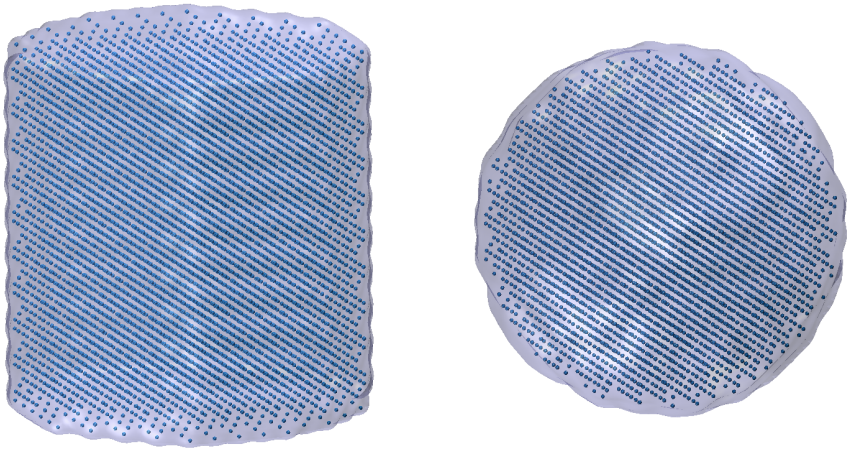


Figure 5.4: Test structures for the volume calculations: cylinder (left) and sphere (right)

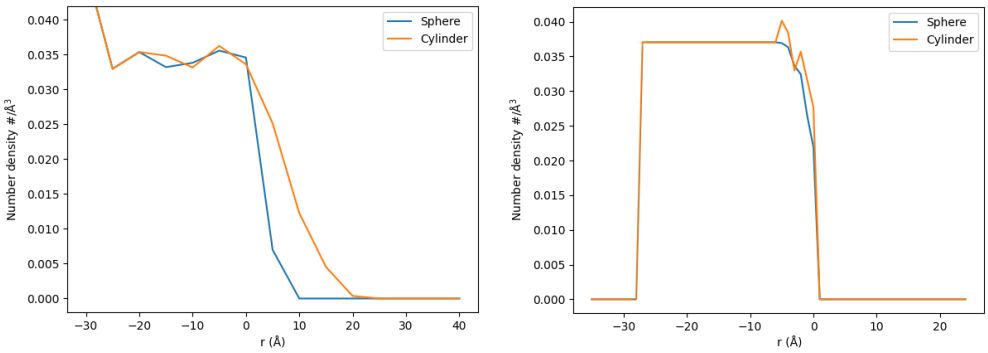


Figure 5.5: Density of particles in the test structures estimated by a standard approach (left) and the AICON algorithm (right).

nm^3, which differs from the expected 153.24 nm^3 by 0.6%. The Riemann integration on the other hand, gave a higher error of 15.4%, with a value of 129.6 nm^3. For the sphere, 103.14 nm^3 was obtained using the Monte Carlo method, relative to the actual value of 102.16 nm^3, with an error of 0.9%. The Riemann integration gave a value of 97.25 nm^3 with a relative error of 4.8%. It is worth noting, that the expected values do not represent the real volume, and are a slight overestimation, as the structures are not continuous. The underestimation from Riemann method is inherent, as from Figure 5.1 (the convex hull is shown in green) it can be seen that a significant portion of volume is excluded from the calculations.

5.3.2 Densities

Similarly, the selected test structures (Figure 5.4) are used to evaluate the accuracy of the density methodology. The number density of both structures inside their bulk can be estimated to 0.0375Å^{-3}. In Figure 5.5 this estimation is shown, which is done by a standard approach, that calculates densities relative to the center of mass of the structure, and the algorithm described in this chapter. While the standard approach yields good results for the sphere, it fails to properly describe the density inside of the cylinder, showing above zero density values beyond the interface ($r = 0$), as a result of the asymmetry of the structure. This happens, as while moving further away from the center of mass of an asymmetric structure, the chemical environment does not remain homogeneous, resulting in density values at distances where particles are absent. The algorithm in this chapter, however, provides correct density values both for the sphere and the cylinder, as the calculations are done relative to the interface of the structure. The drop of density at $r = -29\ \mathring{A}$ is unique to this method. When calculating the density, the minimal distance from the surface of the interface is determined for each particle. As the center of the structure is approached from one side of the interface, the minimum distance from the interface for every particle is determined based on their proximity to the interface. However, as the center is surpassed and the other side is reached, the particles' minimum distance from the interface is recalculated based on their new position. Therefore, the center of geometry of the structure represents the deepest point that can be reached with this method. Beyond the center, the density values gradually decrease until they eventually reach 0. Furthermore, results of the AICON were compared to that determined by the nanoCISC algorithm for two different structures,[170] a semi-spherical micelle formed by TX100 surfactants, and an aspherical micelle formed by TX100 surfactants and solubilized indomethacin molecules. Figure 5.6 shows the results for both algorithms when analyzing the semi-spherical micelle (Figure 5.7 left). Both algorithms perform similarly in terms of density values, the differences being

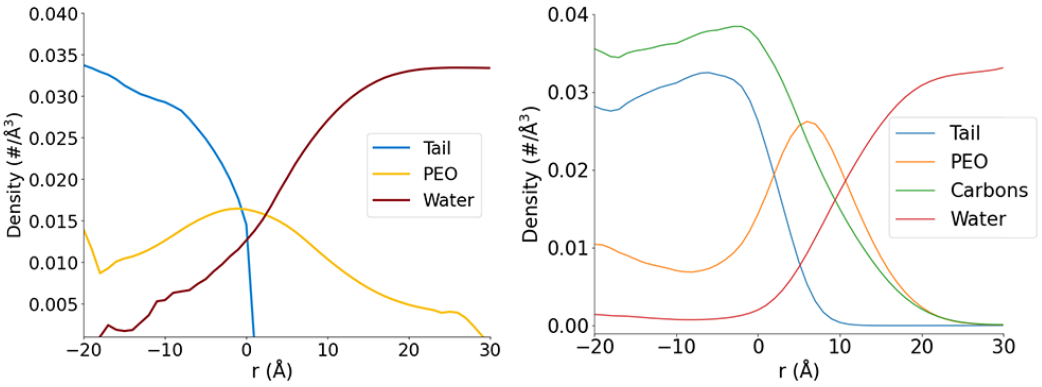


Figure 5.6: Density profiles of water, Triton X-100 hydrophobic tail and hydrophilic head. Comparison of results from two algorithms (left - algorithm of this thesis, right - nanoCISC).

mainly shifted peaks, which is expected, as the nanoCISC algorithm describes the interface using user-defined anchor points, after which the interface is constructed by interpolating between these points, whereas the AICON code uses any atom inside of the hydrophobic parts and interpolates between them. On the other hand, on an elongated nanoparticle (Figure 5.7 right), the nanoCISC algorithm shows some artefacts, whereas the new algorithm provides more adequate results (Figure 5.8). First issue to note, is the water density (Figure 5.8 right), where it monotonically increases past the average density value of water in bulk ($\sim 0.033 \text{Å}^{-3}$), whereas the new algorithm gives the correct values. Secondly, due to the asymmetry of the micelle, one axis is significantly larger than the other two. Therefore, algorithms which are symmetry-dependent are prone to provide results with larger statistical error. The right plot in Figure 5.8 shows a continuous increase of hydrophilic head density as it goes deeper into the micelle. However, this might not be a correct estimation for asymmetric micelles for the same reason explained before (Figure 5.5). In the left graph, on the other hand, the PEO density, after reaching its peak near $r = 0$, decreases to 0. This is expected, as the distances are calculated relative to the convex hull of the interface, so $r = 0$ means any point on the interface. Hence, the AICON method allows the core or shell thickness of an asymmetric, non-spherical nanoparticle to be calculated. The large water density inside of

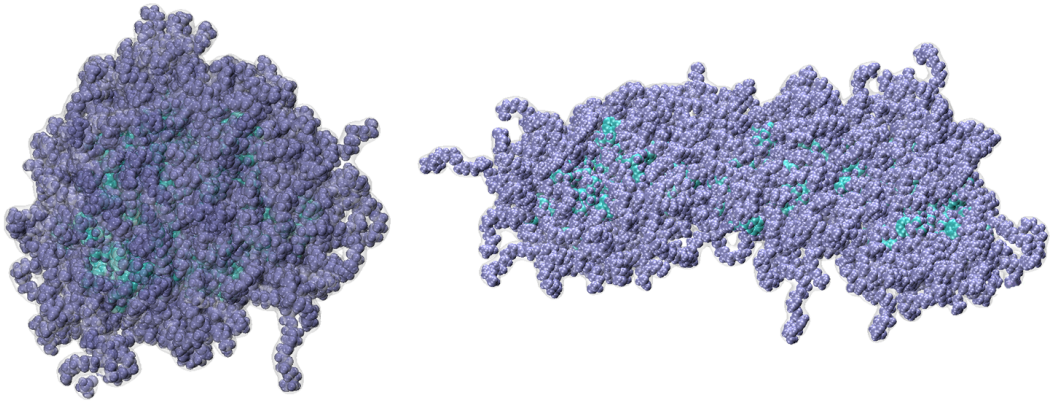


Figure 5.7: Snapshots of (left) the semi-spherical TX100 micelle and (right) the elongated TX100 micelle.

the micelle in both cases is the result of the micelle division in the simulation, during which a large amount of water penetrates the region of the micelle, where the splitting occurs.

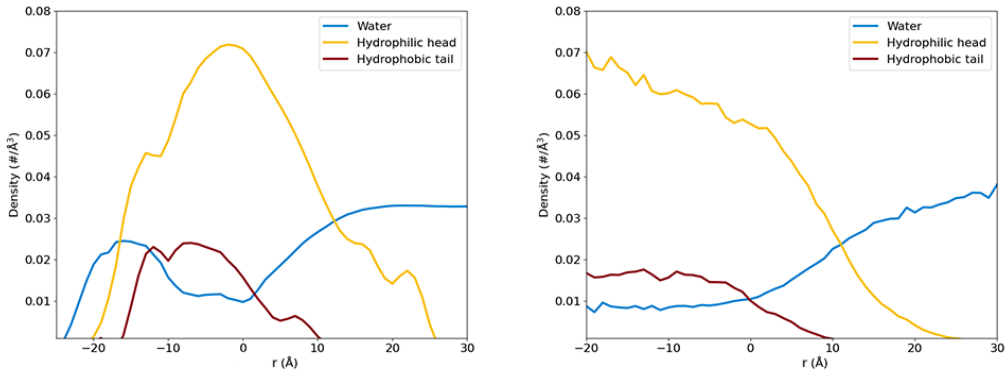


Figure 5.8: Density profiles of water, Triton X-100 hydrophobic tail and hydrophilic head. Comparison of results from two algorithms (left - AICON, right - nanoCISC).

5.3.3 Code performance analysis

In this section a detailed performance analysis of the code is displayed based on the implementation techniques discussed in the methods section. The protocol suggested is as follows. Firstly, one needs to identify the bottleneck segment of their code. The process to identify the bottlenecks in this thesis is described in the Appendix C. Secondly, the identified functions are separated from the main

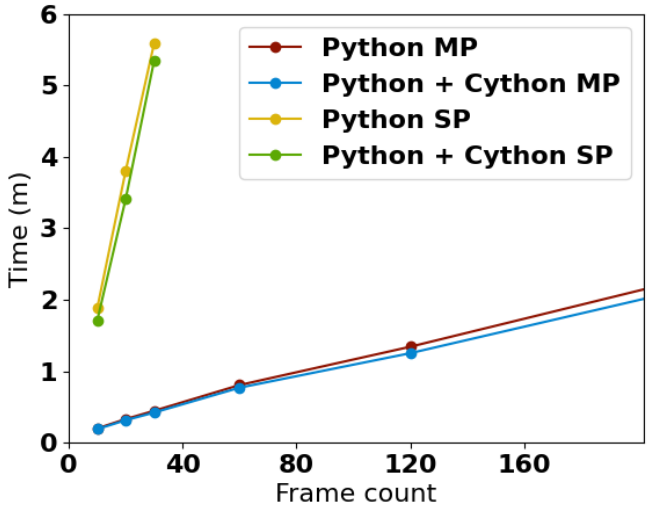


Figure 5.9: Performance time for different techniques to compute densities in AICON algorithm as a function of the number of frames employed.

code into an extended Python script file (.pyx) and compiled using the Cython compiler. In this code, the function that took the most computational time to execute, and hence was compiled, was the function responsible for distance calculations. Finally, the code is parallelized to use multiple CPU processes (8 in this test) simultaneously. The results are shown in Figure 5.9. Using a single process, the compiled version offers an average performance boost of ∼2.25%. Implementing a simple parallelization through multiprocessing, increases the performance of the non-compiled code dramatically. The rate of change in computational time depending on the number of frames, is ∼18 times less for parallelized code, than for the single process version. Furthermore, the parallelizing of a compiled code offers an additional ∼7% performance boost. Finally, the time complexity of the code can be estimated as $O(Nh)$, where N is the number of particles for density calculations and h is the number of vertices on the convex hull. With a constant h, the execution time increases linearly with an increasing N (Figure 5.10). This plot was produced by running the algorithm with varying number of atoms over 300 frames of the same simulation trajectory.

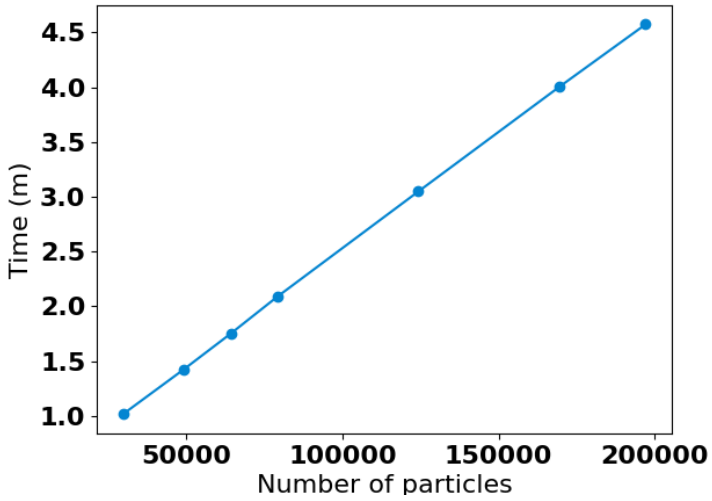


Figure 5.10: Linear dependence of the execution time on the number of particles.

5.4 Conclusion

Understanding the properties of nanoparticle interfaces and how they interact with different materials is essential in order to synthesize high quality nanoparticle formulations. MD simulations provide spatial information about every particle throughout the trajectory allowing one to conveniently define water-nanoparticle interfaces using various methods. In this chapter, a new approach of interface definition has been described. It was shown that this approach provides adequate results for spherical as well as non-spherical nanoparticles.

Finally, a protocol to enhance the performance of Python codes was proposed. However, these concepts are mostly applicable and practical with other languages as well. It was demonstrated, that a simple parallelization of an existing pure Python code, can boost the performance dramatically, with the boost rate depending on the specifications of the system the code is executed on. Furthermore, code compilation can offer an additional increase in the performance. The amount of performance enhancement is a subject to what part of the code was compiled and how the compilation was performed. The results of this analysis show that by solely defining variable types decreases the code execution time by $\sim$7%.

5.5 Future work

The AICON algorithm implementation and optimization are still under active development including a release in the near future. Volume calculations using the Riemann method will be improved, by increasing the resolution of the grid mesh. Furthermore, the volume calculations will also be parallelized to allow averaging over large segments of trajectories. There are two major chages to implement. First, is changing the definition of the interface to a more complex and concave shape. Some solvent particles that are outside of the interface, will be considered inside as a result of convexity of the interface (Figure 5.11, black arrows point to these particles). Figure 5.11 shows an example of a concave hull (yellow, dashed line), which will be implemented in the future. Second, is the usage of Cython's more complex features, which will optimize the performance further. A few other corrections and optimizations need to be done. Finally, when the code is fully functional, the scalability of parallelization will be highly improved, to allow the code to be executed on a cluster of CPUs, by the usage of external libraries. Although this code is fast enough, and running it on a cluster could be an overkill, a well tested and documented protocol on this example will be highly beneficial for time-consuming software.

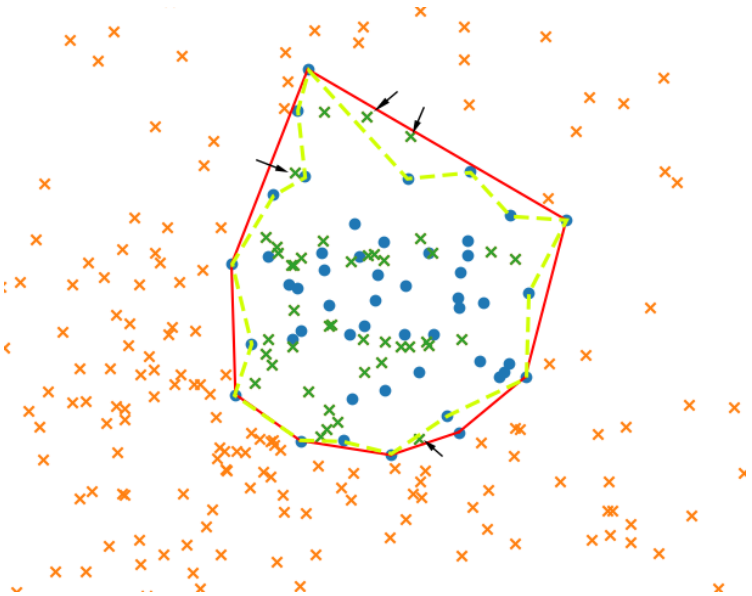


Figure 5.11: A 2D convex hull (red) for a set of particles (blue) for which the interface needs to be defined. Solvent particles (marked with ×) inside of the hull are in green. A concave representation of an interface is in light green.

Chapter 6

Structural properties of Triton X-100- and Tyloxapol-based mixed micelles

Surfactants can be covalently linked to form oligomers, properties of which differ from their monomeric variants. Surfactant oligomers often possess qualities, such as a lower critical micelle concentration (CMC) and better wetting properties, that result in them being advantageous over their monomeric counterparts in various applications. Furthermore, such structures can be further modified by introducing other surfactants to the system. Such mixed surfactant micelle systems can benefit from the extended functionality provided from both surfactant types which can prove to be advantageous over single-type drug formulations. In this chapter, mixed micelles formed by Triton X-100 and its oligomer, Tyloxapol, have been studied. In total, eight systems were investigated containing different ratios of each surfactant. The size and shape of each micelle were evaluated using various analysis methods. Furthermore, the interface of each micelle was computed, which allowed the internal structure of the micelle to be determined by calculating the density profiles of different species relative to the micelles interface. Also, by being able to determine the interface of the micelle, the volume which take complex shapes is able to be calculated. Additionally, by conducting a neighbour analysis, it has been

assessed whether one type of surfactant has affinity towards itself or the other.

6.1 Introduction

Surfactants are amphiphilic molecules that, in aqueous environments, can self-assemble into different structures, such as micelles, vesicles, rod-like particles etc. Due to their ability to self-assemble, to lower surface tension and their wetting properties, they have found use in a wide variety of applications, e.g. cleaning materials, cosmetics, agriculture and pharmaceutics.[22,25,31,216] Surfactants can be classified as anionic (negatively charged), cationic (positively charged), zwitterionic (carrying both positive and negative charges) and non-ionic (no charge). In this study, the non-ionic surfactant Triton X-100 and its oligomer, Tyloxapol, have been studied.

Oligormeric surfactants are synthesized by covalently linking single molecules via a spacer. Surfactant oligormers have been a subject of interest for decades, and numerous studies have shown that oligomers have superior properties in different aspects compared to their monomeric counterparts.[217–219] Early comparative studies indicated that surfactant dimers and trimers, have lower critical micelle concentrations (CMC) and better surface tension reduction capabilities.[219–222] Bunton et al[220] demonstrated that the CMC is lower for dicationic detergents compared to cationic surfactant, cetyltrimethylammonium bromide (CTABr). Dam et al[222] have shown that alongside with the low CMC in dimeric quaternary ammonium bromides, these surfactants show better oil solubilization capabilities than anionic sodium dodecyl sulfate (SDS) or CTABr. This was further demonstrated by computational studies. Maiti et al.[223] have shown the decrease of CMC with the increase of the polymerization degree in model surfactants in coarse-grain simulations, and the same trend has been demonstrated for SDS via dissipative particle dynamics simulations conducted by Wu et al.[224] More recently, Wang et al.,[225] through coarse-grain simulations, have investigated the effect of spacer length in dimeric dimethylcetylammonium bromide-based surfactants on the shape and structure of the

micelles resulting from their self-assembly. Furthermore, Zhou et al.[78] has shown that antimicrobial capabilities of ammonium surfactants improve with the increasing level of oligomerization. The trimeric, tetrameric and hexameric surfactants, at concentrations that are non-toxic to mammalian cells, show higher effectivity against E. coli bacteria, as opposed to their dimeric and monomeric counterparts. Dharaiya et al.[226] have compared the solubilization of disphenol A in Tyloxapol and Triton X-100 micelles, where Tyloxapol micelles have shown to have better solubilization capabilities than Triton X-100 micelles.

In some cases, micelles and other nanoparticles are formed by a mix of surfactants, rather than by a single type of surfactant.[227] Depending on particular surfactants used, mixed micelle systems can be superior to their single surfactant-based counterparts in different applications.[227–229] The CMC values of mixed micelles are often found to be in between the CMCs of the first and the second surfactant types.[228] Properties of various mixed micelles, such as their size and shape, interaction coefficients, CMCs etc. have been previously investigated.[230–233] Poorly soluble drug solubility into mixed micelle systems has also been investigated. Experimental studies using two-component mixed micelles to solubilize the antitumor drug, doxorubicin, have been conducted and have shown a high efficacy towards tumor growth inhibition.[234–237] In a study conducted by Mehta et al.,[81] Lecithin-Tyloxapol mixed micelles demonstrated high synergy between the two surfactants, as well as high drug encapsulation capabilities. The self-assembly of mixed micelles formed by two surfactants have been investigated in a few studies using atomistic and coarse-grain MD.[238–240] These studies have investigated the self-assembly of mixed micelles composed of different surfactants (CTAB, SDS, glycocholate, etc.). Nevertheless, to this date, there is no computational study on mixed micelles comprised of a mix of a surfactant and its oligomer. Such investigation could answer two important questions, 1) how does the cross-linking between surfactants affect the overall stability of the micelle, and 2) what will be the

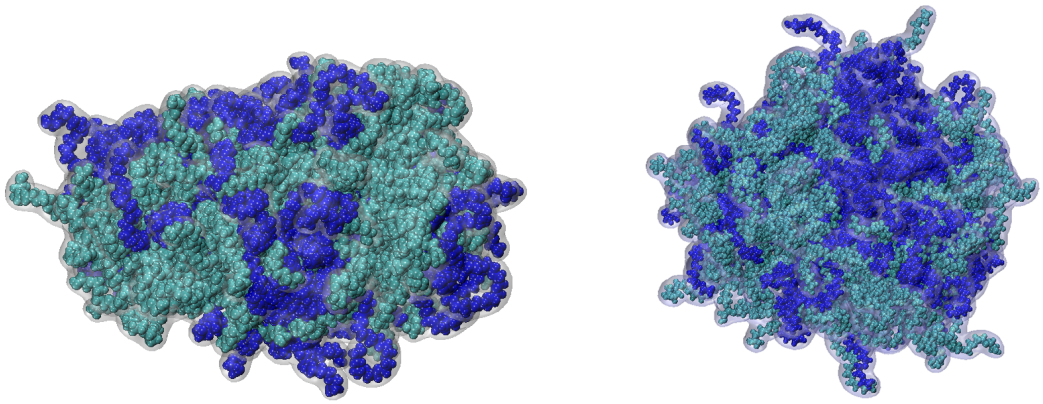


Figure 6.1: Snapshots of Tyloxapol ($m = 3$, left) and Triton X-100, and Tyloxapol ($m = 7$, right) and Triton X-100 mixed micelles. Both snapshots are taken from the 50/50 Tyloxapol-Triton X-100 systems

difference in morphology between single-surfactant-based micelles, surfactant oligomer-based micelles and the mixed micelles formed by both.

In this study, mixed micelles formed by Triton X-100 and Tyloxapol surfactants have been investigated (Figure 6.2). Triton X-100 is comprised of a hydrophilic polyethilene oxide (PEO) headgroup and a 4-(1,1,3,3-tetramethylbutyl)-phenyl hydrophobic tail. Tyloxapol is the oligomeric variant of Triton X-100, with in average of 7 monomers cross-linked via a spacer. This study compares the structural properties of mixed micelles (Figure 6.1) containing different ratios of both surfactants and demonstrates the effect of cross-linking of surfactants on the overall stability and shape of the nanoparticle.

6.2 Methods

6.2.1 Molecular dynamics simulations

In this chapter, Triton X-100 and Tyloxapol mixed micelles have been investigated. All-atom molecular dynamics simulations have been carried out using the GROMACS package[184–186] and the CHARMM36[161–163] force field. Triton X-100 was modelled using CHARMM parameters reported by Yordanova et al.[111] Two types of tyloxapol molecules have been constructed - a trimer

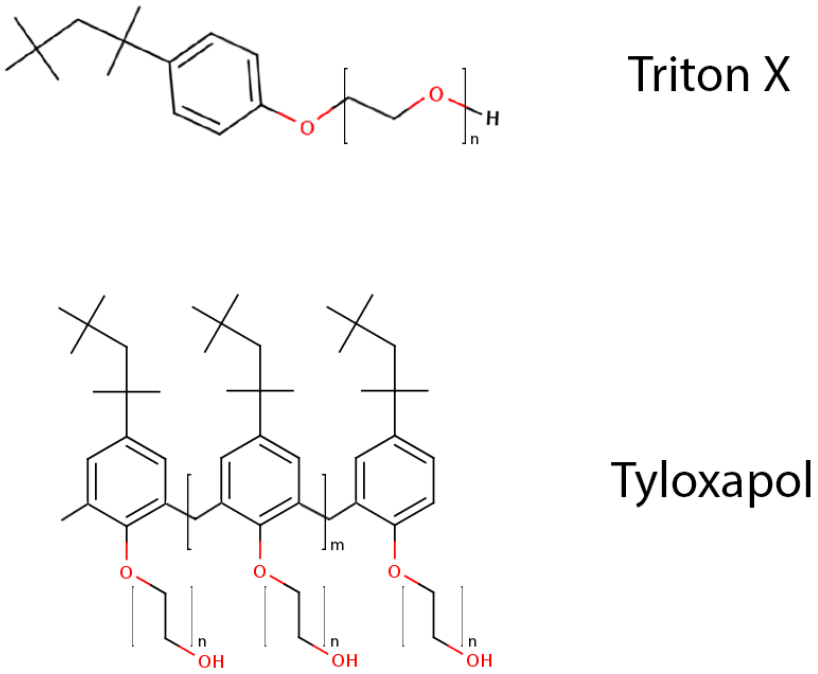


Figure 6.2: Surfactants from Triton X family. For TX100, $n \approx 9.5$, as for TX114, $n \approx 7.5$. $m \approx 7$ for Tyloxapol.

(TYL3) and a heptamer (TYL7) of Triton X-100 (TX100) (Figure 6.2), and were parameterized by the CHARMM36 general force field.[241] The water was modelled using CHARMM36m TIP3 potential.

Overall, eight systems, containing varying quantities of Triton X-100 and Tyloxapol, have been constructed and simulated. In Table 6.1, the number of species in each system is presented. The amounts of both surfactants were chosen such that the total number of monomers was approximately 150. Firstly, surfactants were pre-assembled into a spherical structure using the Packmol software.[183] Then, the micelles were centered in a simulation box with dimensions of 120 Å × 120 Å × 120 Å, after which water was added to fill the box.

The steepest descent algorithm with 5×10^3 steps was applied to minimize each system. Then, the systems were brought to the desired temperature of 303.15 K in a canonical, NVT, ensemble using Nosé-Hoover thermostat, after which the systems were equilibrated in a NPT ensemble to achieve a target

System	Tyl (%)	TX100 (%)	Tyl (N)	TX100 (N)	Water
Tyl3 pure	100	0	50	0	51463
Tyl3-TX100 75	75	25	38	38	51289
Tyl3-TX100 50	50	50	25	75	51237
Tyl3-TX100 25	25	75	13	112	51084
Tyl7 pure	100	0	21	0	51373
Tyl7-TX100 75	75	25	16	38	51158
Tyl7-TX100 50	50	50	11	75	51242
Tyl7-TX100 25	25	75	5	113	51041

Table 6.1: Composition of the eight simulation systems. Percentages of each surfactant and the number of different molecular species.

pressure of 1 bar, coupled to a Nosé-Hoover thermostat and Parrinello-Rahman barostat. The durations for the equilibration simulations were set to 75 ps and 325 ps for the NVT and NPT simulations, respectively. Each system was then simulated for 600 ns using a timestep of 2 fs. The LINCS algorithm[172] was applied to constrain hydrogen-containing bonds. A cut-off of 1.2 nm was used to truncate short-range interactions. Long-range interactions were calculated using the Particle-Mesh Ewald algorithm.

6.2.2 Analysis of trajectories

The analysis of the systems was conducted using tools provided by the GROMACS package as well as in-house written Python scripts.

6.2.3 Basic analysis

To determine the stability of the structure of micelles, the root mean square deviation (RMSD) has been calculated:

$$RMSD = \sqrt{\frac{1}{N}\sum_{i}^{N}(r_i - r_{i0})^2} \tag{6.1}$$

where r_i and r_{i0} are the current and initial positions of i-th particle respectively, and N is the number of particles in the system. The stability has been further monitored by calculating the radius of gyration of micelles:

$$R_g = \sqrt{\frac{\sum_i^N m_i(r_i - r_c)^2}{\sum_i^N m_i}} \tag{6.2}$$

where m_i is the mass of i-th particle, and r_c is the position of the center of the mass of the micelle. The solvent accessible surface area (SASA) was calculated using the FreeSASA library,[242] which implements the Lee and Richards algorithm for accessible surface area calculations.[243]

To determine the shape of the micelle, the inertia tensor has been calculated. In terms of its shape, the micelle can be classified as spherical, oblate, prolate or triaxial. The criteria for a micelle to have a certain shape can be defined in the following manner. Let I_1, I_2 and I_3 be the principal moments of inertia. Then the shape of the micelle can be determined as follows:

1. $I_1 \simeq I_2 \simeq I_3$, micelle is spherical.

2. $I_1 \simeq I_2 > I_3$, micelle is oblate.

3. $I_1 \simeq I_2 < I_3$, micelle is prolate.

4. $I_1 \neq I_2 \neq I_3$, micelle is triaxial.

The moments of inertia can be used further to quantify the shape by computing the ellipticity parameter, ϵ, which is defined as:

$$\epsilon = \frac{I_{max}}{I_{min}} \tag{6.3}$$

where I_{max} and I_{min} are the largest and smallest principal moments of inertia.

6.2.4 Interface definition and density calculation

The interface has been defined using the in-house Python package, AICON, described in Chapter 5. The closest oxygen atoms (O in Figure 6.2) to the hydrophobic tails were selected as the atoms comprising the interface. The densities were computed on the portion of the trajectory when the micelles were already stabilized. The densities of carbon atoms in hydrophilic head,

hydrophobic tail of both Triton X-100 and Tyloxapol were computed. Oxygen atoms in water molecules were selected to calculate the water density.

6.2.5 Volume calculation

The volume of the micelles was calculated using the AICON code. After the interface is defined, the volume estimation has been carried out using Monte Carlo estimation. A million randomly generated points were labeled as inside or outside the interface. The volume, then, was calculated using the following equation:

$$V = \frac{N_{inside}}{N_{total}} d^3 \tag{6.4}$$

where N_{total} and N_{inside} are the total number of points and number of points inside of the interface, respectively. d is the length of the cubic periodic box.

6.2.6 Neighbour analysis

Graph theory has been applied to calculate the number of neighbours and their mutual connectivity. Firstly, the adjacency matrix has been defined. The pairwise distance matrix between centers of masses of surfactants was calculated. Distances shorter than a cut-off ($r_c = 10$Å) are set to 1, whereas the rest is set to 0. Therefore, the elements of the adjacency matrix are defined as:

$$a_{ij} = \begin{cases} 1 & \text{if } r_{ij} \leq r_c \\ 0 & \text{if } r_{ij} > r_c \end{cases} \tag{6.5}$$

where r_{ij} is the distance between particles i and j. Afterwards, for each molecule, types and quantities of neighbours are found, and are used to calculate the ratio $\frac{N_a}{N_{tot}}$ and $\frac{N_b}{N_{tot}}$, where N_a and N_b are the numbers of neighbours of type a and type b of the molecule, respectively, and N_{tot} is the total number of neighbours.

6.3 Results

In this section, the results of the analysis will be summarized. The shape and size of each mixed micelle will be described. Furthermore, the volume estimations alongside with the density calculations will be presented. Finally, the neighbour analysis will be discussed.

6.3.1 Structural properties of micelles

To demonstrate the stability of each system, the corresponding RMSD and radius of gyration have been calculated for each trajectory. Figure 6.3 shows RMSD over time for TYL3-TX100 and TYL7-TX100 systems. Pure Tyloxapol systems reach equilibrium fairly quickly with an average RMSD value of 34.36± 0.01Å and 19.04 ± 0.01Å for TYL3 and TYL7 systems respectively. Systems containing an equal percentage of both TYL and TX100 also maintain their stability over time with average values of 38.86 ± 0.02Å for TYL3 and $21.30 \pm$ 0.02Å for TYL7. The remaining two systems for TYL7 reach a stable state with average RMSD values of 45.03±0.01 for 75% TYL7 system and 47.83±0.01 for 25% TYL7 system. On the other hand, corresponding TYL3 systems greatly fluctuate around average values of 38.10 ± 0.08 and 51.40 ± 0.08 for 75% and 25% TYL3 systems, respectively.

Figure 6.4 shows the radius of gyration for each system. The same general behaviour is observed for each of the systems. The only systems which have significant fluctuations in the R_g are the ones with 25% and 75% of TYL3, as is the case when measuring the RMSD of the micelles.

The SASA of each micelle over time is presented in Figure 6.5. The smallest SASA values were found in the pure TYL3 (47717 ± 24Å^2), and the pure TYL7 micelle (50326 ± 23Å^2). It is worth noting, that pure Tyloxapol micelles have smaller average SASA than pure Triton X-100 micelles reported in Chapter 3. The mixed systems containing TYL7 and TX100 have similar SASA values (54321 ± 25Å^2, 54925 ± 26Å^2, and 54827 ± 27Å^2 in the 75%, 50% and 25% TYL7 systems, respectively). 50% TYL3 micelle has an average SASA value of 53385±26Å^2, which is the lowest of all mixed micelles. The 75%

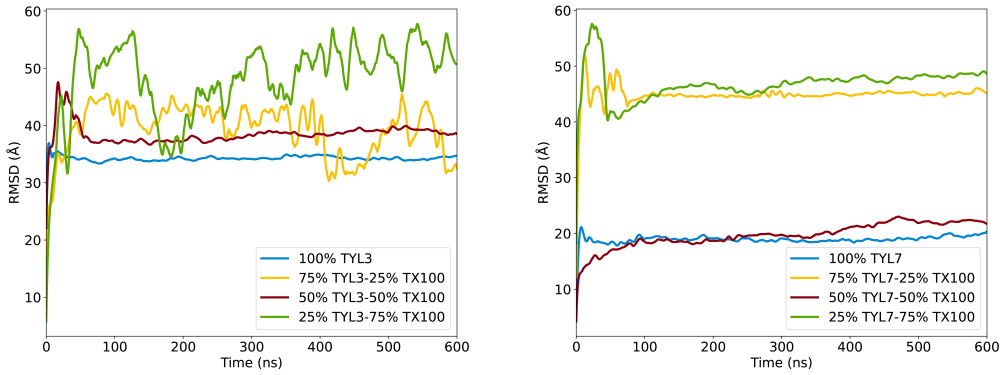


Figure 6.3: RMSD of Tyloxapol trimer (left) and heptamer (right) based micelles as a function of time.

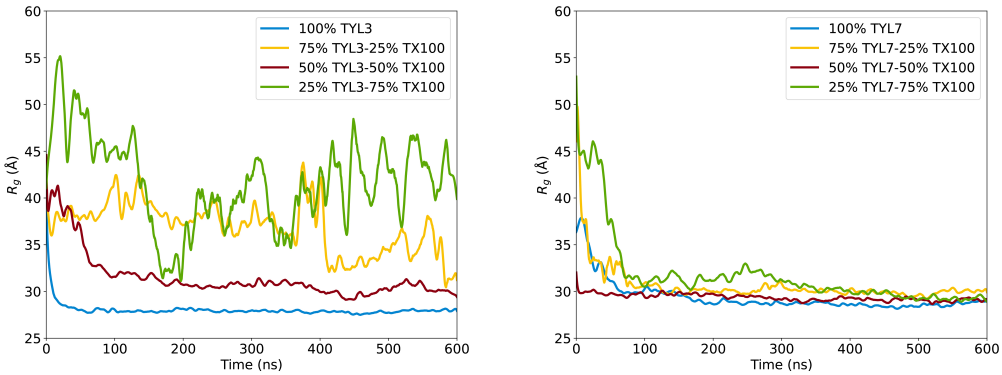


Figure 6.4: Radius of gyration of Tyloxapol trimer (left) and heptamer (right) based micelles as a function of time.

and 25% TYL3 systems exhibit high fluctuations around the average values of $64996 \pm 74\text{Å}^2$ and $57232 \pm 53\text{Å}^2$, respectively.

Furthermore, the volume of each micelle was determined. Figure 6.6 shows the change in the volume of the mixed micelles over time. Pure Tyloxapol micelles have the smallest volume. The 25% and 75% TYL3 micelles have the largest volumes which are approximately two times larger than their TYL7 counterparts. The 50/50 mixture of Triton X-100 and Tyloxapol have approximately equal volumes in both systems. The average values for volume calculations are provided in Table 6.1.

To determine the shape of each micelle, the principal moments of inertia were computed and the ellipticity for each system has been evaluated (Figure

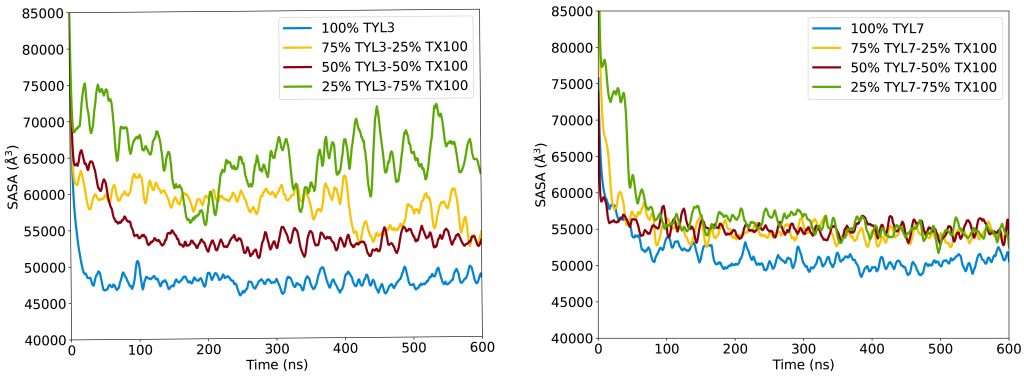


Figure 6.5: Solvent accessible surface area (SASA) of Tyloxapol trimer (left) and heptamer (right) based micelles as a function of time.

6.7). The pure Tyloxapol systems were found to be oblate, and their average ellipticity values were determined to be ~ 1.4. The mixed micelles containing 25% TX100 are triaxial in shape, whereas the rest of the systems are prolate ellipsoids.

6.3.2 Density calculations

The interfaces of the micelles have been constructed and the density profiles of each species throughout the systems have been determined. To define the hydrophobic-hydrophilic interface of micelles, the oxygen atoms that are closest to the hydrophobic tail of TX100 and Tyloxapol have been chosen as vertices for the interface. To calculate the densities of the hydrophobic tails and the hydrophilic heads of the surfactants, only their carbon atoms have been considered, whereas for water only the oxygen atoms were considered. Figure 6.8

System	SASA (Å^2)	Ellipticity	Volume (nm^3)
Tyl3 pure	47717 ± 24	1.370 ± 0.001	256.9 ± 0.8
Tyl3-TX100 75	57232 ± 53	2.609 ± 0.009	422.7 ± 7.1
Tyl3-TX100 50	53385 ± 26	1.902 ± 0.004	295.3 ± 1.9
Tyl3-TX100 25	64996 ± 74	2.099 ± 0.009	474.2 ± 11.2
Tyl7 pure	50326 ± 23	1.438 ± 0.001	294.7 ± 1.0
Tyl7-TX100 75	54321 ± 25	1.682 ± 0.001	310.0 ± 2.7
Tyl7-TX100 50	54925 ± 26	1.453 ± 0.001	293.5 ± 1.0
Tyl7-TX100 25	54827 ± 27	1.496 ± 0.003	302.3 ± 1.3

Table 6.2: Average SASA, ellipticity and volume values for each system.

shows the density plots for the pure Tyloxapol systems. As discussed earlier, $r = 0$ is at the surface of the interface. As the interface was defined as the boundary between hydrophobic tails and hyrophilic heads, it can be observed, that the density of carbon atoms in the surfactant tails are quickly reaching 0 as the distance increases. Furthermore, the carbon atoms in hydrophilic head have approximately have a density half of that for the carbon atoms in the hydrophobic tails. The water density in the bulk solution is on average 0.033Å^{-3}, which is in accordance with the value obtained with other methods.[170,244,245] When getting closer to the interface, the water density decreases reaching an average value of 0.004Å^{-3} for TYL3 and a 0.007Å^{-3} for TYL7 systems respectively.

For the mixed systems, the densities are shown in Figure 6.9. For every system, the peak density of hydrophilic heads are approximately two times smaller than the density of hydrophobic head, as the heads are more mobile and are found to be spread outside as well as inside of the micelle. Furthermore, water can be found inside of each micelle. Furthermore, in both of the mixed systems containing equal percentages of Tyloxapol and Triton X-100 (Figure 6.9 c), d)), a larger density of Tyloxapol tails than Triton X-100 tails is observed. In figure 6.9 d), the hydrophilic heads of both TYL3 and TX100 have a similar density profiles, whereas in TYL7 micelle, TYL7 head den-

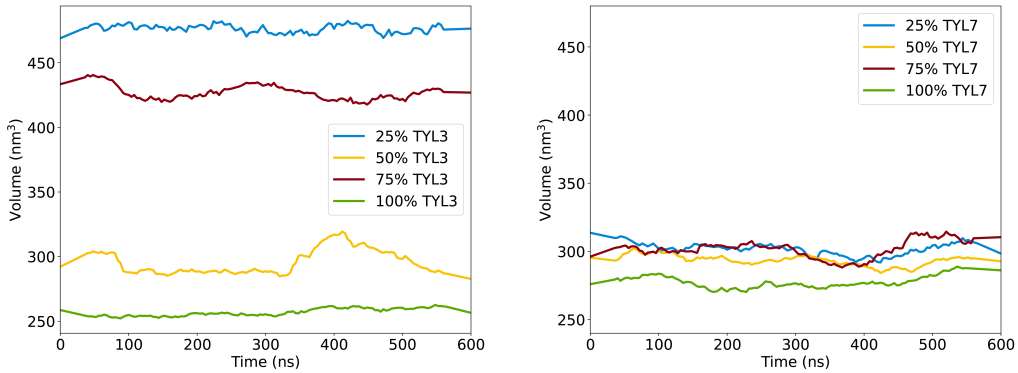


Figure 6.6: Volumes of TYL3 (left) and TYL7 (right) micelles as a function of time.

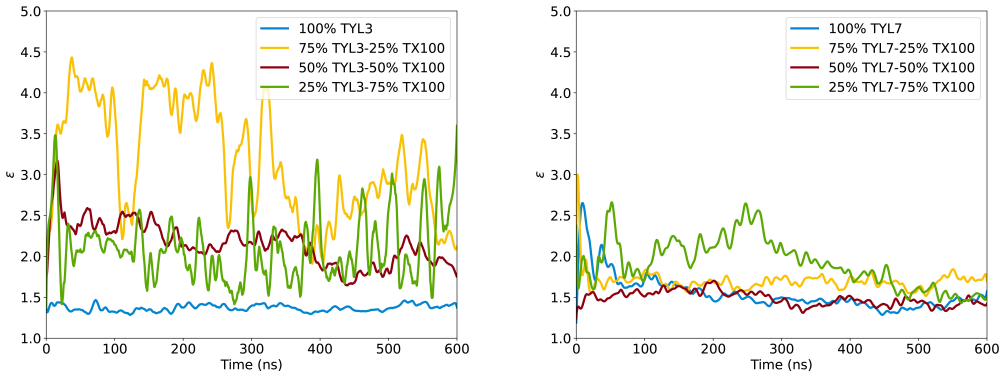


Figure 6.7: Ellipticity of Tyloxapol trimer (left) and heptamer (right) based micelles as a function of time.

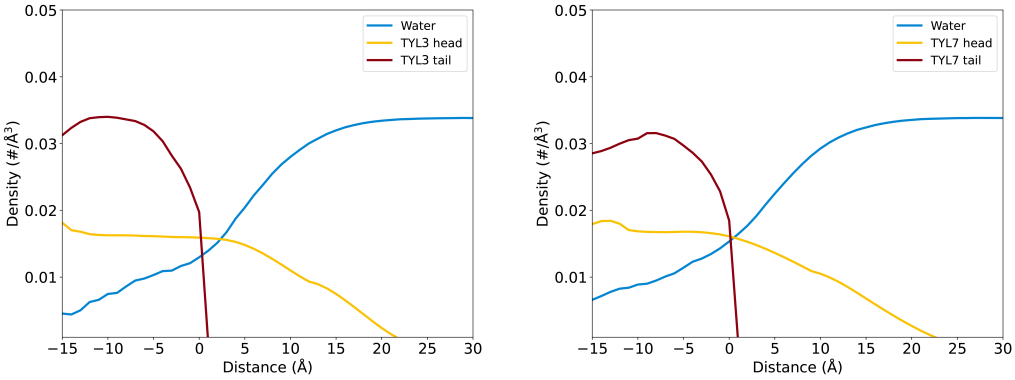


Figure 6.8: Densities of water and carbon atoms in hydrophibic tail and hydrophilic head in pure TYL3 system (left) and pure TYL7 system (right).

sity is larger than TX100 head density inside of the interface (Figure 6.9 c)). Finally, in systems containing the least amount of Tyloxapol, the density of Triton X-100 hydrophobic and hydrophilic parts is larger than the corresponding densities of Tyloxapol. Larger density values of the entrapped water close to the interface partly arise due to the limitations of the interface definition discussed in the "Future work" section of the previous chapter.

6.3.3 Neighbour analysis

In order to assess the environment of each type of surfactants, a neighbour analysis has been conducted. Figure 6.10 shows the distribution of TYL3 percentage around TX100 molecules throughout the trajectory. The average

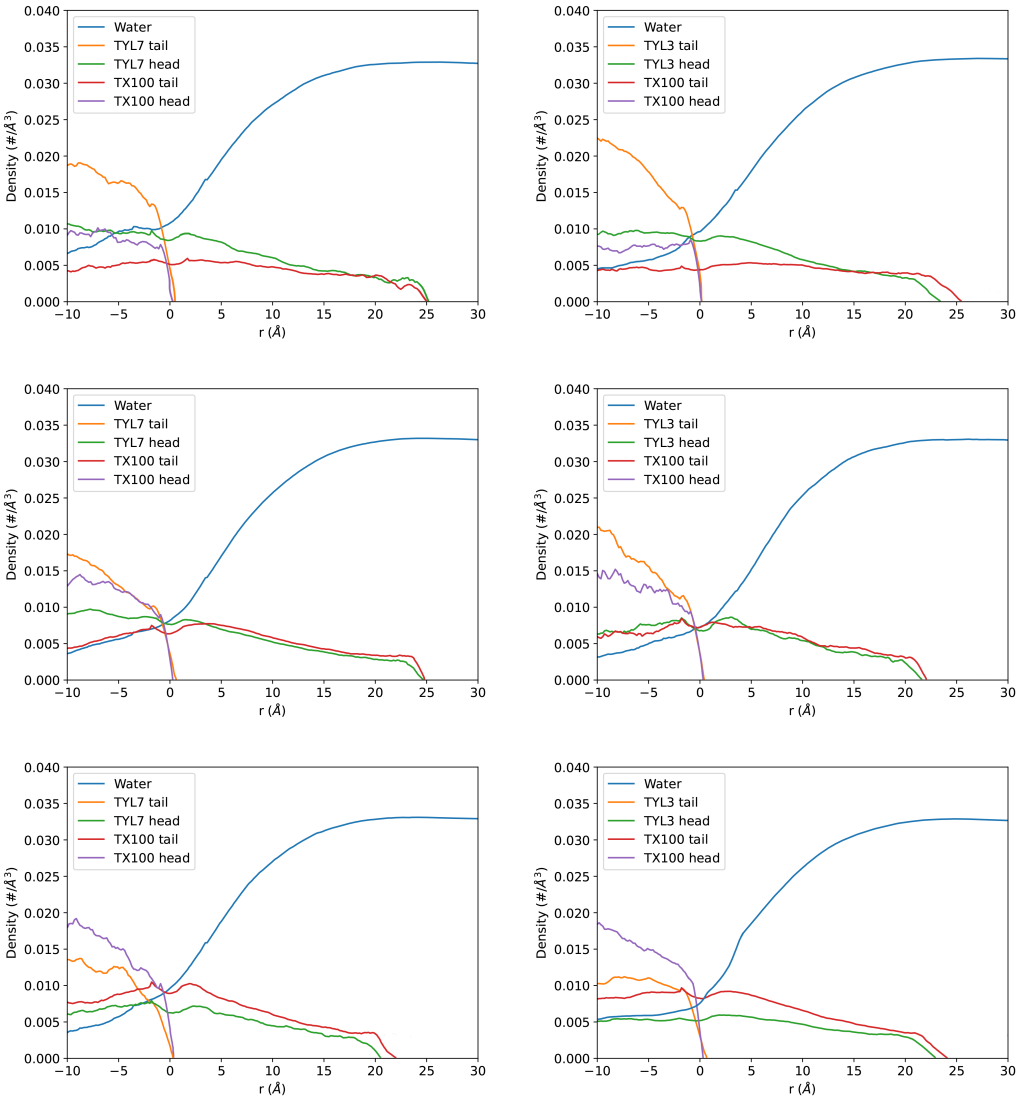


Figure 6.9: Density profiles for Tyloxapol-Triton X-100 mixed micelles.

values for the three TYL3-TX100 systems are 0.09 (25% TYL3), 0.18 (50% TYL3), and 0.48 (75% TYL3). These values are fairly close to the percentage of Tyloxapol molecules inside of the micelle. For the system with 25% TYL3, TYL3 percentage inside of the micelle is ∼0.1. For 50% TYL3 system, the corresponding value is 0.25, and for the 75% system it is 0.5. The similarity between these percentages and neighbour percentages indicate that there is no selectivity between Tyloxapol trimers and Triton X-100 molecules.

Similarly, neighbour analysis for TYL7-TX100 system is depicted in Figure 6.11. For the first two systems, the obtained values for the ratio of the

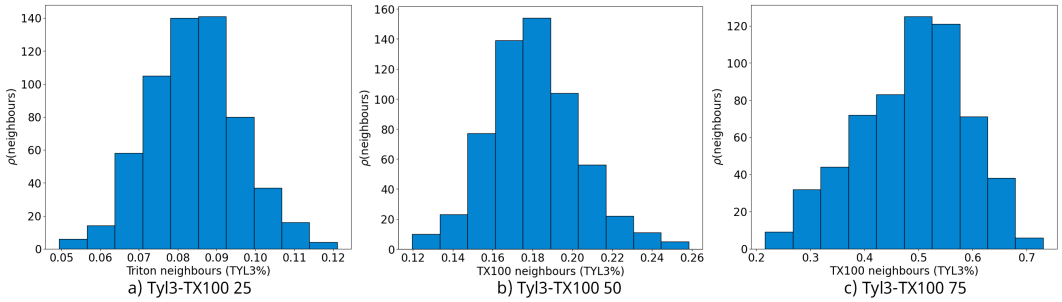


Figure 6.10: Percentage of Tyloxapol trimers around TX100 surfactants.

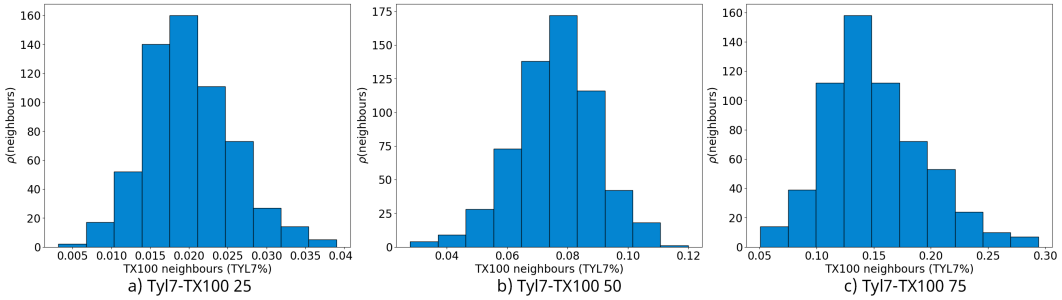


Figure 6.11: Percentage of Tyloxapol heptamers around TX100 surfactants.

neighbouring Tyloxapol heptamers around the TX100 molecules are 0.03 and 0.11 for 25% TYL7 and 50% TYL7 systems respectively. The corresponding ratios of TYL7 molecules inside of the mixed micelles are 0.04 (25% TYL7) and 0.13 (50% TYL7). For the 75% TYL7 system, the neighbouring and the actual ratios are 0.2 and 0.3, respectively. This difference, however, does not necessarily indicate to a selectivity. Due to the size and large number of Tyloxapol heptamers, the neighbourhood of each molecule did not change significantly from the beginning of the simulation (neighbours over time for 75% TYL3 and 75% TYL7 systems shown in Appendix D).

6.3.4 Conclusions

In this chapter, the structures of micelles formed by Tyloxapol and Triton X-100 surfactants have been investigated. The pure Tyloxapol micelles have quickly stabilized, and have shown the smallest surface area out of all the systems, with the heptamer showing slightly higher average SASA than its trimeric counterpart. Furthermore, pure micelles were the only oblate ellipsoids, possessing small ellipticity values. Additionally, the density calculations

show a certain amount of water inside of the core of the micelles. Analysis of the local environments of the surfactants has been conducted using graphs. It has shown that the percentage of Tyloxapol surrounding Triton X-100 molecules is close to the percentage of Tyloxapol in entire micelles, which would indicate that there is no selectivity between the two types of surfactants. This is expected, since both surfactants are similar in structure, with one being the oligomeric version of the other. However, this new approach can be generalized to be applied to other two-component mixed systems in order to quantify the selectivity of one component towards the other and assess the local chemical environments of different species.

6.3.5 Future work

A complete analysis of the 25% and 75% TYL3 systems will be performed in order to gain more insight into what causes them to be less stable than the other systems. After modifying the code to define a concave interface, the density calculations will be repeated, and will provide more accurate density profiles.

Mixed surfactant micelles have different properties, e.g. structural, wetting, solubilizing, than their single-surfactant counterparts. They can enhance solubilizion of certain poorly-soluble drugs. In our previous studies, we have investigated drug solubilization capabilities of micelles formed by Triton X surfactants. A further research to study drug encapsulation by the mixed micelles of Triton X-100 and Tyloxapol will provide an interesting insight into the dependence of solubilization from the composition of the nanoparticles. The same non-steroidal anti-inflammatory drugs, ibuprofen and indomethacin will be used in the next series of simulations. Additionally, a detailed analysis will be conducted to describe the solubilization and morphological changes of the mixed micelles induced by the drug molecules.

Chapter 7

Conclusions

The research summarised in this thesis has provided an in-depth understanding of the molecular scale mechanisms which govern the morphology and drug solubilization capabilities of surfactant based micelles. In Chapter 3, all-atom molecular dynamics simulations were used to investigate micelles formed by non-ionic surfactant Triton X-100. These surfactants contain an aromatic and a methyl group in their hydrophobic tail, and polyethylene glycol (PEG) chain comprised of 10 units in their hydrophilic head. In water, Triton X-100 formed micelles that were prolate ellipsoids. In a solution containing non-steroidal anti-inflammatory drugs (NSAIDs), ibuprofen and indomethacin, these micelles became more elongated forming rod-like structures. The ibuprofen-loaded micelle at its full capacity stays stable with an aggregation number of 150. The indomethacin-loaded micelle, however, splits into two daughter micelles that remain stable throughout the simulation. In addition, Chapter 4 has investigated the effect of the headgroup length of the surfactant on the potential of its micelles as drug carriers. Triton X-114, another non-ionic surfactant closely related to Triton X-100, and having a hydrophilic headgroup with 8 ethylene glycol units, has been studied. Pure micelles formed by Triton X-114 were triaxial in shape and slightly smaller in comparison with the Triton X-100 micelles. Furthermore, ibuprofen and indomethacin have promoted structural changes in the micelles, rendering them elongated. While ibuprofen-loaded micelles remained stable similar to Triton X-100 micelles,

continuous indomethacin encapsulation resulted in splitting of the micelle, a phenomenon reported in Chapter 3. This has been explained by the extensive interactions between indomethacin molecules, that cause them to aggregate inside the core of Triton X-100 and Triton X-114 micelles and destabilize them. In comparison, the interactions between ibuprofen molecules were weaker, and did not have any destabilizing effect on the micelles. The detailed analysis of these systems scrutinizes the structure, shape, dimensions and hydration of the micelles and inter-molecular interactions. These findings shed light on the interactions of different components in drug delivery formulations and can act as a guideline for future drug design.

Chapter 5 was focused on a Python package developed to construct interfaces between different phases, which allows one to describe various important properties such as density profiles of different species in the system, volume enclosed by the interface, etc. The need for such a tool arose from the fact, that, to my best knowledge, no publicly available program or a script has been able to correctly describe asymmetrical and non-spherical interfaces. As the systems that are investigated in this project were often elongated, rod-like structures, this tool was a necessity for an accurate description of the hyrophobic-hydrophilic interface. Furthermore, the chapter has provided a protocol to make any computationally demanding scientific script or software, written in a relatively slow language such as Python, dramatically faster by employing easy-to-implement compilation and parallelization.

Finally, in Chapter 6, micelles formed by two types of surfactants were studied. Triton X-100 and Tyloxapol were used to form mixed micelles. Tyloxapol is an oligomeric surfactant based on Triton X-100, in which an average of 7 Triton X-100 are covalently connected. Two versions of Tyloxapol were used, a trimer (Tyloxapol 3) and a heptamer (Tyloxapol 7). This work touched on two important questions. Firstly, mixed micelles are known for exhibiting properties different from their single-surfactant-based counterparts, and by fine-tuning the composition, they can be adjusted for the desired appli-

cation. Secondly, this work has investigated the effect of crosslinking between the components of the micelle on latter's stability, shape and structure, a topic which to my best knowledge was not investigated before in molecular dynamics. Pure Tyloxapol micelles were oblate ellipsoids and were more compact than pure Triton X-100 micelles investigated in Chapter 3. With the increasing percentage of Triton X-100, the micelles became larger, adopting either prolate or triaxial shapes. The exception being the micelle containing 50% of Tyloxapol 7, which was oblate and nearly as small as the pure Tyloxapol micelle. Additionally, an approach of determining the local environment of each type of molecule based on graph theory was introduced. In mixed Triton X-100 and Tyloxapol micelles, this approach has been used to describe the selectivity of each surfactant towards itself, or the other type. However, the surfactants has shown little or no selectivity.

Chapter 8

Future work

A summary of the future work will be presented in this chapter.

8.1 Wrapping up and future prospects

As an extension to chapter 3 of this thesis, the solubilization of other poorly-soluble non-steroidal anti-inflammatory drugs (NSAID), that have intermediary molar masses to ibuprofen and indomethacin (e.g. diclofenac, naproxen) in Triton X-100 micelles may be useful to investigate. This project will provide insight on the dependence of the mass and hydrophobicity of the drugs that need solubilizing on the solubilization process itself.

As discussed in chapter 5, there are a few improvements that need to be implemented for the code. First and foremost, the interface definition will be refactored to use a more concave definition for the hull. Additionally, unit tests will be implemented to assure the integrity and proper functionality of the code. Furthermore, the code needs to be cleaned and prepared in order to deploy it in an online repository (e.g. conda-forge, PyPI), to make the code public and usable by others.

Due to time constraints, the mixed micelle investigation has not been concluded. The stability of the two micelles with containing 25% and 75% of the trimer surfactant, need to be further investigated as they have shown large fluctuations in their RMSD, radius of gyration, etc. The amount of water inside of the hydrophobic core in these systems needs to be determined, as

excess water inside of the core can destabilize the micelle. Finally, poorly-soluble drug solubilization inside of the mixed micelles will be investigated.

8.2 G-quadruplex DNA selective drugs

A G-quadruplex is a non-canonical conformation of DNA. It can be formed in a single DNA strand or in multiple strands that are rich in guanine and can be stablilized with a cation.[246,247] The existence of these structures has been shown and investigated extensively *in vitro*, although for a long time there has been a postulation that suggests that these structures may also form and play a regulatory role *in vivo*.[248,249] One of the reasons is that guanine-rich segments exist in some crucial functional parts, such as promoters of some genes and telomeres, of the genome of many organisms. Interestingly, guanine-rich sequences has been found in the promoter regions of certain proto-oncogenes, e.g. c-kit, c-MYC, KRAS.[250–252] Regulation of G-quadruplex structures in these regions may inhibit the transcription of the gene. Therefore, these regions gained popularity as potential targets for anti-cancer pharmaceuticals.[253–255]

As a side-project in the framework of this Ph.D. research, G-quadruplex-drug interactions have been investigated in all-atom molecular dynamic simulations. In collaboration with Professor Miraz Rahman from School of Cancer & Pharmaceutical Sciences, King's College London, three novel drugs have been investigated and their potential as a KRAS gene inhibitor has been partially evaluated. As a part of my future work, this project will be resumed and a complete analysis will be conducted in order to assess the selectivity of the drugs towards G-quadruplexes, rather than towards a helical DNA.

I wish there were a far off corner,
A child's innocent sleep -
Humanity living happily
And peacefully in a dream.

Hovhannes Tumanyan

Appendix A

Supporting information for "Impact of drug aggregation on the structural and dynamic properties of Triton X-100 micelles"

ıic Supplementary Material (ESI) for Nanoscale.
rnal is © The Royal Society of Chemistry 2022

Supporting information for "Impact of drug aggregation on the structural and dynamic properties of Triton X-100 micelles"

Hrachya Ishkhanyan,[†] Natasha H. Rhys,[†] David J. Barlow,[‡] M. Jayne Lawrence,[*,‡] and Christian D. Lorenz[*,†]

†*Biological & Soft Matter Research Group, Department of Physics, Faculty of Natural, Mathematical & Engineering Sciences, King's College London, London, United Kingdom*

‡*Division of Pharmacy and Optometry, School of Health Sciences, Faculty of Biology, Medicine and Health, University of Manchester, Stopford Building, Oxford Road, Manchester, United Kingdom*

E-mail: jayne.lawrence@manchester.ac.uk; chris.lorenz@kcl.ac.uk

Starting Configurations of the Systems

Packmol input file used to generate the starting configurations is shown below. The same code, with different files for ibuprofen and indomethacin, was used for both systems:

```
tolerance 2.0
output tx100_ibup_pre.pdb
filetype pdb

structure ibup_ini.pdb
   number 100
   inside box -60.5 -60.5 -60.5 60.5 60.5 60.5
   outside sphere 0. 0. 0. 45.
end structure

structure triton_x100_n_10.pdb
  number 100
  atoms 70
    inside sphere 0. 0. 0. 10.
  end atoms
  atoms 46
    outside sphere 0. 0. 0. 25.
  end atoms
end structure
```

Further analysis

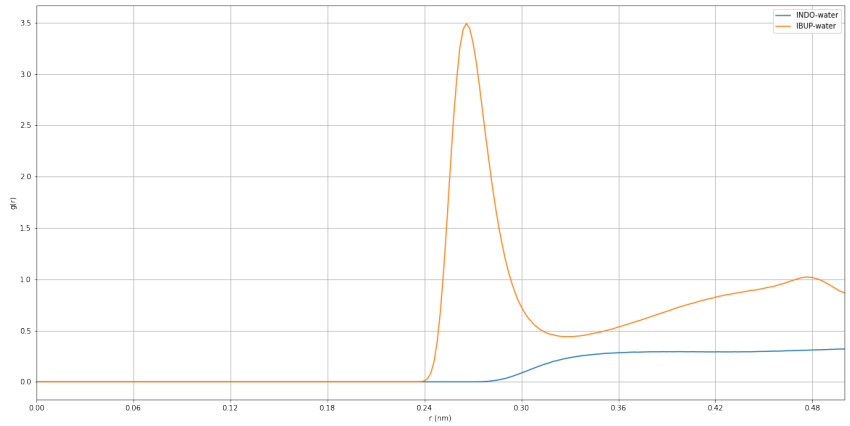
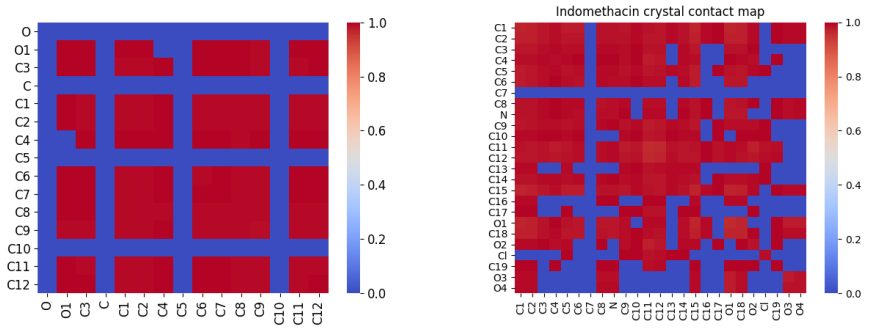


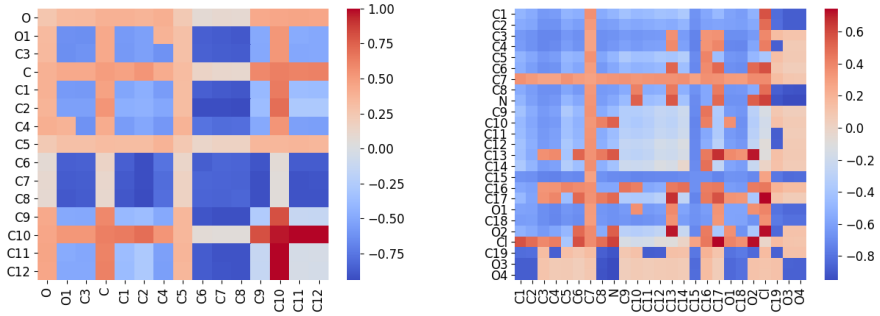
Figure S1: RDF's of oxygen in water with O and O2 in ibuprofen and Cl and N in indomethacin as reference atoms.

Contact Maps of Drugs in a Crystalline Structure



(a) (b)

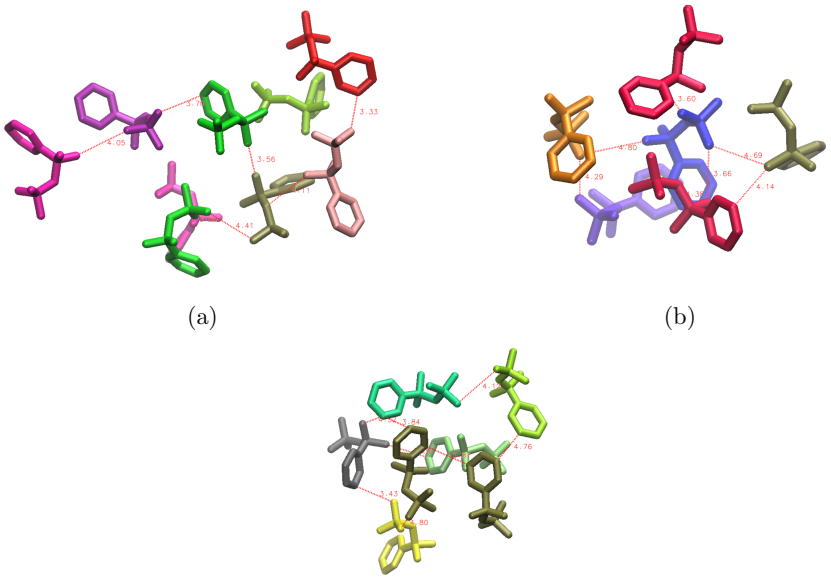
Figure S2: Contact heat maps of the drug - drug interactions for (a) ibuprofen and (b) indomethacin in their crystalline structure.



(a) (b)

Figure S3: Difference in the contact maps of drug-drug interactions within the micelle and in their crystalline structure for (a) ibuprofen and (b) indomethacin. Positive values represent contacts which are more common in the structure taken by the drugs in the core of the micelle, while negative values represent contacts which are more common in the crystalline structure of the drug.

Interaction between Triton X-100 hydrophobic tails

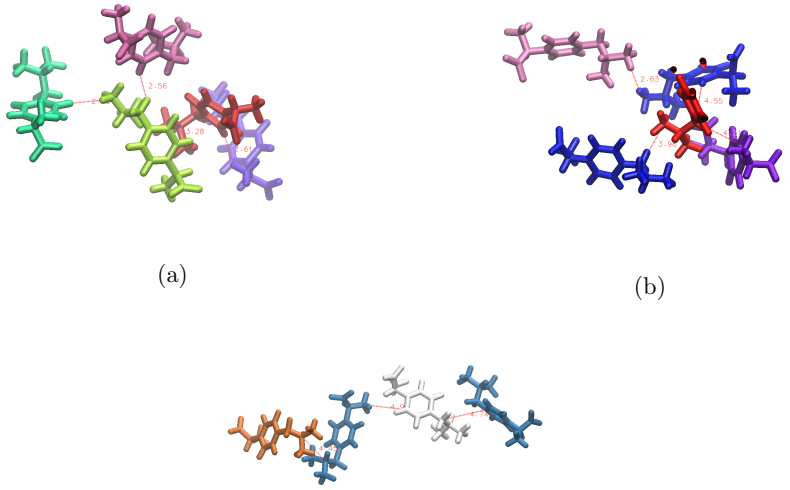


(a) (b)

(c)

Figure S4: Snapshots showing the representative interactions between the hydrophobic tails of the Triton X-100 surfactants within the micelles. Generally the surfactant molecules interact via a mixture of hydrophobic contacts between the benzene ring and the methyl groups in their hydrophobic tails. The different colors in (a) - (c) represent different molecules.

Interaction between encapsulated ibuprofen molecules



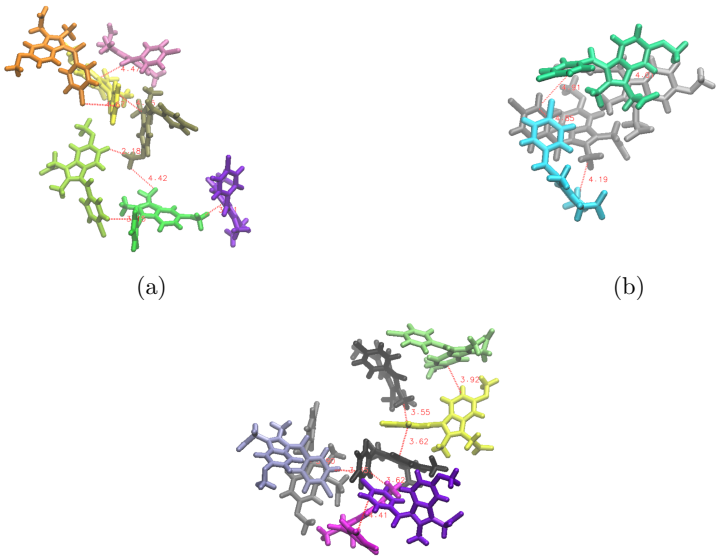
(a)

(b)

(c)

Figure S5: Snapshots showing the representative interactions between neighbouring ibuprofen molecules within the core of a Triton X-100 micelle. The different colors in (a) - (c) represent different molecules.

Interaction between encapsulated indomethacin molecules

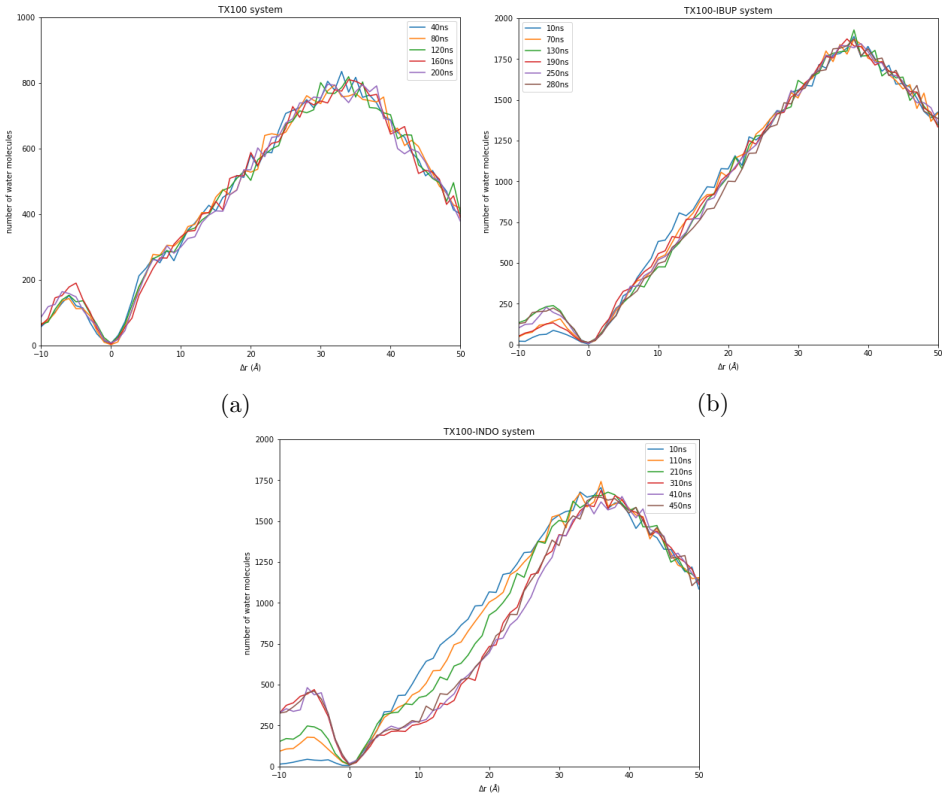


(a) (b)

(c)

Figure S6: Snapshots showing the representative interactions between neighbouring indomethacin molecules within the core of a Triton X-100 micelle. The different colors in (a) - (c) represent different molecules.

Penetration of water into the core of the micelles



(a) (b)

(c)

Figure S7: Plots of the amount of water as a function of Δr at various times during the production simulations of the (a) Triton X-100 micelle, (b) the ibuprofen-loaded Triton X-100 micelle and (c) the indomethacin-loaded Triton X-100 micelle.

Appendix B

Supporting information for "NSAID Solubilisation Promotes Morphological Transitions in Triton X-114 Surfactant Micelles"

Supporting information for "NSAID Solubilisation Promotes Morphological Transitions in Triton X-114 Surfactant Micelles"

Hrachya Ishkhanyan,[†] Robert M. Ziolek,[†] David J. Barlow ,[‡] M. Jayne Lawrence,[‡] Armen H. Poghosyan,[*,¶] and Christian D. Lorenz[*,†]

†*Biological Physics and Soft Matter Group, Department of Physics, King's College London, London WC2R 2LS, United Kingdom*

‡*Division of Pharmacy and Optometry, School of Health Sciences, Faculty of Biology, Medicine and Health, University of Manchester, Stopford Building, Oxford Road, Manchester M13 9PG, United Kingdom*

¶*International Scientific-Educational Center of National Academy of Sciences, M. Baghramyan Ave. 24d, 0019 Yerevan, Armenia*

E-mail: sicnas@sci.am; chris.lorenz@kcl.ac.uk

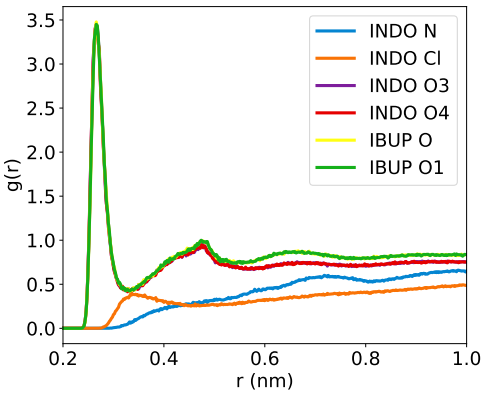


Figure S1: **RDFs for water.** Reference atoms are oxygens in carboxyl groups of the drugs and nitrogen and chlorine in indomethacin.

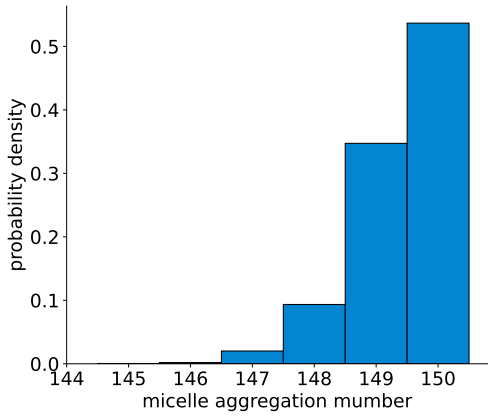


Figure S2: **Aggregation number of the TX-114 micelle**

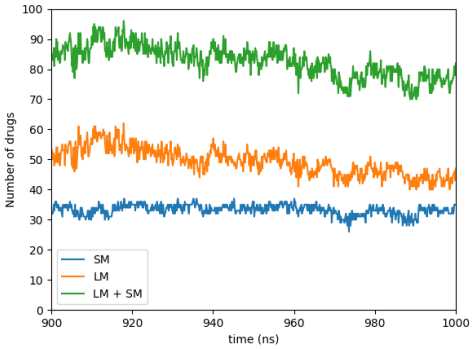
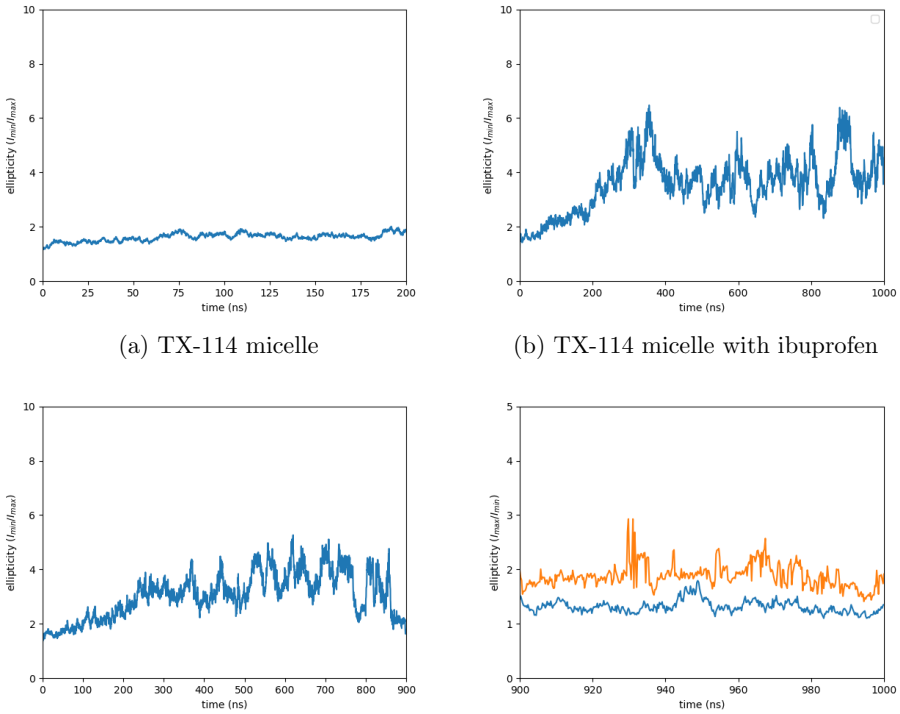


Figure S3: **Indomethacin encapsulation in daughter TX-114 micelles**

Ellipticity



(a) TX-114 micelle

(b) TX-114 micelle with ibuprofen

(c) Parent micelle with indomethacin

(d) Daughter micelles with indomethacin

Figure S4: **Ellipticity of the micelles.** The ellipticity is plotted as a function of time for the (a) pure Triton X-114 micelle, (b) Triton X-114 micelle loaded with ibuprofen, (c) the parent Triton X-114 micelle loaded with indomethacin and (d) the daughter Triton X-114 micelles (LM - larger micelle, SM - smaller micelle) loaded with indomethacin.

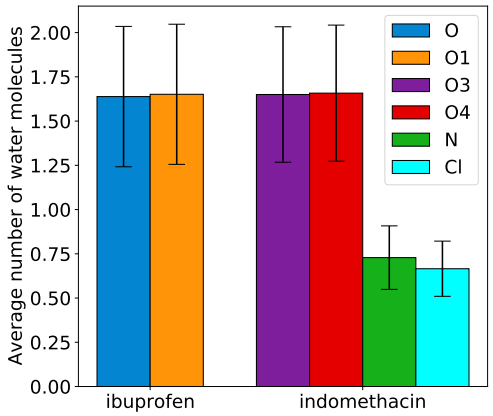
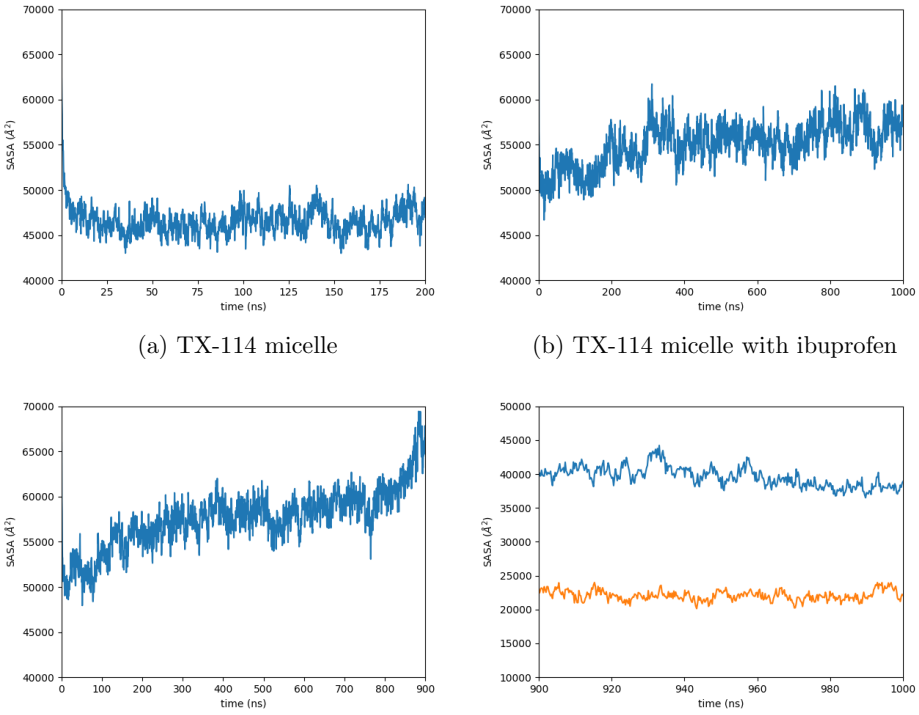


Figure S5: **Hydration of drugs.** Bar plot showing the hydration of oxygens in the carboxyl groups of indomethacin and ibuprofen and chlorine and nitrogen of indomethacin.

SASA



(a) TX-114 micelle

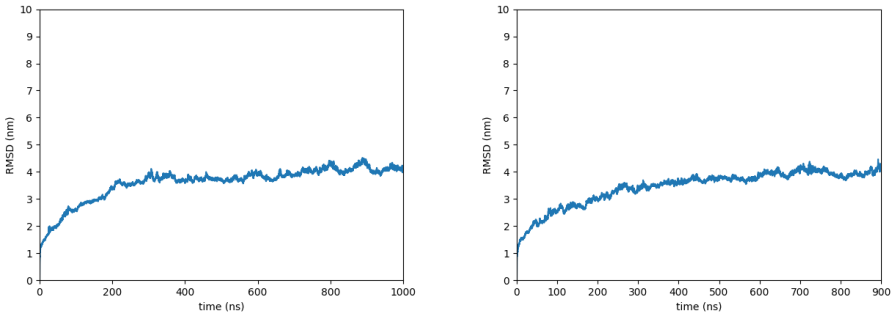
(b) TX-114 micelle with ibuprofen

(c) Parent micelle with indomethacin

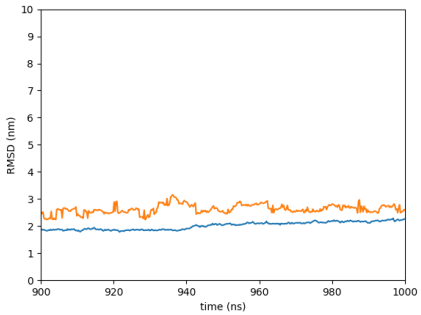
(d) Daughter micelles with indomethacin

Figure S6: **Solvent assessible surface area (SASA) of micelles.** Plots of the SASA as a function of time for the (a) pure Triton X-114 micelle, (b) Triton X-114 micelle loaded with ibuprofen, (c) the parent Triton X-114 micelle loaded with indomethacin and (d) the daughter Triton X-114 micelles (LM - larger micelle, SM - smaller micelle) loaded with indomethacin.

RMSD



(a) (b)



(c)

Figure S7: **Root-Mean-Square Deviation (RMSD) of the micelles.** Figures (a) shows the RMSD of the micelle in the presence of ibuprofen. In figures (b) RMSD of the indomethacin loaded micelle slowly increases until it splits into two. Figure (c) shows the RMSD of the resulting big micelle and small micelle in orange and blue respectively.

Radius of Gyration

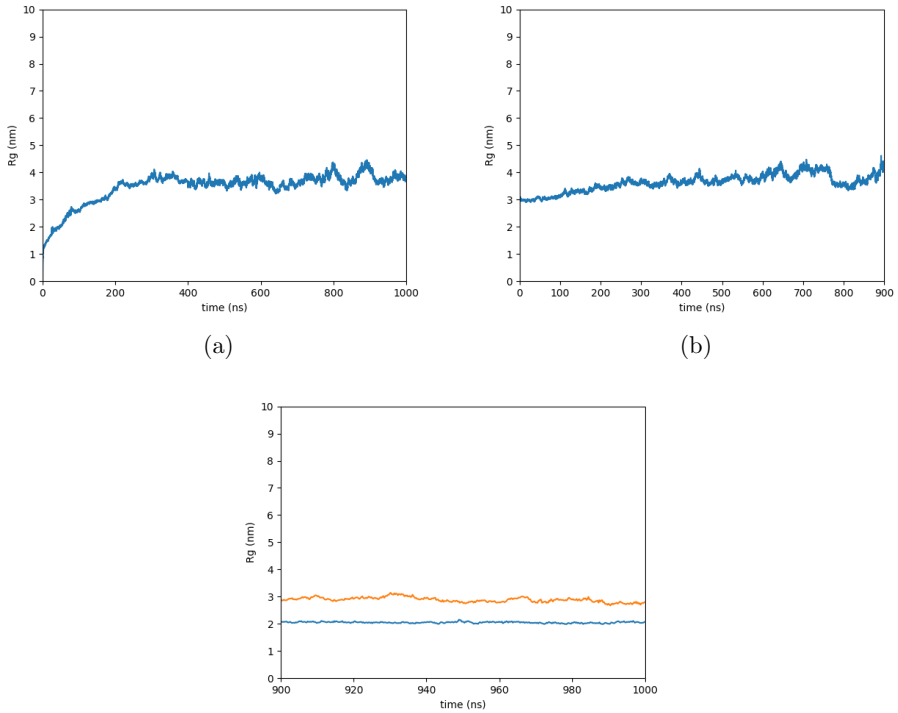


Figure S8: **Radius of gyration of the micelles.** Figures (a) shows the radius of gyration of the micelle in the presence of ibuprofen. In figures (b) the radius of gyration of the indomethacin loaded micelle slowly increases. At 750ns timestep, the value drops and starts to increase at a larger rate until the micelle is split into two. Figure (c) shows the radius of gyration of the resulting big micelle and small micelle in orange and blue respectively.

Evolution of Contacts

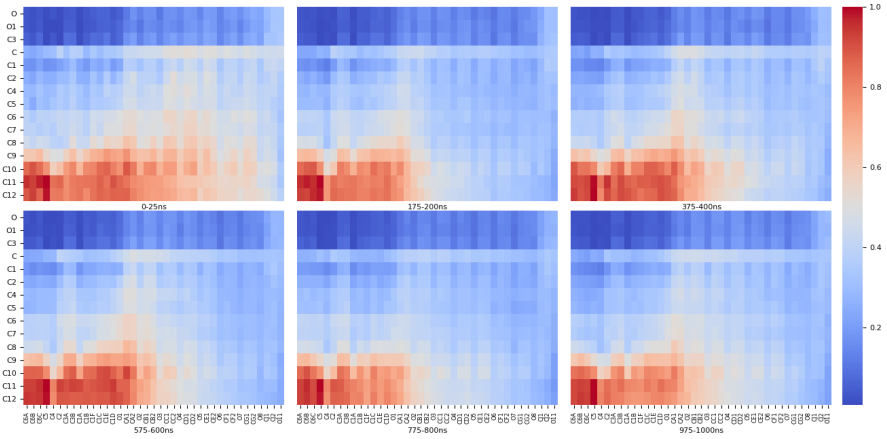


Figure S9: **Evolution of contacts between ibuprofen and TX-114**

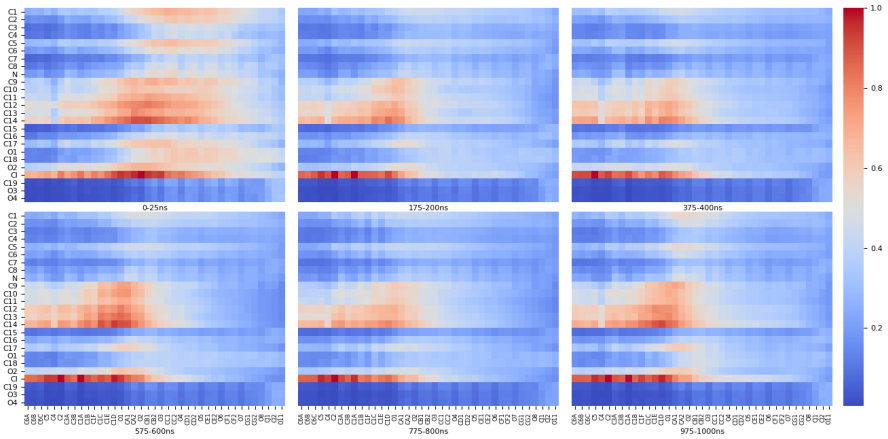


Figure S10: **Evolution of contacts between indomethacin and TX-114**

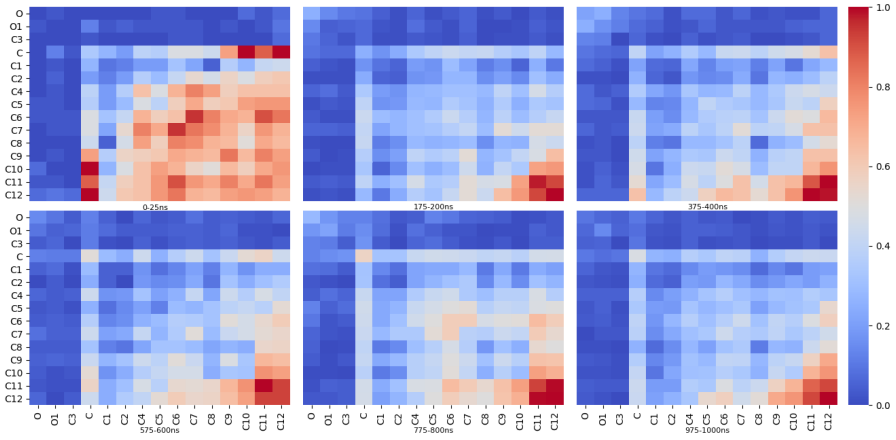


Figure S11: **Evolution of contacts between ibuprofen with itself**

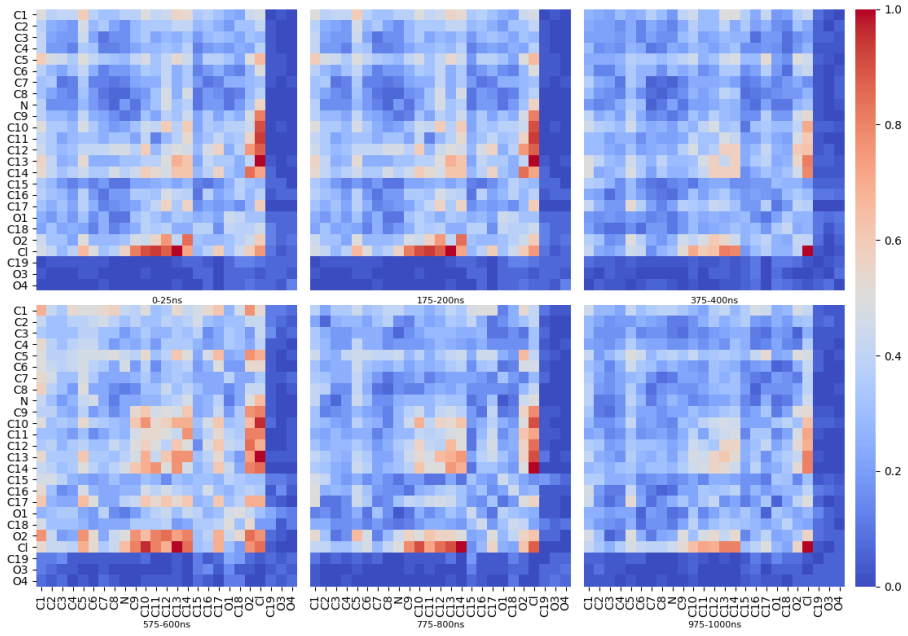
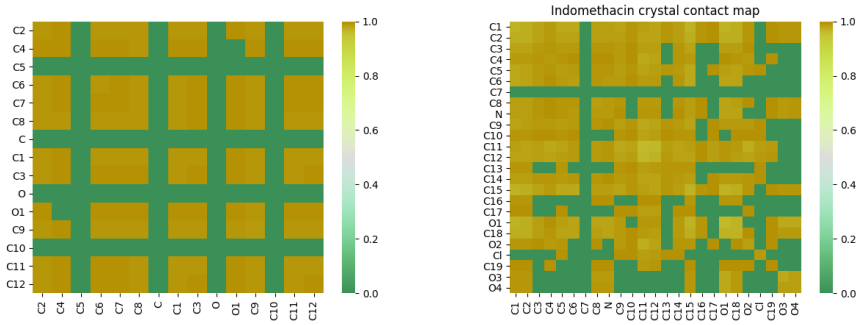


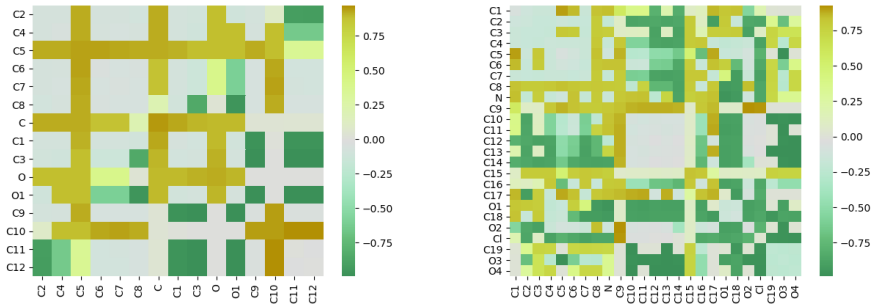
Figure S12: **Evolution of contacts between indomethacin with itself**

Contact Maps of Drugs in a Crystalline Structure



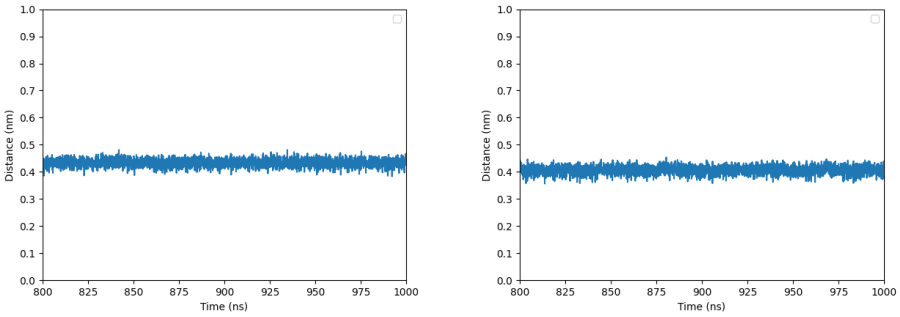
(a) (b)

Figure S13: **Contact heat maps of the drug - drug interactions** for (a) ibuprofen and (b) indomethacin in their crystalline structure.



(a) (b)

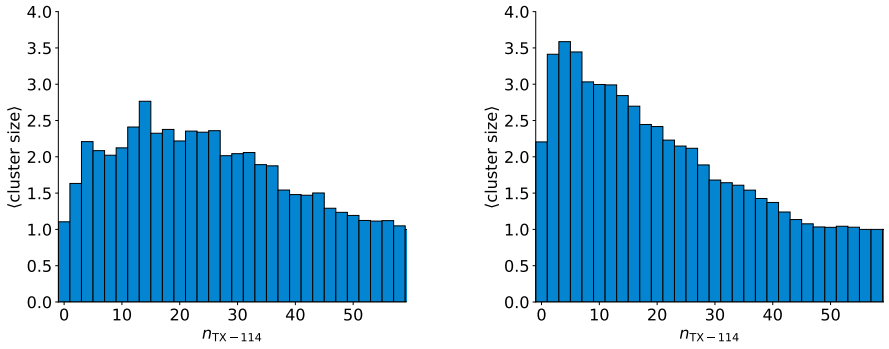
Figure S14: **Difference in the contact maps of drug-drug interactions within the micelle and in their crystalline structure** for (a) ibuprofen and (b) indomethacin. Positive values represent contacts which are more common in the structure taken by the drugs in the core of the micelle, while negative values represent contacts which are more common in the crystalline structure of the drug.



(a) (b)

Figure S15: **The distance between the closest atoms in the drug-micelle system.** Figure (a) shows the distance between C5 and C11 of ibuprofen and TX-114 respectively through last 200ns of the trajectory. Figure (b) shows the distance between the Cl of indomethacin and C5 of the surfactant through the same duration of the simulation.

Effect of solubilisation on drug clustering



(a) (b)

Figure S16: **Effect of degree of solubilisation on drug clustering.** Effect of the number of TX-114 non-hydrogen atoms in contact with each drug molecule ($n_{\mathrm{TX-114}}$) on the average cluster size of ibuprofen (a) and indomethacin (b).

Appendix C

Analysing code performance in "AICON: A Python package to analyze aspherical nanoparticles"

To assess the performance of a code it needs to be profiled. The Python standard library provides two great tools for profiling called **cProfile** and **profile**. Below is an example of profiling a simple function that sorts an array in descending order (Listing C.1). **run()** function from **cProfile** library takes a command that needs to be executed and shows the execution time of the different functions that were called. The output of **run()** function is shown in the listing C.1. The column **tottime** shows the total time it took for the corresponding function to execute. **cumtime** shows the execution time of the function and all the other functions called from inside of it. The **sort()** function (underlined) is the most computationally expensive in this case.

Listing C.1: Profiling a simple sorting function

```
import cProfile
from test import arr


def sort(arr_1):
    l = len(arr_1)
    for i in range(l):
        for j in range(l):
            if arr_1[i] > arr_1[j]:
                arr_1[i], arr_1[j] = arr_1[j], arr_1[i]


def main():
    sort(arr)


cProfile.run('main()')
```

```
         8267 function calls in 0.123 seconds

   Ordered by: standard name

   ncalls  tottime  percall  cumtime  percall filename:lineno(function)
        1    0.000    0.000    0.123    0.123 <string>:1(<module>)
        1    0.000    0.000    0.123    0.123 main_1.py:13(main)
        1    0.000    0.000    0.003    0.003 main_1.py:15(<listcomp>)
        1    0.119    0.119    0.119    0.119 main_1.py:5(sort)
     1000    0.001    0.000    0.001    0.000 random.py:239(_randbelow_with_getrandbits)
     1000    0.001    0.000    0.002    0.000 random.py:292(randrange)
     1000    0.000    0.000    0.003    0.000 random.py:366(randint)
     3000    0.000    0.000    0.000    0.000 {built-in method _operator.index}
        1    0.000    0.000    0.123    0.123 {built-in method builtins.exec}
        1    0.000    0.000    0.000    0.000 {built-in method builtins.len}
        1    0.000    0.000    0.000    0.000 {built-in method builtins.print}
     1000    0.000    0.000    0.000    0.000 {method 'bit_length' of 'int' objects}
        1    0.000    0.000    0.000    0.000 {method 'disable' of '_lsprof.Profiler' objects}
     1259    0.000    0.000    0.000    0.000 {method 'getrandbits' of '_random.Random' objects}
```

Figure C.1: Output of the profiler

The above code can be compiled as it is or after adding Cython types. The Cython style code will look like the following:

Listing C.2: Extended Python code with explicit types

```
import random
from test import arr


def sort(list arr_1):
    cdef int l, j, i
    l = len(arr_1)
    for i in range(l):
        for j in range(l):
            if arr_1[i] > arr_1[j]:
                arr_1[i], arr_1[j] = arr_1[j], arr_1[i]


def main():
    sort(arr)
```

After compiling it, the profiling for the compiled version of the code is presented in figure C.2.

```
         4 function calls in 0.014 seconds

   Ordered by: standard name

   ncalls  tottime  percall  cumtime  percall filename:lineno(function)
        1    0.000    0.000    0.014    0.014 <string>:1(<module>)
        1    0.000    0.000    0.014    0.014 {built-in method builtins.exec}
        1    0.000    0.000    0.000    0.000 {method 'disable' of '_lsprof.Profiler' objects}
        1    0.014    0.014    0.014    0.014 {sort.sort}
```

Figure C.2: Output of the profiler for the compiled version of the code

It can be seen, that just by adding data types into a Python code and compiling it, the execution time of the code decrease approximately 19 times (same array of length 1000 was used for pure Python function and for the compiled version).

gprof2dot (https://github.com/jrfonseca/gprof2dot) Python package allows to visualize the statistics provided by the profiler. Figure C.3 shows visualization performed by the gprof2dot package. Each node in the graph represents a function call. Arrows indicate the order of the execution. The nodes are color-mapped such that the blue nodes are taking the least amount of time, whereas increased red hue indicates more execution time. As it can be seen, 96.93% of the code execution time was taken by the function **main()**, which calls the function **sort()**, that takes 93.24% of the overall execution time.

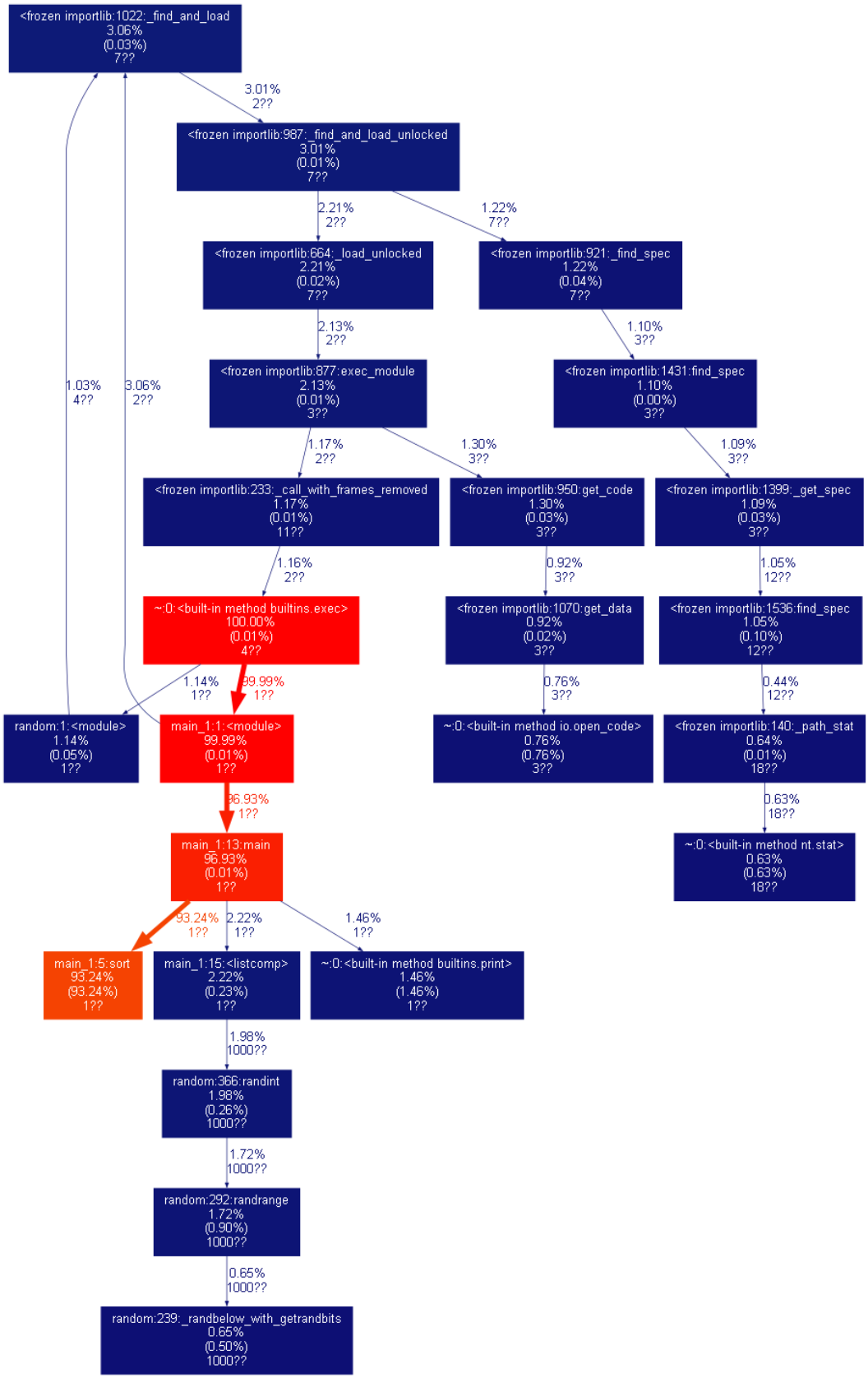


Figure C.3: Visualized statistics provided by the profiler

The profiling for AICON is shown in figure C.4. It can be seen that the function that takes the most time to execute is the one called **norm()**, which is called from the function responsible for iterating over the particles and calculating every distance. This unravels the bottleneck of the code, which then allows to work on optimization on that part of the code.

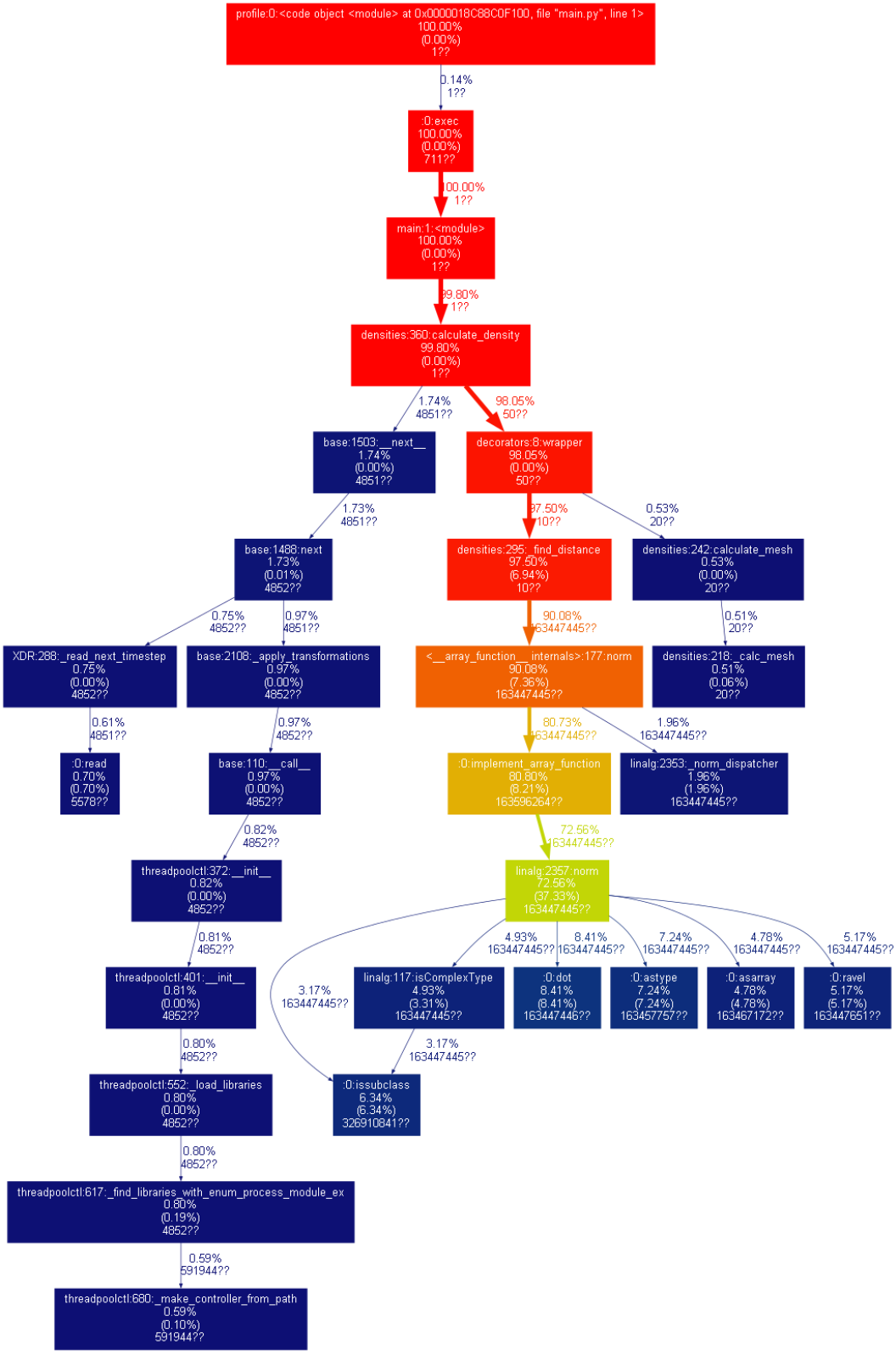


Figure C.4: The visualization of the results from profiling the AICON code.

Appendix D

Additional analysis for Triton X-100- and Tyloxapol-based mixed micelles

In 75% TYL7 system, the percentage of TYL7 neighbours around TX-100 molecules does has a little change through time, whereas in 75% TYL3 system, it changes significantly in comparison as the molecules move around easier (Figure D.1).

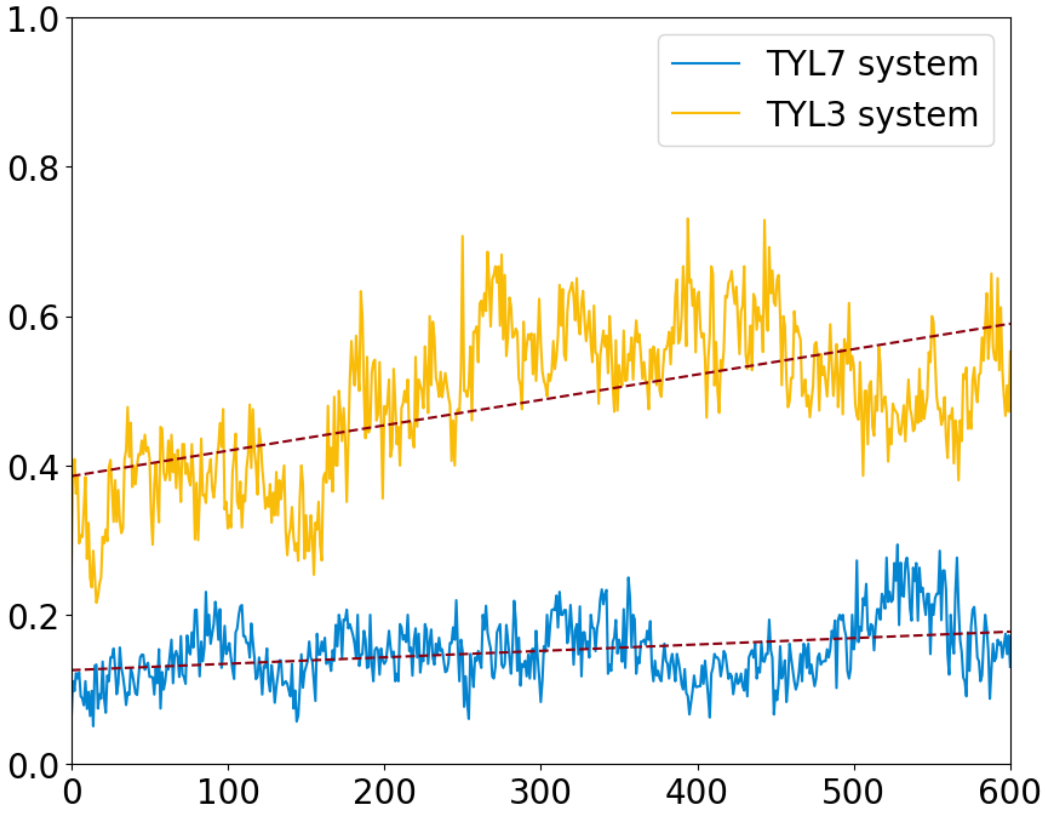


Figure D.1: Radius of gyration for Tyloxapol and Triton X-100 mixed micelles

Bibliography

(1) Schwartz, A. M.; Perry, J. W.; Bartell, F. E. *The Journal of Physical and Colloid Chemistry* **2002**, *53*, 1467–1467.

(2) YU, Y.; ZHAO, J.; Bayly, A. E. *Chinese Journal of Chemical Engineering* **2008**, *16*, 517–527.

(3) Karsa, D. R., *Industrial applications of surfactants IV*; 230; Elsevier: 1999.

(4) Partearroyo, M. A.; Ostolaza, H.; Goñi, F. M.; Barberá-Guillem, E. *Biochemical Pharmacology* **1990**, *40*, 1323–1328.

(5) Kumar, G. P.; Rajeshwarrao, P. *Acta Pharmaceutica Sinica B* **2011**, *1*, 208–219.

(6) Lawrence, M. J. *European Journal of Drug Metabolism and Pharmacokinetics 1994 19:3* **1994**, *19*, 257–269.

(7) Drummond, C. J.; Fong, C. *Current Opinion in Colloid & Interface Science* **1999**, *4*, 449–456.

(8) Kaur, P.; Garg, T.; Rath, G.; Murthy, R. S.; Goyal, A. K. *https://doi.org/10.3109/10717544.2014.935530* **2014**, *23*, 727–738.

(9) Myers, D., *Surfactant science and technology*; John Wiley & Sons: 2020.

(10) Schick, M. J., *Nonionic surfactants: physical chemistry*; CRC Press: 1987.

(11) Kislik, V. S. *Solvent Extraction* **2012**, 451–481.

(12) Elnaggar, Y. S.; El-Massik, M. A.; Abdallah, O. Y. *International Journal of Pharmaceutics* **2009**, *380*, 133–141.

(13) Akula, S.; Gurram, A. K.; Devireddy, S. R. *International Scholarly Research Notices* **2014**, *2014*, 1–11.

(14) Chen, F.; Wang, Y.; Zheng, F.; Wu, Y.; Liang, W. *Colloids and Surfaces A: Physicochemical and Engineering Aspects* **2000**, *175*, 257–262.

(15) Itoh, K.; Tozuka, Y.; Oguchi, T.; Yamamoto, K. *International Journal of Pharmaceutics* **2002**, *238*, 153–160.

(16) Singh, A.; Van Hamme, J. D.; Ward, O. P. *Biotechnology Advances* **2007**, *25*, 99–121.

(17) Rieger, M., *Surfactants in cosmetics*; Routledge: 2017.

(18) Mehta, S.; Jindal, N. *Colloids and Surfaces B: Biointerfaces* **2013**, *101*, 434–441.

(19) Falk, N. A. *Journal of Surfactants and Detergents* **2019**, *22*, 1119–1127.

(20) Vieira, D. B.; Carmona-Ribeiro, A. M. *Journal of Antimicrobial Chemotherapy* **2006**, *58*, 760–767.

(21) Kindall, H.; Pimentel, D. *The Royal Swedish Academy of Science* **1994**, *23*.

(22) Castro, M. J. L.; Ojeda, C.; Cirelli, A. F., *Surfactants in Agriculture*, 2013.

(23) Jazzar, C.; Hammad, E. A.-F. *Bulletin of Insectology* **2003**, *56*, 269–275.

(24) Gronwald, J. W.; Plaisance, K. L.; Ide, D. A.; Wyse, D. L. *Weed Science* **2002**, *50*, 397–404.

(25) Stevens, P. J. *Pesticide Science* **1993**, *38*, 103–122.

(26) Johnson, H. E.; Hazen, J. L.; Penner, D. *Weed Technology* **2002**, *16*, 867–872.

(27) Knepper, T. P.; Berna, J. L. In *Analysis and Fate of Surfactants and the Aquatic Environment*; Comprehensive Analytical Chemistry, Vol. 40; Elsevier: 2003, pp 1–49.

(28) Tadros, T. F., *Applied surfactants: principles and applications*; John Wiley & Sons: 2006.

(29) Speight, J. G. *Natural Water Remediation* **2020**, 263–303.

(30) Chu, W. *Practice Periodical of Hazardous, Toxic, and Radioactive Waste Management* **2003**, *7*, 19–24.

(31) West, C. C.; Harwell, J. H. *Environmental Science & Technology* **1992**, *26*, 2324–2330.

(32) Wayt, H. J.; Wilson, D. J. *http://dx.doi.org/10.1080/01496398908049882* **2006**, *24*, 905–937.

(33) Donaldson, E. C.; Chilingarian, G. V.; Yen, T. F., *Microbial enhanced oil recovery*; Newnes: 1989.

(34) Patel, J.; Borgohain, S.; Kumar, M.; Rangarajan, V.; Somasundaran, P.; Sen, R. *Renewable and Sustainable Energy Reviews* **2015**, *52*, 1539–1558.

(35) Saravanan, A.; Kumar, P. S.; Vardhan, K. H.; Jeevanantham, S.; Karishma, S. B.; Yaashikaa, P. R.; Vellaichamy, P. *Journal of Cleaner Production* **2020**, *258*, 120777.

(36) Pal, S.; Mushtaq, M.; Banat, F.; Sumaiti, A. M. A. *Petroleum Science* **2018**, *15*, 77–102.

(37) Pal, N.; Hoteit, H.; Mandal, A. *Journal of Molecular Liquids* **2021**, *339*, 116811.

(38) Liu, Z.; Zhao, G.; Brewer, M.; Lv, Q.; Sudhölter, E. J. *Advances in Colloid and Interface Science* **2021**, *294*, 102467.

(39) Saji, V. S.; Umoren, S. A., *Corrosion inhibitors in the oil and gas industry*; John Wiley & Sons: 2020.

(40) Obot, I. B.; Solomon, M. M.; Umoren, S. A.; Suleiman, R.; Elanany, M.; Alanazi, N. M.; Sorour, A. A. *Journal of Industrial and Engineering Chemistry* **2019**, *79*, 1–18.

(41) Jr., E. D. S.; Koh, C. A.; Koh, C. A. *Clathrate Hydrates of Natural Gases* **2007**, DOI: 10.1201/9781420008494.

(42) Kelland, M. A. *Energy & Fuels* **2006**, *20*, 825–847.

(43) Semenov, A. P.; Mendgaziev, R. I.; Stoporev, A. S.; Kuchierskaya, A. A.; Novikov, A. A.; Vinokurov, V. A. *Journal of Natural Gas Science and Engineering* **2020**, *82*, 103491.

(44) Farhadian, A.; Naeiji, P.; Varfolomeev, M. A.; Peyvandi, K.; Kiiamov, A. G. *Chemical Engineering Journal* **2022**, *427*, 131852.

(45) Amidon, G. L.; Lennernäs, H.; Shah, V. P.; Crison, J. R. *Pharmaceutical Research: An Official Journal of the American Association of Pharmaceutical Scientists* **1995**, *12*, 413–420.

(46) Nasir, S.; Hussain, A.; Abbas, N.; Bukhari, N. I.; Hussain, F.; Arshad, M. S. *International Journal of Pharmaceutics* **2021**, *604*, 120775.

(47) Fahr, A.; Liu, X. *Expert Opinion on Drug Delivery* **2007**, *4*, 403–416.

(48) Larrañeta, E.; Stewart, S.; Ervine, M.; Al-Kasasbeh, R.; Donnelly, R. *Journal of Functional Biomaterials* **2018**, *9*, 13.

(49) Wang, G.; Wang, J.; Wu, W.; To, S. S. T.; Zhao, H.; Wang, J. *Expert Opinion on Drug Delivery* **2015**, *12*, 1475–1499.

(50) Shubhra, Q. T. H.; Tóth, J.; Gyenis, J.; Feczkó, T. *Polymer Reviews* **2014**, *54*, 112–138.

(51) https://www.ema.europa.eu/en/medicines/human/EPAR/abraxane.

(52) https://chemocare.com/chemotherapy/drug-info/doxil.aspx.

(53) https://dailymed.nlm.nih.gov/dailymed/fda/fdaDrugXsl.cfm?setid=9b8ea543-1de8-472f-9666-34f99ca2f183&type=display.

(54) `https://flarin.co.uk/`.

(55) Pouton, C. W. *International Journal of Pharmaceutics* **1985**, *27*, 335–348.

(56) Buyukozturk, F.; Benneyan, J. C.; Carrier, R. L. *Journal of Controlled Release* **2010**, *142*, 22–30.

(57) Rani, S.; Rana, R.; Saraogi, G. K.; Kumar, V.; Gupta, U. *AAPS PharmSciTech* **2019**, *20*, 129.

(58) Goodhart, F. W.; McCoy, R. H.; Ninger, F. C. *Journal of Pharmaceutical Sciences* **1973**, *62*, 304–310.

(59) Leinonen, U.; Jalonen, H.; Vihervaara, P.; Laine, E. *Journal of Pharmaceutical Sciences* **1992**, *81*, 1194–1198.

(60) Barreiro-Iglesias, R.; Alvarez-Lorenzo, C.; Concheiro, A. *Journal of Controlled Release* **2003**, *93*, 319–330.

(61) Dun, J.; Osei-Yeboah, F.; Boulas, P.; Lin, Y.; Sun, C. C. *International Journal of Pharmaceutics* **2018**, *552*, 139–147.

(62) Calahan, J. L.; Paul, S.; Yanez, E. G.; DeNeve, D.; Sun, C. C.; Munson, E. J. *Pharmaceutical Development and Technology* **2021**, *26*, 150–156.

(63) Tsai, C. H.; Vivero-Escoto, J. L.; Slowing, I. I.; Fang, I. J.; Trewyn, B. G.; Lin, V. S. *Biomaterials* **2011**, *32*, 6234–6244.

(64) Li, Y.; Yang, D.; Lu, S.; Lao, S.; Qiu, X. *Journal of Agricultural and Food Chemistry* **2018**, *66*, 3457–3464.

(65) Carvalho, F. C.; Sarmento, V. H.; Chiavacci, L. A.; Barbi, M. S.; Gremião, M. P. *Journal of Pharmaceutical Sciences* **2010**, *99*, 2367–2374.

(66) Camacho-Muñoz, D.; Martín, J.; Santos, J. L.; Aparicio, I.; Alonso, E. *Science of The Total Environment* **2014**, *468-469*, 977–984.

(67) Bautista-Toledo, M. I.; Rivera-Utrilla, J.; Méndez-Díaz, J. D.; Sánchez-Polo, M.; Carrasco-Marín, F. *Journal of Colloid and Interface Science* **2014**, *418*, 113–119.

(68) Palmer, M.; Hatley, H. *Water Research* **2018**, *147*, 60–72.

(69) Marrakchi, S.; Maibach, H. I. *Skin Pharmacology and Physiology* **2006**, *19*, 177–180.

(70) Effendy, I.; Maibach, H. I. *Contact dermatitis* **1995**, *33*, 217–225.

(71) Xue, Y.; Zhang, S.; Tang, M.; Zhang, T.; Wang, Y.; Hieda, Y.; Takeshita, H. *Journal of Applied Toxicology* **2012**, *32*, 480–487.

(72) Pulce, C.; Descotes, J. In *Human Toxicology*, DESCOTES, J., Ed.; Elsevier Science B.V.: Amsterdam, 1996, pp 683–702.

(73) Xiang, W.; Tardy, B.; Bai, L.; Stubenrauch, C.; Rojas, O. J. Measuring the Interfacial Behavior of Sugar-Based Surfactants to Link Molecular Structure and Uses, 2019.

(74) Espert, A.; Klitzing, R. V.; Poulin, P.; Colin, A.; Zana, R.; Langevin, D. *Langmuir* **1998**, *14*, 4251–4260.

(75) Kern, F.; Lequeux, F.; Zana, R.; Candau, S. J. *Langmuir* **1994**, *10*, 1714–1723.

(76) Hoque, J.; Akkapeddi, P.; Yarlagadda, V.; Uppu, D. S.; Kumar, P.; Haldar, J. *Langmuir* **2012**, *28*, 12225–12234.

(77) Zhang, S.; Ding, S.; Yu, J.; Chen, X.; Lei, Q.; Fang, W. *Langmuir* **2015**, *31*, 12161–12169.

(78) Zhou, C.; Wang, F.; Chen, H.; Li, M.; Qiao, F.; Liu, Z.; Hou, Y.; Wu, C.; Fan, Y.; Liu, L.; Wang, S.; Wang, Y. *ACS Applied Materials & Interfaces* **2016**, *8*, 4242–4249.

(79) Schott, H. *Journal of Colloid and Interface Science* **1998**, *205*, 496–502.

(80) Regev, O.; Zana, R. *Journal of Colloid and Interface Science* **1999**, *210*, 8–17.

(81) Mehta, S.; Jindal, N. *Colloids and Surfaces B: Biointerfaces* **2013**, *110*, 419–425.

(82) Dharaiya, N.; Aswal, V. K.; Bahadur, P. *Colloids and Surfaces A: Physicochemical and Engineering Aspects* **2015**, *470*, 230–239.

(83) Vainio, H.; Morgan, G. *Pharmacology & Toxicology* **1997**, *81*, 151–152.

(84) KANTOR, T. G. *Annals of Internal Medicine* **1979**, *91*, 877.

(85) Todd, P. A.; Clissold, S. P. *Drugs* **1990**, *40*, 91–137.

(86) Small, R. E. *Clinical Pharmacy* **1989**, *8*, 545–558.

(87) Alván, G.; Orme, M.; Bertilsson, L.; Ekstrand, R.; Palmér, L. *Clinical Pharmacology & Therapeutics* **1975**, *18*, 364–373.

(88) Vane, J. R.; Botting, R. M. *Scandinavian Journal of Rheumatology* **1996**, *25*, 9–21.

(89) Ghlichloo, I.; Gerriets, V. *Treatment of Chronic Pain Conditions: A Comprehensive Handbook* **2022**, 77–79.

(90) Sostres, C.; Gargallo, C. J.; Arroyo, M. T.; Lanas, A. *Best practice & research. Clinical gastroenterology* **2010**, *24*, 121–132.

(91) Bally, M.; Dendukuri, N.; Rich, B.; Nadeau, L.; Helin-Salmivaara, A.; Garbe, E.; Brophy, J. M. *BMJ* **2017**, *357*, DOI: 10.1136/bmj.j1909.

(92) Schafer, A. I. *The American journal of medicine* **1999**, *106*, 25S–36S.

(93) Süleyman, H.; Demircan, B.; Karagöz, Y. *Pharmacological reports : PR* **2007**, *59*, 247–58.

(94) Patrignani, P. *Toxicology Letters* **2000**, *112-113*, 493–498.

(95) Murray, M. D.; Brater, D. C. *https://doi.org/10.1146/annurev.pa.33.040193.002251* **2003**, *33*, 435–465.

(96) Conaghan, P. G. *Rheumatology International* **2012**, *32*, 1491–1502.

(97) Nissen, S. E. et al. *The New England journal of medicine* **2016**, *375*, 2519–2529.

(98) Solomon, D. H.; Husni, M. E.; Libby, P. A.; Yeomans, N. D.; Lincoff, A. M.; Luscher, T. F.; Menon, V.; Brennan, D. M.; Wisniewski, L. M.; Nissen, S. E.; Borer, J. S. *American Journal of Medicine* **2017**, *130*, 1415–1422.e4.

(99) Varrassi, G.; Pergolizzi, J. V.; Dowling, P.; Paladini, A. *Advances in Therapy* **2020**, *37*, 61–82.

(100) Lucas, S. *Headache: The Journal of Head and Face Pain* **2016**, *56*, 436–446.

(101) Nalamachu, S.; Wortmann, R. *Postgraduate Medicine* **2014**, *126*, 92–97.

(102) Branden, C. I.; Tooze, J. *Introduction to Protein Structure* **2012**, DOI: 10.1201/9781136969898.

(103) Zhang, S. *Biotechnology Advances* **2002**, *20*, 321–339.

(104) Zhang, S. *Nature Biotechnology 2003 21:10* **2003**, *21*, 1171–1178.

(105) Saaem, I.; Labean, T. H. *Wiley Interdisciplinary Reviews: Nanomedicine and Nanobiotechnology* **2013**, *5*, 150–162.

(106) Linko, V.; Ora, A.; Kostiainen, M. A. *Trends in Biotechnology* **2015**, *33*, 586–594.

(107) Whitesides, G. M.; Mathias, J. P.; Seto, C. T. *Science* **1991**, *254*, 1312–1319.

(108) Ahir, S. V.; Petrov, P. G.; Terentjev, E. M. *Langmuir* **2002**, *18*, 9140–9148.

(109) Beyer, K. *Journal of Colloid and Interface Science* **1982**, *86*, 73–89.

(110) De Nicola, A.; Kawakatsu, T.; Rosano, C.; Celino, M.; Rocco, M.; Milano, G. *Journal of Chemical Theory and Computation* **2015**, *11*, PMID: 26574282, 4959–4971.

(111) Yordanova, D.; Smirnova, I.; Jakobtorweihen, S. *Journal of Chemical Theory and Computation* **2015**, *11*, 2329–2340.

(112) Solomonov, A. V.; Marfin, Y. S.; Rumyantsev, E. V.; Ragozin, E.; Zahavi, T. S.; Gellerman, G.; Tesler, A. B.; Muench, F.; Kumagai, A.; Miyawaki, A. *Materials Science and Engineering: C* **2019**, *99*, 794–804.

(113) Metropolis, N.; Rosenbluth, A. W.; Rosenbluth, M. N.; Teller, A. H.; Teller, E. *The Journal of Chemical Physics* **1953**, *21*, 1087–1092.

(114) Alder, B. J.; Wainwright, T. E. *The Journal of Chemical Physics* **2004**, *27*, 1208.

(115) Alder, B. J.; Wainwright, T. E. *The Journal of Chemical Physics* **1959**, *31*, 459–466.

(116) Rahman, A. *Physical Review* **1964**, *136*, A405.

(117) Uarp, G. D.; Berne, B. J. *The Journal of Chemical Physics* **2003**, *49*, 1249.

(118) Harp, G. D.; Berne, B. J. *Physical Review A* **1970**, *2*, 975.

(119) Rahman, A.; Stillinger, F. H. *The Journal of Chemical Physics* **1971**, *55*, 3336–3359.

(120) McCammon, J. A.; Gelin, B. R.; Karplus, M. *Nature 1977 267:5612* **1977**, *267*, 585–590.

(121) Levitt, M. In *Cold Spring Harbor symposia on quantitative biology*, 1983; Vol. 47, pp 251–262.

(122) Lee, E. H.; Hsin, J.; Sotomayor, M.; Comellas, G.; Schulten, K. *Structure* **2009**, *17*, 1295–1306.

(123) Hautman, J.; Klein, M. L. *The Journal of Chemical Physics* **1989**, *91*, 4994–5001.

(124) Karaborni, S.; Esselink, K.; Hilbers, P. A. J.; Smit, B.; Karthauser, J.; van Os, N. M.; Zana, R. *Science* **1994**, *266*, 254–256.

(125) Griffiths, J. A.; Heyes, D. M. *Langmuir* **1996**, *12*, 2418–2424.

(126) Salvalaglio, M.; Vetter, T.; Giberti, F.; Mazzotti, M.; Parrinello, M. *Journal of the American Chemical Society* **2012**, *134*, 17221–17223.

(127) Salvalaglio, M.; Mazzotti, M.; Parrinello, M. *Faraday Discussions* **2015**, *179*, 291–307.

(128) Salvalaglio, M.; Perego, C.; Giberti, F.; Mazzotti, M.; Parrinello, M. *Proceedings of the National Academy of Sciences of the United States of America* **2015**, *112*, E6–E14.

(129) Lorenz, C. D.; Hsieh, C. M.; Dreiss, C. A.; Lawrence, M. J. *Langmuir : the ACS journal of surfaces and colloids* **2011**, *27*, 546–553.

(130) Hollingsworth, S. A.; Dror, R. O. *Neuron* **2018**, *99*, 1129–1143.

(131) Proctor, C. J.; Boche, D.; Gray, D. A.; Nicoll, J. A. *PLOS ONE* **2013**, *8*, e73631.

(132) Nasica-Labouze, J. et al. *Chemical Reviews* **2015**, *115*, 3518–3563.

(133) Nguyen, P. H.; Derreumaux, P. *Biophysical Chemistry* **2020**, *264*, 106421.

(134) Boopathi, S.; Poma, A. B.; Garduño-Juárez, R. *International Journal of Molecular Sciences* **2021**, *22*, 10798.

(135) Manglik, A. et al. *Nature* **2016**, *537*, 185.

(136) McCorvy, J. D.; Butler, K. V.; Kelly, B.; Rechsteiner, K.; Karpiak, J.; Betz, R. M.; Kormos, B. L.; Shoichet, B. K.; Dror, R. O.; Jin, J.; Roth, B. L. *Nature Chemical Biology* **2018**, *14*, 126–134.

(137) Pardo, L. C.; Tamarit, J. L.; Veglio, N.; Bermejo, F. J.; Cuello, G. J. *Physical Review B* **2007**, *76*, 134203.

(138) Rey, R.; Pardo, L. C.; Llanta, E.; Ando, K.; López, D. O.; Tamarit, J. L.; Barrio, M. *The Journal of Chemical Physics* **2000**, *112*, 7505–7517.

(139) Mason, P. E.; Neilson, G. W.; Dempsey, C. E.; Brady, J. W. *Journal of the American Chemical Society* **2006**, *128*, 15136–15144.

(140) Takemoto, M.; Kato, H. E.; Koyama, M.; Ito, J.; Kamiya, M.; Hayashi, S.; Maturana, A. D.; Deisseroth, K.; Ishitani, R.; Nureki, O. *PLoS ONE* **2015**, *10*, 131094.

(141) Larson, R. G. *The Journal of Chemical Physics* **1988**, *89*, 1642–1650.

(142) Larson, R. G. *The Journal of Chemical Physics* **1988**, *91*, 2479.

(143) Smit, B.; Hilbers, P. A.; Esselink, K.; Rupert, L. A.; Os, N. M. V.; Schlijper, A. G. *Nature 1990 348:6302* **1990**, *348*, 624–625.

(144) Smit, B.; Hilbers, P. A.; Esselink, K.; Rupert, L. A.; Os, N. M. V.; Schlijper, A. G. *Journal of Physical Chemistry* **1991**, *95*, 6361–6368.

(145) Karaborni, S.; Os, N. M. V.; Esselink, K.; Hilbers, P. A. J. *Langmuir* **1993**, *9*, 1175–1178.

(146) Tanis-Kanbur, M. B.; Velioğlu, S.; Tanudjaja, H. J.; Hu, X.; Chew, J. W. *Journal of Membrane Science* **2018**, *566*, 140–150.

(147) Almeida, J. A.; Marques, E. F.; Jurado, A. S.; Pais, A. A. *Physical Chemistry Chemical Physics* **2010**, *12*, 14462–14476.

(148) Ma, Y.; Velioğlu, S.; Trinh, T. A.; Wang, R.; Chew, J. W. *ACS ES&T Engineering* **2021**, *1*, 1470–1480.

(149) Bandyopadhyay, S.; Shelley, J. C.; Klein, M. L. *Journal of Physical Chemistry B* **2001**, *105*, 5979–5986.

(150) Rezaeisadat, M.; Bordbar, A. K.; Omidyan, R. *Journal of Molecular Liquids* **2021**, *332*, 115862.

(151) Patel, S. K.; Lavasanifar, A.; Choi, P. *Biomaterials* **2010**, *31*, 1780–1786.

(152) Luo, Z.; Jiang, J. *Journal of Controlled Release* **2012**, *162*, 185–193.

(153) Poghosyan, A. H.; Schafer, N. P.; Lyngsø, J.; Shahinyan, A. A.; Pedersen, J. S.; Otzen, D. E. *Protein Engineering, Design and Selection* **2019**, *32*, 175–190.

(154) Liu, Y. T.; Li, H. M.; Gao, M. Z.; Ye, S. Q.; Zhao, Y.; Xie, J.; Liu, G. K.; Liu, J. J.; Li, L. M.; Deng, J.; Zhou, W. Q. *RSC Advances* **2021**, *11*, 24543–24555.

(155) Fatemi, S. M.; Foroutan, M. *Journal of the Iranian Chemical Society* **2015**, *12*, 1905–1913.

(156) Van Rossum, G.; Drake, F. L., *Python 3 Reference Manual*; CreateSpace: Scotts Valley, CA, 2009.

(157) Hopfinger, A. J.; Pearlstein, R. A. *Journal of Computational Chemistry* **1984**, *5*, 486–499.

(158) Krieger, E.; Darden, T.; Nabuurs, S. B.; Finkelstein, A.; Vriend, G. *Proteins: Structure, Function, and Bioinformatics* **2004**, *57*, 678–683.

(159) Monticelli, L.; Tieleman, D. P. **2013**, 197–213.

(160) Allen, M. P.; Tildesley, D. J., *Computer simulation of liquids*; Oxford university press: 2017.

(161) Brooks, B. R.; Bruccoleri, R. E.; Olafson, B. D.; States, D. J.; Swaminathan, S.; Karplus, M. *Journal of Computational Chemistry* **1983**, *4*, 187–217.

(162) Huang, J.; Mackerell, A. D. *Journal of computational chemistry* **2013**, *34*, 2135–2145.

(163) Huang, J.; Rauscher, S.; Nawrocki, G.; Ran, T.; Feig, M.; de Groot, B. L.; Grubmüller, H.; MacKerell, A. D. *Nat. Methods* **2017**, *14*, 71–73.

(164) Heinz, H.; Lin, T. J.; Mishra, R. K.; Emami, F. S. *Langmuir* **2013**, *29*, 1754–1765.

(165) Senftle, T. P.; Hong, S.; Islam, M. M.; Kylasa, S. B.; Zheng, Y.; Shin, Y. K.; Junkermeier, C.; Engel-Herbert, R.; Janik, M. J.; Aktulga, H. M.; Verstraelen, T.; Grama, A.; Duin, A. C. V. *npj Computational Materials 2016 2:1* **2016**, *2*, 1–14.

(166) Allinger, N. L.; Yuh, Y. H.; Lii, J. H. *Journal of the American Chemical Society* **1989**, *111*, 8551–8566.

(167) Van Westen, T.; Vlugt, T. J. H.; Gross, J. *The Journal of Physical Chemistry B* **2011**, *115*, 7872–7880.

(168) Marrink, S. J.; Risselada, H. J.; Yefimov, S.; Tieleman, D. P.; Vries, A. H. D. *Journal of Physical Chemistry B* **2007**, *111*, 7812–7824.

(169) Souza, P. C. T. et al. *Nature Methods* **2021**, *18*, 382–388.

(170) Allen, D. T.; Lorenz, C. D. *Journal of Molecular Modeling* **2017**, *23*, 1–11.

(171) Kim, S. *Physics Procedia* **2014**, *53*, 60–62.

(172) Hess, B.; Bekker, H.; Berendsen, H. J. C.; Fraaije, J. G. E. M. *Journal of Computational Chemistry* **1997**, *18*, 1463–1472.

(173) Ryckaert, J.-P.; Ciccotti, G.; Berendsen, H. J. *Journal of Computational Physics* **1977**, *23*, 327–341.

(174) Ewald, P. P. *Annalen der Physik* **1921**, *369*, 253–287.

(175) Darden, T.; Perera, L.; Li, L.; Pedersen, L. *Structure* **1999**, *7*, R55–R60.

(176) Hünenberger, P. H. Thermostat Algorithms for Molecular Dynamics Simulations, 2005.

(177) Berendsen, H. J. C.; Postma, J. P. M.; van Gunsteren, W. F.; DiNola, A.; Haak, J. R. *The Journal of Chemical Physics* **1984**, *81*, 3684–3690.

(178) Paci, E.; Marchi, M. *Journal of Physical Chemistry* **1996**, *100*, 4314–4322.

(179) Morishita, T. *The Journal of Chemical Physics* **2000**, *113*, 2976–2982.

(180) Nosé, S. *Molecular Physics* **1984**, *52*, 255–268.

(181) Hoover, W. G. *Physical Review A* **1985**, *31*, 1695–1697.

(182) Parrinello, M.; Rahman, A. *Physical Review Letters* **1980**, *45*, 1196–1199.

(183) Martínez, L.; Andrade, R.; Birgin, E. G.; Martínez, J. M. *Journal of Computational Chemistry* **2009**, *30*, 2157–2164.

(184) Bekker, H.; Berendsen, H.; Dijkstra, E.; Achterop, S.; Drunen, R.; van der Spoel, D.; Sijbers, A.; Keegstra, H.; Reitsma, B.; Renardus, M. *Physics Computing* **1993**, *92*, 252–256.

(185) Berendsen, H.; van der Spoel, D.; van Drunen, R. *Computer Physics Communications* **1995**, *91*, 43–56.

(186) Abraham, M. J.; Murtola, T.; Schulz, R.; Páll, S.; Smith, J. C.; Hess, B.; Lindahl, E. *SoftwareX* **2015**, *1-2*, 19–25.

(187) Hub, J. S.; de Groot, B. L.; Grubmüller, H.; Groenhof, G. *Journal of Chemical Theory and Computation* **2014**, *10*, 381–390.

(188) Ziolek, R. M.; Omar, J.; Hu, W.; Porcar, L.; González-Gaitano, G.; Dreiss, C. A.; Lorenz, C. D. *Macromolecules* **2020**, *53*, 11065–11076.

(189) Jarvis, R. A. *Information Processing Letters* **1973**, *2*, 18–21.

(190) Barber, C. B.; Dobkin, D. P.; Huhdanpaa, H. *ACM Trans. Math. Softw.* **1996**, *22*, 469–483.

(191) Hagberg, A. A.; Schult, D. A.; Swart, P. J. In *Proceedings of the 7th Python in Science Conference*, ed. by Varoquaux, G.; Vaught, T.; Millman, J., Pasadena, CA USA, 2008, pp 11–15.

(192) Humphrey, W.; Dalke, A.; Schulten, K. *Journal of Molecular Graphics* **1996**, *14*, 33–38.

(193) Stone, J. *An Efficient Library for Parallel Ray Tracing and Animation*, MA thesis, Computer Science Department, University of Missouri-Rolla, 1998.

(194) Hunter, J. D. *Computing in Science & Engineering* **2007**, *9*, 90–95.

(195) Adobe Inc. Adobe Photoshop, version CC 2019, 2019.

(196) Popović, Z.; Liu, W.; Chauhan, V. P.; Lee, J.; Wong, C.; Greytak, A. B.; Insin, N.; Nocera, D. G.; Fukumura, D.; Jain, R. K.; Bawendi, M. G. *Angewandte Chemie International Edition* **2010**, *49*, 8649–8652.

(197) Meyers, J. D.; Doane, T.; Burda, C.; Basilion, J. P. *Nanomedicine* **2013**, *8*, PMID: 23256496, 123–143.

(198) Wilczewska, A. Z.; Niemirowicz, K.; Markiewicz, K. H.; Car, H. *Pharmacological Reports* **2012**, *64*, 1020–1037.

(199) Couvreur, P. *Advanced Drug Delivery Reviews* **2013**, *65*, 21–23.

(200) Sanità, G.; Carrese, B.; Lamberti, A. *Frontiers in Molecular Biosciences* **2020**, *7*, 381.

(201) Neouze, M.-A.; Schubert, U. *Monatshefte für Chemie - Chemical Monthly* **2008**, *139*, 183–195.

(202) Albanese, A.; Tang, P. S.; Chan, W. C. *Annual Review of Biomedical Engineering* **2012**, *14*, 1–16.

(203) Lewiner, T.; Lopes, H.; Vieira, A. W.; Tavares, G. *Journal of Graphics Tools* **2003**, *8*, 1–15.

(204) Willard, A. P.; Chandler, D. *Journal of Physical Chemistry B* **2010**, *114*, 1954–1958.

(205) Behnel, S.; Bradshaw, R.; Citro, C.; Dalcin, L.; Seljebotn, D. S.; Smith, K. *Computing in Science & Engineering* **2011**, *13*, 31–39.

(206) Michaud-Agrawal, N.; Denning, E. J.; Woolf, T. B.; Beckstein, O. *Journal of Computational Chemistry* **2011**, *32*, 2319–2327.

(207) Gowers, R.; Linke, M.; Barnoud, J.; Reddy, T.; Melo, M.; Seyler, S.; Domański, J.; Dotson, D.; Buchoux, S.; Kenney, I.; Beckstein, O. In 2016, pp 98–105.

(208) Harris, C. R. et al. *Nature* **2020**, *585*, 357–362.

(209) Virtanen, P. et al. *Nature Methods* **2020**, *17*, 261–272.

(210) .

(211) .

(212) Lam, S. K.; Pitrou, A.; Seibert, S. *Proceedings of LLVM-HPC 2015: 2nd Workshop on the LLVM Compiler Infrastructure in HPC - Held in conjunction with SC 2015: The International Conference for High Performance Computing, Networking, Storage and Analysis* **2015**, *2015-January*, DOI: 10.1145/2833157.2833162.

(213) .

(214) Flynn, M. J. *IEEE Transactions on Computers* **1972**, *C-21*, 948–960.

(215) Beckman, N. E. *May* **2006**, *10*, 1–20.

(216) Sekhon, B. S. *Journal of Pharmaceutical Technology, Research and Management* **2013**, *1*, 43–68.

(217) Zana, R. *Advances in Colloid and Interface Science* **2002**, *97*, 205–253.

(218) Chen, J.; Qiao, M.; Gao, N.; Ran, Q.; Wu, J.; Shan, G.; Qi, S.; Wu, S. *Colloids and Surfaces A: Physicochemical and Engineering Aspects* **2018**, *538*, 686–693.

(219) In, M.; Bec, V.; Aguerre-Chariol, O.; Zana, R. *Langmuir* **2000**, *16*, 141–148.

(220) Bunton, C. A.; Robinson, L. B.; Schaak, J.; Stam, M. F. *The Journal of Organic Chemistry* **1971**, *36*, 2346–2350.

(221) Zana, R.; Benrraou, M.; Rueff, R. *Langmuir* **1991**, *7*, 1072–1075.

(222) Dam, T.; Engberts, J.; Karthäuser, J.; Karaborni, S.; van Os, N. *Colloids and Surfaces A: Physicochemical and Engineering Aspects* **1996**, *118*, 41–49.

(223) Maiti, P. K.; Lansac, Y.; Glaser, M. A.; Clark, N. A.; Rouault, Y. *Langmuir* **2002**, *18*, 1908–1918.

(224) Wu, H.; Xu, J.; He, X.; Zhao, Y.; Wen, H. *Colloids and Surfaces A: Physicochemical and Engineering Aspects* **2006**, *290*, 239–246.

(225) Wang, P.; Pei, S.; Wang, M.; Yan, Y.; Sun, X.; Zhang, J. *Physical Chemistry Chemical Physics* **2017**, *19*, 4462–4468.

(226) Dharaiya, N.; Aswal, V. K.; Bahadur, P. *Colloids and Surfaces A: Physicochemical and Engineering Aspects* **2015**, *470*, 230–239.

(227) Scamehorn, J. F. An Overview of Phenomena Involving Surfactant Mixtures, 1986.

(228) Moroi, Y. Mixed Micelle Formation, 1992.

(229) Holland, P. M. Modeling Mixed Surfactant Systems, 1992.

(230) Haque, M. E.; Das, A. R.; Rakshit, A. K.; Moulik, S. P. *Langmuir* **1996**, *12*, 4084–4089.

(231) Khan, A.; Marques, E. F. *Current Opinion in Colloid & Interface Science* **1999**, *4*, 402–410.

(232) Acharya, D. P.; Kunieda, H. *Advances in Colloid and Interface Science* **2006**, *123-126*, 401–413.

(233) Sugihara, G.; Nagadome, S.; Oh, S. W.; Ko, J. S. *Journal of Oleo Science* **2008**, *57*, 61–92.

(234) Alakhov, V.; Klinski, E.; Li, S.; Pietrzynski, G.; Venne, A.; Batrakova, E.; Bronitch, T.; Kabanov, A. *Colloids and Surfaces B: Biointerfaces* **1999**, *16*, 113–134.

(235) Yoo, H. S.; Park, T. G. *Journal of Controlled Release* **2004**, *96*, 273–283.

(236) Gao, Z. G.; Fain, H. D.; Rapoport, N. *Journal of controlled release : official journal of the Controlled Release Society* **2005**, *102*, 203–222.

(237) Wu, X. L.; Kim, J. H.; Koo, H.; Bae, S. M.; Shin, H.; Kim, M. S.; Lee, B. H.; Park, R. W.; Kim, I. S.; Choi, K.; Kwon, I. C.; Kim, K.; Lee, D. S. *Bioconjugate Chemistry* **2010**, *21*, 208–213.

(238) Turner, D. C.; Yin, F.; Kindt, J. T.; Zhang, H. *Langmuir* **2010**, *26*, 4687–4692.

(239) Storm, S.; Jakobtorweihen, S.; Smirnova, I. *Journal of Physical Chemistry B* **2014**, *118*, 3593–3604.

(240) Wu, W.; Zou, Z.; Yang, S.; Wu, Q.; Li, W.; Ding, Q.; Guan, Z.; Zhu, W. *Langmuir* **2020**, *36*, 2082–2092.

(241) Vanommeslaeghe, K.; Hatcher, E.; Acharya, C.; Kundu, S.; Zhong, S.; Shim, J.; Darian, E.; Guvench, O.; Lopes, P.; Vorobyov, I.; Mackerell, A. D. *Journal of Computational Chemistry* **2009**, NA–NA.

(242) Mitternacht, S. *F1000Research* **2016**, *5*, 189.

(243) Lee, B.; Richards, F. *Journal of Molecular Biology* **1971**, *55*, 379–IN4.

(244) Allen, D. T.; Saaka, Y.; Lawrence, M. J.; Lorenz, C. D. *Journal of Physical Chemistry B* **2014**, *118*, 13192–13201.

(245) Ziolek, R. M.; Smith, P.; Pink, D. L.; Dreiss, C. A.; Lorenz, C. D. *Macromolecules* **2021**, *54*, 3755–3768.

(246) Lane, A. N.; Chaires, J. B.; Gray, R. D.; Trent, J. O. *Nucleic Acids Research* **2008**, *36*, 5482–5515.

(247) Bhattacharyya, D.; Arachchilage, G. M.; Basu, S. *Frontiers in Chemistry* **2016**, *4*, 38.

(248) Lipps, H. J.; Rhodes, D. *Trends in Cell Biology* **2009**, *19*, 414–422.

(249) Rhodes, D.; Lipps, H. J. *Nucleic Acids Research* **2015**, *43*, 8627–8637.

(250) Hall, D. J. *Oncogene* **1990**, *5*, 47–54.

(251) Hsu, S. T. D.; Varnai, P.; Bugaut, A.; Reszka, A. P.; Neidle, S.; Balasubramanian, S. *Journal of the American Chemical Society* **2009**, *131*, 13399–13409.

(252) Cogoi, S.; Xodo, L. E. *Nucleic Acids Research* **2006**, *34*, 2536–2549.

(253) Drygin, D.; Siddiqui-Jain, A.; O'Brien, S.; Schwaebe, M.; Lin, A.; Bliesath, J.; Ho, C. B.; Proffitt, C.; Trent, K.; Whitten, J. P.; Lim, J. K.; Hoff, D. V.; Anderes, K.; Rice, W. G. *Cancer Research* **2009**, *69*, 7653–7661.

(254) Xu, H. et al. *Nature Communications 2017 8:1* **2017**, *8*, 1–18.

(255) Xu, J.; Jiang, R.; He, H.; Ma, C.; Tang, Z. *TrAC Trends in Analytical Chemistry* **2021**, *139*, 116257.